FURTHER DEVELOPMENT OF ULTRA-HIGH-PERFORMANCE FIBER REINFORCED CONCRETE (UHP-FRC): 3D PRINTING, SIFCON, ALTERNATIVE FIBERS, SHRINKAGE CRACK CONTROL, HIGH TEMPERATURE, AND LIGHTWEIGHT

by

BHUPENDRA RAJ ACHARYA

Presented to the Faculty of the Graduate School of

The University of Texas at Arlington in Partial Fulfillment

of the Requirements

for the Degree of

MASTER OF SCIENCE IN CIVIL ENGINEERING

THE UNIVERSITY OF TEXAS AT ARLINGTON

August 2021

ACKNOWLEDGEMENTS

I would like to express my deepest appreciation to my supervising Professor Shih-Ho (Simon) Chao, for his unparalleled support, guidance, motivation, and encouragement throughout the duration of my Master's study at the University of Texas at Arlington. It would never be possible without his invaluable suggestions and technical supervision. It has been a real pleasure and honor to work with him. I would like to extend my deepest gratitude to Dr. Suyun Ham, Dr. Juan Antonio Balderrama, and Prof Brad Paul Bell for spending their invaluable time serving my thesis committee.

I would like to thank Mr. Varthan Babakhanian, Technical Services Lab Manager at Forterra Pipe & Precast in Grand Prairie, TX, for providing cement and fly ash that was used in this research. I would like to extend my sincere thanks to Ashish Karmacharya for guiding me at the beginning of my research work. I also had a great pleasure working with Alateeq Ahmed Abdullah, and Gonzalez Marilyn in some of my research work. Many thanks to Shamshiri Guilvayi Seyed Missagh, Dr. Kyoungsub Park, Dr. Ghassan Sulaiman Almasabha, and Dr. Ra'ed Khalil Mohammad Al-Mazaidh for their continuous guidance and encouragement in my laboratory work. I would also like to acknowledge the UTA CELB technician, Mr. Ebner Gary, for the technical support in the lab.

I am deeply grateful to my family members for their unrelenting encouragement and support for my decision to pursue an MS degree abroad. The blessing of my grandparents on every moment and on every decision is beyond expressing in words. Last but not the least, I would like to recognize the help and support of my friends for their everyday call and moral support.

August 2021

ABSTRACT

PRELIMINARY STUDY IN 3D PRINTED ULTRA-HIGH-PERFORMANCE FIBER-REINFORCED CONCRETE (UHP-FRC) AND ULTRA-HIGH-PERFORMANCE SLURRY INFILTRATED FIBER-REINFORCED CONCRETE (UHP-SIFCON)

Bhupendra Raj Acharya, MS
The University of Texas at Arlington, 2021

Supervising Professor: Shih-Ho Chao

Introduction of artificial intelligence (AI) and machine learning in manufacturing industry also in every service industry, decreasing conventional skilled workforce and stagnated construction industry, probability and past statistics of the accident at the construction sites and difficulty in quality control has led the researchers to think of the solution and alternatives of the conventional construction. A new construction paradigm, known as 3-D concrete printing or additive manufacturing of concrete (AMC) provides such a solution. This research focuses on a preliminary study in 3d printed ultra-high-performance fiber-reinforced concrete (UHP-FRC) and, has developed a novel mix that has balanced extrude-ability and buildability. In addition to this, to get an idea of highest possible mechanical properties of fiber reinforced concrete, ultra-high-performance slurry infiltrated fiber-reinforced concrete (UHP-SIFCON) has developed. The developed UHP-SIFCON can exhibit very high compressive strength more than 33 ksi for an equivalent compressive strain of 8% and high tensile strength of 2.34 ksi for an equivalent tensile strain of 1.07 %. The study further investigates the performance of UHP-FRC with different types of fiber for direct tensile loading. Furthermore, the study examines early age shrinkage cracking

and its mitigation measures. The use of UHF-FRC has been observed more severe failure in elevated temperature. So this study examines the performance of UHP-FRC at high temperatures and investigates the mitigation measures. At last, the study investigates reducing the unit weight of existing UHP-FRC and develops Lightweight high strength concrete with weight 60-70% of the weight of conventional UHP-FRC having 28 days compressive strength comparable to normal weight concrete. Any reduced weight can significantly reduce the design and construction work in other structural members such as columns, beams, and foundations. For buildings in high seismic areas, the reduced self-weight can lead to much smaller inertial forces thereby potentially reducing the damage induced by earthquakes.

TABLE OF CONTENTS

LIST OF FIGURES

LIST OF TABLES

1 INTRODUCTION

1.1 3D Printed Ultra-High-Performance Fiber-Reinforced Concrete

As an outwaited, emerging construction industry and manufacturing technology, 3D printing (3DP) was raised in the late 1980s and was first introduced to construction industry in 1997 [1]. 3D printing of concrete is a process of manufacturing of concrete with layer by layer concrete deposition based on a digital model to create a three dimensional object without the formwork or any support. ASTM defines additive manufacturing as "a process of joining materials to make objects from 3D model data, usually layer upon layer, as opposed to subtractive manufacturing methodologies'' [17]. In this free form layer wise fabrication, multiple layer are built in X-Y direction, on the top of one another to generate Z or 3rd dimension [2]. In order to ensure the implementation of 3DP technology, the first step of 3DP is to design a building path by a 3D-to-2D slicing software. It first slices the 3D shape of the object into flat thin layers with a certain thickness, and then designs the path of each layer. All these paths are made up of a contour line and a filling pattern (such as a honeycomb structure or a space filling curve). The main principle of this process is that the nozzle moves along a predetermined path and then the fresh concrete is extruded. After all the printing layers have been stacked, the construction is complete [3]. Complex geometrical curvilinear shapes, which are difficult to build using conventional concrete casting method, can be built using the 3DP technique is a unique advantages of 3DP over conventional construction method. Khoshnevis used this technique of contour crafting in the construction industry [7]. CC will most probably be one of the very few feasible

approaches for building structures on other planets, such as Moon and Mars, which are being targeted for human colonization before the end of the new century.

1.1.1 Why 3D Printing of Concrete

The world is moving towards the era of artificial intelligence (AI) and machine learning in manufacturing industry also in every service industry however the construction industry is stagnated for ages. Conventional method of construction techniques do not lend themselves to construction of large structurers with many internal features. The conventional skilled workforce is decreasing alarmingly each day because construction industry involves labor intensive work at construction sites, peoples are getting plenty of other opportunities, probability and past statistics of accident at the construction sites are higher comparable to other jobs. Also it is very difficult to control the work quality at construction site because of involvement of manual labor. So construction industry have become an industry with least benefit/cost ratio. Application of 3D- Printing of concrete as gained wide attention from researchers, engineers and construction practitioners around globe.

1.1.2 Properties of Printable Mix

For the concrete to be 3D printable the following two parameters should be met.

1. **Extrude-ability**

   It's the ability to continuously extrude through the nozzle of the printer with the required dimensional conformity and to form layers with good print quality.

2. Buildability

The ability of to retain shape once extruded is buildability. The number of concrete layers that could be built without noticeable deformation in the lower layer is used to access the buildability of mix.

Similar to the ink in normal inkjet printer, concrete acts like ink in 3D printable printer. Concrete printer is filled with the workable mix of concrete which is propelled with the help of pump to create a layer by layer deposition. The concrete mix should be sufficiently printable (workable) to make sure that concrete comes from the nozzle of printer. After the concrete layer is deposited, it should have sufficient yield stress to maintain its buildability. Ideally the material must acts like liquid having low viscosity inside the pump and it should go to a transition so that it should act like a solid behavior having enough stiffness to resist the deformation due to self-weight, and pressure acted over it. The workability and buildability of concrete mainly depends on its mix constituents and their proportion. It requires enough adhesion and rigidity to print high-rise buildings without any failure. According to the point of rheology, the higher viscosity and lower yield stress of concrete result in higher plasticity and better workability. Moreover, shorter setting time and higher early strength are also required for the 3D printed concrete [4]. To maintain sufficient workability and buildability is a critical task for mix designers. Many researchers have tried to prepare high performance 3D printable however this research focus on the development of 3-D printable ultra-high-performance fiber-reinforced concrete (UHP-FRC) for cost-effective maintenance and construction of transportation infrastructure. In order to reduce the use of reinforcement in the 3D printable concrete and to maintain the

sufficient ductility of structures, this research studies on the use of polyethylene fibers in the concrete mix.

Additive Manufacturing Technologies Explored in the Construction Industry [5]

a. D-Shape

b. Contour crafting

Contour Crafting is based upon extruding a cement-based paste against a trowel that creates a smooth surface finish through the buildup of subsequent layers. The D-Shape involves a powder deposition process, where each layer of building material is deposited to the desired thickness, compacted and then nozzles mounted on a gantry frame deposit the binder where the part is to be made solid [44]. Figure 1.1 shows a house printed by contour crafting method.

Figure 1. 1 3D Printed House (contour crafting)

1.1.3 Attraction towards 3D Printable Concrete

Architectural Freedom

3DP of construction techniques push boundaries for designers and engineers to design and built exotic and curvilinear geometric shapes. In 3DP, a gantry system carrying the nozzle moves on X-Y plane installed on the construction site. Gantry system have two dimensional freedom and can move up and down which allows it to build the free form structures which is very difficult to make using the traditional formwork construction. Figure 1.2 is an example of house printed by 3D printer and shows the wide scope of 3D concrete printing in architecture.

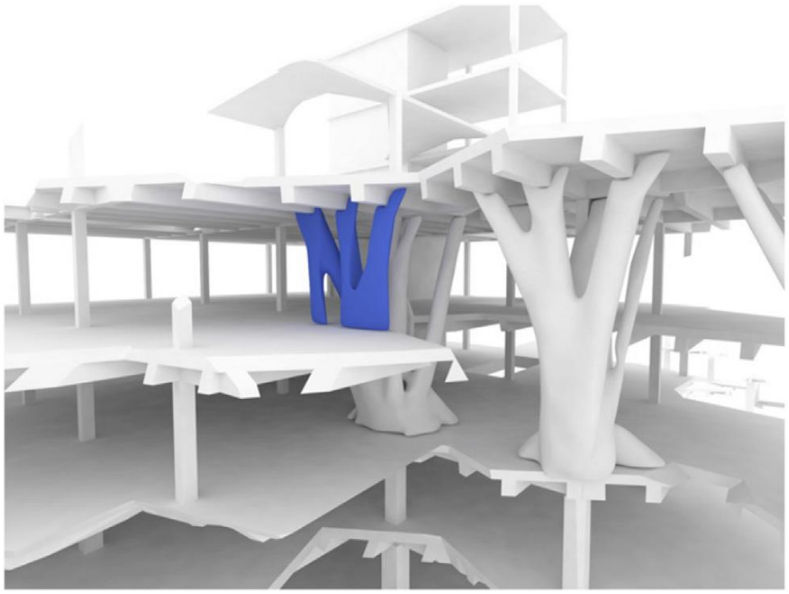

Figure 1. 2 An Ultra-High-Performance Structure with Complex Geometric Shapes Designed by Gosselin et al., [6]

Moreover, researchers have found that 3DP could benefit from following the unconventional and natural inspired patterns and suggested different printing patterns boost the structural integrity of 3D printed concrete. Among investigated patterns, the quasi-isotropic demonstrates significant influences in both compressive and flexural responses

of 3D printed concrete samples. For the same material mix, by changing the printing patterns from the unidirectional to cross-ply, quasi-isotropic, and helicoidal patterns, it is observed an increase of up to 26.5% in the compressive strengths of samples [7].

The 3D printing techniques can also be used for optimized topologies, where the material can be deposited only to the place where it is needed from structural analysis. This advantages the optimum use of materials and reduces the excessive structural self-weight.

Multiple Materials on Same Member

As shown in Figure 1.3, different materials in a same structural member may be used in 3DP of concrete. For instance, variability of material according to the stress distribution on that particular structural member can be used. The quantity of different materials can be controlled by computer system which is an integral part of 3DP. Which leads to the materials optimization in various region of structures and adorns it. Use of different color ink (mix) in the 3DP saves the use of extra painting in the structures.

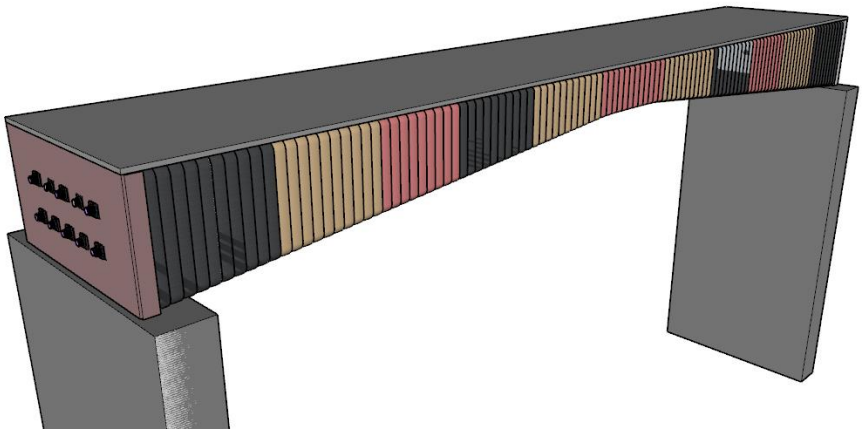

Figure 1. 3 Use of Different Materials and Different Color in 3D Printed Bridge (Animated)

Construction Time

Previous studies have shown that construction with 3DP technology can reduce 50–70% of production time [9]. It does not require the preparation of formwork which usually takes several weeks, 3DP significantly reduces the wait time in construction. Due to the speed of construction, 3D printing of concrete construction is one of the viable option for post disaster recovery program, where many people need rapid shelter.

Construction Cost

The construction cost of the structure has changed with the innovation of 3DP of concrete structures. Conventional construction cost includes mainly labor cost, material cost and equipment cost. The labor cost accounts for more than half of the cost of conventional construction, the material cost and equipment cost separately account for about 20%. For 3D printed concrete, the material cost is increased to about half of the total cost, the labor cost is reduced to about 35%, and the equipment cost is about 20% [8]. The change in cost of construction is due to the use of formwork in the traditional construction. Although in latest time use of steel formwork have alleviated the formwork cost somehow, however there is still use of single used timber formwork which surges the cost of construction.

However, primary feature of 3DP of concrete is formwork free construction which significantly reduces the cost of construction. Moreover, in traditional construction, wastage of materials is a key parameter to escalate the construction cost, however in 3DP of concrete there is no over engineered construction material wastages which also corroborates the reduction in construction cost. In relatively early day, when the 3DP of concrete is in its fledgling stage, there might be chances of higher equipment cost, but when

the 3DP of concrete becomes omnipresent in the construction industry, the equipment cost will be lower than the equipment cost in traditional construction. In summary, the total cost of the 3DP of concrete is lower compare to the conventional construction.

3DP of Concrete in Harsh Environment

Some instances involves the printing of concrete in chemically harsh environment to repair the sewer channels, deep gorge where involvement of human is potentially dangerous. 3DP of concrete can be use in those difficult situation to repair those or renovation of structures. In some adverse weather conditions, 3DP of concrete maybe useful where involvement of human labor is challenging.

1.2 Ultra-High-Performance Slurry Infiltrated Fiber-Reinforced Concrete (UHP-SIFCON)

Stiff fibers are placed in a mold to its full capacity and then slurry of cementitious materials is added from the top in gravity flow accompanied with surface vibration called slurry infiltrated fiber concrete. Maximum possible fiber can be arranged in SIFCON so that maximum possible mechanical properties (strength and ductility) of the resulting concrete can be obtained. The fiber content may range from 5% to 20% of the volume of concrete for long randomly oriented fibers and short oriented fibers respectively. SIFCON is different from conventional fiber reinforced concrete. Pre placed fiber in the mold creates voids inside it, generally maximum particle size of materials used should be one fourth of the minimum size of the voids created to ensure the complete infiltration of cementitious slurry. Because of high fiber volume fraction and small size particle paste with high strength the post cracking strength and ductility is substantially higher than conventional fiber reinforced concrete.

SIFCON was first introduced in Haynes in 1968 with the infiltration of high content of Portland cement based composite [54]. Lankard and Newell 1984 used the concept of SIFCON in construction pavement overlays. Later in 1990s Naaman and team comprehensively studied the properties and applications of SIFCON. SIFCON is relatively new material however it has already been used in some of the construction projects since early 1980s.

1.2.1 Distinction between SIFCON and Ordinary Fiber Reinforced Concrete

SIFCON differs from ordinary fiber reinforced concrete in many different ways. In ordinary fiber reinforced concrete the fiber volume fraction is limited to only 3% of the volume of the composite. In SIFCON depending on the fiber type and its size, fiber volume fraction can be attained as much as 30%. Fibers are directly added to the paste of concrete in the ordinary fiber reinforced concrete with V_f less than 3% however as the fiber volume increases it makes it difficult to mix such a higher volume of fibers. So the fibers are preplaced in a mold and a slurry of concrete is added from the top. The slurry should be flowable enough to be infiltrated and the particle size should be a fine-grained mortar. But the ordinary fiber reinforced concrete applies to any type of matrix. So from a new failure behavior is introduced in SIFCON, where fibers in the SIFCON are mechanically and frictionally interlock in addition to the usual bond of the matrix. In SIFCON, the matrix plays the role of not only transferring the force between fibers by shear but also acts as a bearing to keep the fibers interlocked [53].

1.2.2 Mixing Limitations of Fiber Reinforced Concrete

The fiber volume fraction (V_f) is the total volume of fiber per unit volume of the concrete materials. Generally in fiber reinforced concrete, the volume of matrices is at higher end nearly (97-98) % where as volume of fibers is at lower end nearly (2-3) % of the volume of total mix due to the mixing limitations. The fiber volume fraction depends on fiber length, diameter, aspect ratio, types of fibers (straight or hooked or twisted), mixing process, particle size used and flowability of the paste. ‘‘In the process of pre-mixing the fibers with the matrix in conventional mixers, fine diameter micro synthetic fibers (PP, Kevlar, Carbon, Spectra) are extremely difficult to mix in volume fractions larger than 1.5% to 2% (Naaman, 2017)’’. Longer length, smaller diameter, higher aspect ratio, hooked fibers lower the fiber volume fraction (V_f) and higher particle size used in mix, higher viscous paste increase the mixing load and hinder the mixing of the fibers in concrete paste. For more than 3% fiber volume fraction(V_f), it is difficult to premix fiber with concrete. In some cases, it is needed to have higher fiber volume fraction (V_f) to achieve desirable concrete property. In those circumstances, formwork or mold is filled with fiber and slurry of concrete paste can be infiltrated later, called Slurry Infiltrated Fiber Concrete (SIFCON). Depending on the fiber type, dimension and aspect ratio of the fiber, the SIFCON can be produced with the fiber volume fraction of 5% to 30% (Homrich and Naaman, 1987 [53]; Naaman et al. 1991 [56]).

1.3 Organization of Thesis

The thesis is divided into 5 chapters and they are summarized below.

Chapter 1 provides the introduction of AM-UHP-FRC and SIFCON, necessity and attraction towards additive manufacturing and distinction between SIFCON and ordinary fiber reinforced concrete.

Chapter 2 defines the literature review on development of additive manufacturing and properties of 3D printed concrete. This chapter also describes the development of SIFCON and its application.

Chapter 3 is divided to six different sub sections.

Section 3.1 describes the experimental program for development of proprietary AM-UHP-FRC Mix and its mechanical properties. Section 3.2 describes the experimental program for development of SIFCON and its mechanical properties. Section 3.3 describes the direct tensile testing of UHP-FRC for large scale specimens. Section 3.4 describes the early-age shrinkage control of UHP-FRC. Section 3.5 describes the performance of UHP-FRC at elevated temperature. Section 3.6 describes the development of ultra-light weight UHP-FRC.

Chapter 4 summarizes the results and conclusions obtained from the study.

2 LITERATURE REVIEW

2.1 Development of 3D Printing of Concrete

The basic sciences behind 3D printing came from the selective deposition of materials in 3D dimensional space. The core of this process involves recursive deposition of a thin layer of different powder or solid materials be added incrementally and eventually grown or assembled into the desired shape and material composition. From a material handling perspective, this technique is akin to the age-old tradition of sand painting practiced for centuries by Tibetan monks and Navajo Indians [1]. Pegna (1997) performed this investigation for the first time where it's the potential application to construction automation. Small masonry structures were produced by selective deposition of alternating thin layers of sand and Portland cement that were then cured with steam. Each layer's geometry had the desired cross-section of the structure. The geometry of each layer is obtained directly from slicing a geometric computer-aided design (CAD) model. Each slice of the model contains information about the geometry and material composition of the cross-section. Eventually, the whole structure was built recursively out of multiple thin layers of mortar. This experiment corroborates the onset of the layer deposition technique for the automatic fabrication of large-scale structures.

Khoshnevis, a researcher at the University of Southern California, in 2004 [7] developed the concept of contour crafting that uses a gantry system to deposit each layer of low slump concrete to build the house and attracted the attention of many researchers towards the digital fabrication. The same technique has been used by Yingchuang Building Technique (Shanghai) Co., Ltd. (Winsun) Stampler, (2015) [30] and built a nearly 12,000 square-foot,

five-story apartment building and three-story mansion that were constructed using a 500-foot-long 3D printer. The same company printed a 2,600-square-foot, single-story office building in Dubai. This broadened the thinking horizon for 3D concrete printing and its application.

2.1.1 Development of Fiber Reinforced Cementitious Composite for 3D Printing

Implementation of 3D printing of concrete technique is still in rudimentary stage and only limited to laboratory prototype. Several challenges should be overcome before it can be fully utilized in the construction industry. There are still limited 3D printable concretes available at the proprietary and non-proprietary levels. Successful development of 3D printable mix requires an understanding of rheology and thixotropic behavior of fresh concrete mix. Having the negligible tensile capacity, and high propensity for shrinkage and temperature cracking on concrete, it is mandatory to find a suitable reinforcement strategy before it is fully implemented in the construction industry. Several studies have been carried out to find a suitable way to reinforce the 3D printed concrete as described in section 2.1.2. Another way to self-reinforce the concrete mix is using short fibers and many researchers have shown great interest in it.

Le et al., 2012 [36] developed the 3D printable concrete mix using 12/0.18 mm length/diameter polypropylene to reduce shrinkage and early age deformation in concrete. They use cement type I, fly ash, and silica fume as a binder in a proportion of 70:20:10, and sand with maximum size 2 mm. Having a low water binder ratio of 0.26, 1% Superplasticizer has been used as water reducer and 0.5% retarder used to prolong the open time. The mix was consistently able to print for 61 layers with a 9 mm nozzle for 100 minutes of open time. The developed mix performed very good in compression with 28

days compressive strength of 100 MPa (14.5 ksi). 1.2 kg/m3 of polypropylene fiber was used to resist the shrinkage cracking but not to enhance ductility and mechanical performance.

Hambach and Volkmer (2017) [38] studied the effect on the 3D-printed composite of Portland cement paste by reinforcing short fibers (carbon, glass, and basalt fibers, 3-6 mm). They reported increasing the fiber volume content (exceeding about 1.5 vol. % fibers) caused frequent blocking of the extrusion nozzle so they used 1 vol. % of fiber reinforcement throughout the experiment. They achieved the highest flexural strength value of 30 MPa (4.35 ksi) by the optimized print path and using 1 vol. % of carbon fiber. Glass fiber and basalt fibers were not found to increase the flexural strength significantly. They mentioned that the print path and fiber alignment along the print path leads to a remarkable increase in flexural/ tensile strength of the printed structures in a designated direction. According to their observation, although tensile and flexural strength was influenced by the print path and fiber alignment, there was a minor influence on compressive strength. They added the different fiber types do not influence the compressive properties significantly. They reported the highest compressive strength they achieved was 80 MPa (11.6 ksi).

Nematollahi, et al., (2018) [37] developed Geopolymer-based 3D printable fiber reinforced concrete using polypropylene fiber. They used four different fiber contents: 0.25, 0.50, 0.75, and 1.00% by volume. They observed that the mixture with an alkaline solution/FA of 0.380 could not accommodate 1 vol. % of fiber; it appeared dry and too stiff, which can be traced to liquid sorption of fine fiber as well as its lattice effect. Such a high dosage of

fiber affected the fiber dispersion and formation of lumps. They increased the alkaline solution/FA to 0.467 to have a 1% fiber dispersed in the mixture. They concluded that fiber reinforcement increases the ductility of the material., Increasing the fiber content leads to an increase in both the deflection capacity and fracture energy. Specimens containing 0.75 and 1.00 vol. % fibers showed deflection-hardening behavior, whereas those with 0.25 and 0.50 vol. % fibers exhibited deflection-softening behavior. They also reported that while increasing the finer content increases the shape retention ability however at the same time increasing the fiber content decreases the interlayer bonding to some extent. Salet et al., (2018) designed and printed a concrete bridge starting with the capabilities of the 3D concrete printer at TU/e as shown in Figure 2.1.

Figure 2. 1 3D Printed Concrete Bridge (Salet et al., 2018)

Soltan and Li (2018) [39] developed a self-reinforced cementitious composite for building-scale 3D printing. According to them, the design was based on that of engineered cementitious composites, which include dispersed short polymer fibers to generate robust tensile strain-hardening. They used type I cement, fly ash, and calcium aluminate cement as cementitious material and reinforced by 2% by volume polyvinyl alcohol (PVA) fiber cut to 12 mm. They reported maximum tensile strength of 4 MPa (0.58 ksi) and approximately 4% tensile strain.

Ogura et al., (2018) [41] developed the Strain-Hardening Cement-Based Composites (SHCC) for 3D printing of concrete. They used cement, silica fume, and fly ash as cementitious material with a very low water to binder ratio of 0.22 to 0.24. 0.012 mm diameter and 6 mm length High-Density Poly Ethylene (HDPE) microfiber were used in different fiber volume fractions. According to Ogura et al., (2018), the HDPE was carefully chosen instead of less expensive fiber PVA taking into consideration of the superior mechanical performance of HDPE fiber which enables the use of a high-performance cement-based matrix without compromising the strain hardening performance of the composite. Such composites exhibit higher compressive strength, Young's modulus, tensile strength, and lower drying shrinkage, which are positive features of the matrix. They purposefully used fine sand with a maximum particle size of 1.0 mm which is uncommonly large for SHCC, to achieve higher yield stress of fresh mixture and consequently to get the higher shape stability. Moreover, they used a poly-carboxylate-based superplasticizer having a density of 1.06 g/cm^3; 2.0% by mass of binder. They reported superior mechanical performance as 5.7 MPa (0.82 ksi) tensile strength, 3.2% tensile strain, and 105 MPa (15.3 ksi) maximum compressive strength. They observed, printed specimens exhibited superior

strain-hardening behavior and more pronounced multiple cracking in comparison to mold-cast specimens made of the selfsame SHCC mixtures. This might be the absence of large air voids in printed specimens due to compaction in the print head and the favorable orientation of fibers as a result of the extrusion process. Besides, Ogura et al., (2018) performed the effect of sand/binder (S/B) ratio for extrusion force and found that increasing the S/B increases the extrusion force as shown in Figure 2.2. This is because higher relative sand content at lower relative binder contents means more inter-particle friction, which subsequently leads to higher plastic viscosity of concrete and higher frictional resistance at the concrete-extruder wall interface. At the same time, higher sand content also increases the probability of the sand particles' interlocking at the piston/wall interfaces. They observed, a rubbing noise from the interface during extrusion of Mixture A was loudest. As a consequence Mixture C with the lower S/B ratio showed lower extrusion load in comparison with Mixture A and Mixture B. Increasing W/B at a constant S/B ratio as well as constant fiber and superplasticizer content leads to further decreases in the extrusion force, as observed for Mixture D in comparison to Mixture C.

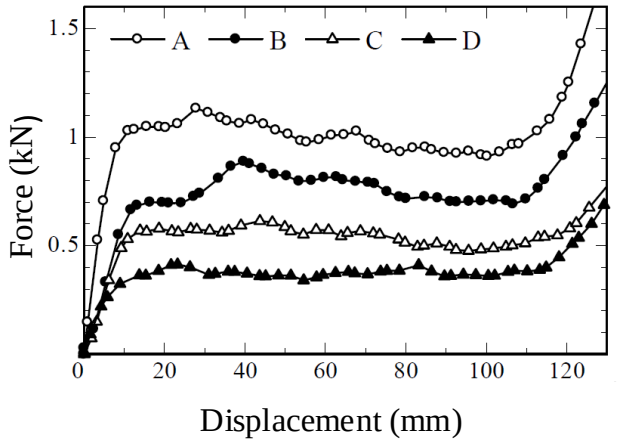

Mixture	W/B	S/B
A	0.24	1.2
B	0.22	0.5
C	0.22	0.2
D	0.24	0.2

Figure 2. 2 Force vs. Piston Displacement Curves Obtained in Ram-Extrusion Tests (Ogura et al., 2018)

Yiwei et al., 2019 [40] developed 3D printable fiber reinforced cementitious composite (3DPFRCC) using ordinary Portland cement, natural river sand, class F fly ash, and un-densified silica fume and polyvinyl alcohol (PVA) fibers having 40 μm diameter and 8 mm in length. They observed the extent of spalling of concrete while testing for an elevated temperature of 950 degrees Celsius. They observed that the developed 3DPFRCC can maintain its structure after the spalling test, and only small cracks were be found on the specimen surface. They reported that the developed 3DPFRCC is suitable for engineering applications due to its good printability and mechanical properties under both normal and elevated temperatures.

Figueiredo et al., (2019) [42] developed two mixes of 3D printable strain-hardening cementitious composite (SHCC). Both mixtures were reinforced with 2% by volume of polyvinyl alcohol (PVA) fibers. The first mixture matrix was composed of ordinary Portland cement (OPC), blast furnace slag (BFS), and limestone powder (LP), while the second reported mixture is composed of OPC, fly ash (FA), and sand. For both mixtures, the fiber reinforcement increased considerably the initial bulk and shear yield stresses and they reported the maximum tensile stress and strain is 3 MPa (0.44 ksi) and 1.2% respectively. They found that multiple cracks were observed in the mix having smaller particle sizes. This explains that the size of aggregates influences the number of cracks and the crack patterns since larger aggregates can also make the dispersion of fibers more difficult, decreasing the number of fibers effectively bridging the cracks.

Zhu et al., (2019) [43] developed 3D-printable engineered cementitious composites (ECCs) exhibiting ultra-high tensile strain capacity of more than 8% and tensile strength 5.7 MPa

(0.83 ksi) using high strength and high modulus PE fibers on Portland cement-based composite. They used Portland cement, fly ash, and sulfo-aluminate cement as a binder and fine sand having a maximum particle size of 300 μm. They added hydroxyl-propyl methylcellulose (HPMC) in the mix and reported HPMC helped to increase the shape retention ability of the resulting mix. They reported the maximum compressive strength achieved was 51.1 MPa (7.4 ksi) and maximum flexural strength 19.4 MPa (2.8 ksi). They reported the uniaxial tensile performance of the 3D printed ECCs was superior to that of the conventionally mold-cast ECCs. The underlying reasons for such behavior can be the optimized fiber orientation, making them more parallel to the direction of force, as compared to the random distribution in the case of the conventional mold-casting process. Also, they stated SEM analysis showed that the 3D printing process also improved the microstructure of the ECC matrix to have pores with more uniform size and narrower distribution.

2.1.2 Reinforcement Strategies for Additive Manufacturing of Concrete

Additive manufacturing of concrete opens the track for the many new possibilities of concrete structures to digitize the concrete construction industry. Technological and material development has advanced to a greater extent however it is still fledgling in reinforcement strategies of 3D printed concrete structures. Therefore the additive manufacturing is quite popular in architectural components and has not advanced in most of the load-taking elements. Researches have been done reinforcing the additive manufacturing concrete with a different type of fibers in the mix which generates the post cracking tensile strength still maintaining the architectural freedom however it is still not sufficient in all the cases. The successful inclusion of tensile reinforcement in the 3D

printing of concrete allows the structures to be designed for structural loads and broadens its applicability.

Xu et al (2020) [24] printed and assembled the whole pedestrian bridge keeping the concrete predominantly in a state of compression. They printed 44 circular arch with uniform cross-section staggered in 4 rows that were assembled on-site that demonstrated the use of 3D-printed concrete structural components in a real-world project.

Researchers have tried to apply post-tensioning as a form of reinforcement in the 3D printed elements. Theo et al., (2018) [25] printed multiple elements of the bridge and assembled them at the Eindhoven University of Technology (TU/e) in 2017. The bridge consists of printed elements that are rotated 90° after printing, and then pressed together by post-tensioned prestressing tendons. Prestressed tendons are placed in the openings of the printed elements, stressed, anchored at the beginning and the end, and finally released. The printed concrete elements are stressed to a level that only compression remains in the section, and no additional passive reinforcement in that direction is required. The main advantage of this approach is that the lack of tensile strength of concrete is overcome, without a need for reinforcement.

Gebhard et al., (2020) [26] used the aligned interlayer reinforcement where fibers are placed in between the different layers of digitally fabricated concrete as shown in Figure 2.3. Due to the separate placement of fibers, the size of the fiber is limited by the geometry of the layer, not by the pumping constraints. In this method, a nozzle extrudes the concrete and at the same time fibers are placed either manually or something mounted on the same nozzle. This process allows to align the fibers in the direction of expected tensile stresses

and grade the fiber concentration according to the structural requirements. Fiber alone may not be sufficient so after the production, post-tensioning reinforcement is applied perpendicularly to the interlayers to compress the concrete and carry the main loads. Aligning the fibers in between the layers results in a higher tensile strength as the efficiency of the fibers can be increased. Homogeneous and automation of fiber placement is one of the key challenges and should be developed further. This reinforcement strategy has proven to provide shear reinforcement.

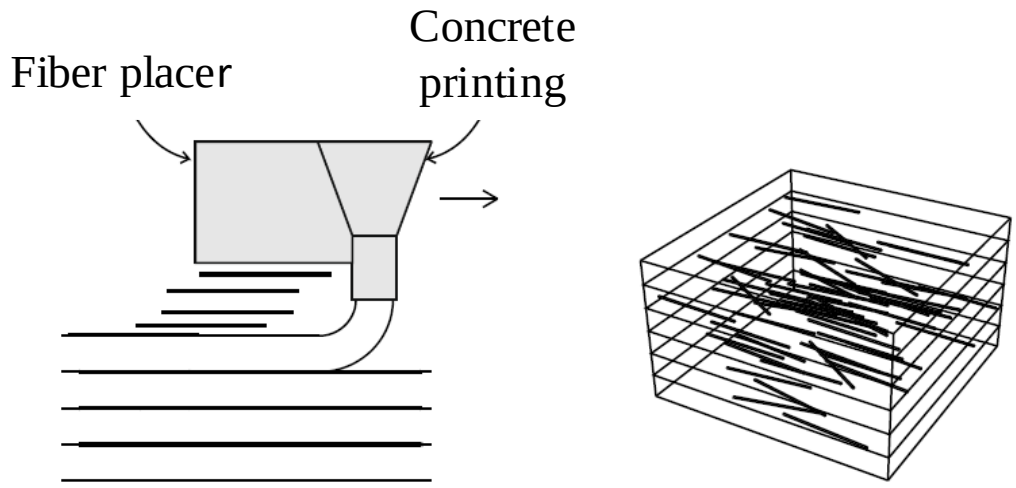

Figure 2. 3 Sketch of Reinforcement Strategy (Gebhard et al., (2020))

Norman Hack of ETH Zurich and Willi Viktor Lauer of the Future Cities Laboratory (FCL) [27] at the Singapore-ETH Centre for Global Environmental Sustainability (SEC) developed 'mesh-mould' as an alternative to conventional formwork and reinforcement strategies. In this technique, as shown in Figure 2.4, concrete is poured into double side fine mesh and it protrudes through the mesh and covers the formwork and the surface are manually troweled, leaving behind a smooth concrete surface. The mesh reinforcement depends on mechanical performance requirement. This techniques is efficient only if the

same elements are repeated over and over again. In this process concrete is continuously poured inside the mesh which reduces the potential layering issue unlike layer extrusion process.

Figure 2. 4 Mesh Mould Technique of Reinforcement in Digital Fabrication (Hack et al., 2015)

Asprone et al., (2018) [28] mentioned concept currently under development at the TU/e, is the direct in-print entrainment of reinforcement cable into the concrete filament during printing. Embedded cable provides longitudinal tensile strength as well as ductility through the layer interface. In this method, the reinforcement cable should be flexible enough to follow the layered printing path in addition to the strong and ductile. It should be ensured that there is sufficient adhesion between the reinforcement cable and printed concrete.

Yingchuang Building Technique (Shanghai) Co., Ltd. (Winsun) [29] uses the concept of passive reinforcement using the conventional steel elements where 3D printed element acts as external formwork. The casting of concrete layer wall in which layers are printed with printer and reinforcement ties are inserted manually.

2.1.3 Yield Stress of 3D Printable Mix

Rheological property is one of the essential properties of 3D printed mix that determines the workability, pump-ability and extrude-ability, buildability, and hardened material properties. Concrete exhibits a time-dependent rheological behavior, it behaves as liquid initially and becomes solid after getting it hardened. 3D printing concrete mix behaves like a liquid when the stress applied is greater than a critical value is applied so that it can flow through the extruder and it behaves as solid when no stress is applied after extruded from the nozzle. It exhibits a thixotropic behavior since the resistance to flow increases with increasing the rest time. Thus it behaves as solid with viscoelastic effect when the applied stress is smaller than certain critical stress and it behaves as a viscous liquid when the applied stress is greater than critical stress, called yield stress of material [32]. When the stress caused due to its self-weight and external forces exceeds its yield stress, the deposited layers suffer the deformation and collapse. Thus identification of yield stress of mix helps mix designers to optimize the vertical build-up rate.

Lex et al., (2018) [47] studied the role of early age structural build-up in digital fabrication with concrete and mentioned that in the layer extrusion process, the yield stress of the concrete should be at least 150 Pa to support the typical layer height of 1 cm and prevent

the flow. Similarly, for the slip forming process, the yield stresses the time of casting should be around 20 Pa for self-compacting and it should transition to self-supporting. Yield stress should be developed at least equal to the weight of the upper layer. When the weight of the accumulated layer increases the yield stress of the lower layer, the lower layer starts to flow and forms the distortion in the shape. This requires waiting until the lower layer gain sufficient yield strength before the upper layer can be deposited. This increases the open time of concrete. On the other hand, increased open time decreases the interlayer bonding capacity.

Joshep et al., (2014) [34] used direct shear test to find the yield stress of cement paste materials. Lootens et al., (2009) [33] used penetration test to find the yield stress of cement paste. Q.D. Nguyen et al., [35] used vane method to measure the direct yield stress.

2.1.4 Topology Optimization

According to Vantyghem et al., (2020) [31] "Topology optimization is a class of computational tools that can be used to optimize the layout of materials in a certain design domain so that an objective function is optimized subject to design and behavioral constraints." Additive manufacturing can be used to deposit the concrete material at the predefined path so that the resulting shape is topologically optimized. Topology optimization has already gained popularity in the aerospace industry due to the reduction of the structural weight of optimized shapes. The same concept can be used in the construction industry. Vantyghem et al., (2020) [31] used the density-based approach for topology optimization of the bridge girder and printed a bridge as shown in Figures 2.5 and 2.6. They used the finite element analysis tool to optimize the concrete girder and the

resulting shape was 3D printed. The whole bridge was printed on a different segment, assembled by applying the post-tensioning, and tested. The following figure 2.5 shows the optimized shape where black represents the concrete and white represents the voids and cyan represents the tendon. Based on the performance of the optimized beam, in terms of mid-span deflections under self-weight and live loads, they predicted material savings of roughly 20%. This study demonstrates the beneficial use of 3D printing on material saving. The negative impact on the environment due to excessive use of concrete and cement production motivates topology optimization.

Figure 2. 5 Topology Optimized Concrete Bridge Girder (Vantyghem et al.,2020)

Figure 2. 6 Topology Optimized Concrete Bridge Girder Subjected to Post-tension (Vantyghem et al. 2020)

2.1.5 Interlayer Bond Strength

The interlayer bonding mechanism between two consecutive layers mainly depends on three factors, namely adhesion of concrete, friction, and mechanical interlock between two layers [52].

Adhesion of concrete is a chemical bond and it depends on the mixer's physical and chemical characteristics. It can be optimized by the optimum time between two layers and optimizing the mixer properties. The friction mechanism against the slip at the interface plays its role right after the adhesion mechanism disappears. After the adhesion and friction mechanism disappears, mechanical interlock between layers plays its role and holds the layers together. The mechanical interlock depends on surface roughness and its texture. The surface roughness depends on several factors such as the properties of the material of the mix, shape, and size of aggregates, particle size distribution. Studies have been conducted to strengthen interlayer bonding and its characteristics.

Le et al., (2012) [44] examine the tensile bond strength of developed high-performance printing concrete at Loughborough University and observed the failure outside the bond region. Which depicts the sufficient bond capacity. Their obtained result was quite common, as increasing the open time from 0 min to 15 min decreased the bond strength by 70%.

Nematollahi et al (2018) [45] studied the Effect of Type of Fiber on Inter-Layer Bond and Flexural Strengths of Extrusion-Based 3D Printed Geopolymer and observed that the incorporation of fiber reduced the interlayer bond strength of 3D printed Geopolymer. They

incorporated three types of fibers namely polyvinyl alcohol (PVA), polypropylene (PP), and poly-phenylene benzo-bisoxazole (PBO) fibers however the pattern was similar regardless of the type of fiber. They mentioned, the plain Geopolymer mix without fiber (GP-Plain) exhibited the highest inter-layer bond strength. The inter-layer bond strengths of GP-PBO, GP-PVA, and GP-PP containing different types of fibers were 23%, 15%, and 20%, respectively, lower than that of GP-Plain. Although the observed interlayer strength was low, it was sufficiently high to prevent interfacial shear failure. The lower inter-layer bond strength of the 3D printed fiber-reinforced Geopolymer may be due to the higher stiffness of fresh fiber-reinforced mixtures owing to the inclusion of the fibers. The increased stiffness of the fresh mix reduced the ability of the freshly placed layers to deform and form a seamless interface.

Similar to Nematollahi et al (2018) [45], Al-Qutaifiet et al., (2018) [51] also found that the incorporation of fiber in the 3D printed mix decreases the interlayer bonding. They interpreted that, drop in interlayer bonding is due to the protrusion of some steel fibers between subsequent layers which impeded the complete adhesion between two additive layers. They observed that a drop in bond strength also affects the flexural performance of the 3D-printed specimens. Insufficient bond strength was not able to distribute the applied load equally throughout the different layers so that the layer with weaker bond strength started to crack first and propagated to the whole element.

Yi et al., (2019) [50] studied the time gap effect on bond strength of 3D-printed concrete and its correlation with tensile strength. They observed that the direct tensile strength dropped logarithmically with increasing the time gap. The drop in strength is significant in the initial time for 1-5 minutes and it is insignificant after 10 minutes. As the time

increases, the overall stiffness of the lower layer increases but the stress induced by the upper layer is the same for all time gaps which causes less disruption in the lower layer. This causes lesser intervention between subsequent layers and ultimately weakens the interlayer bonding. Moreover, they observed that there are almost no obvious voids between two subsequent layers with the time gap of 1 minute and the voids appeared and increased with time. Yi et al., (2019) concluded that the interfacial zone is sensitive when the time gap is short so that the bottom substrate rearranges its orientation due to the stress caused by the upper layer. However, as the gap increases the energy induced by the deposited layer is insufficient to rearrange the orientation of the interface thus voids appear. The author of this research also observed similar behavior and explained it in the section 3.10.

2.1.6 Early Stage Failure Mode of 3D Printable Concrete

Wolfs et al., (2018) [46] studied the early age mechanical behavior of 3D printable concrete in the range of 0 to 90 minutes. They performed the unconfined uniaxial compression test and direct shear test of concrete at different time intervals from 0 minutes to 90 minutes. Both the tests, uniaxial unconfined compression tests, and direct shear tests were performed on cylindrical samples. They have reported the early age failure mode is bulging because of relatively low stiffness so that the early age specimens expand in the lateral direction as vertical deformation increases. However, older specimens showed less expansion in the lateral direction and showed more distinct plane failure formation. In this study, they observed that Young's modulus, compressive strength, and shear strength were a linear function of time, and develop proportionally with fresh concrete age.

2.1.7 Hardened Properties of 3D Printed Concrete

2.1.7.1 Density

Le et al., (2012) [44] compared the density of 3D printed specimens and normally cast specimens and found that printed elements have a slightly higher density than normally cast concrete. The density of normally cast specimens was found to be 2250 kg/m^3 (140.4 lb. /ft^3) while the density of 3D printed specimens was 2350 kg/m^3 (146.7 lb. /ft^3). This was probably because the concrete hopper was gently vibrated before delivery of the fresh concrete, and the pipe and pump system also provided a small pressure during extrusion.

2.1.7.2 Compressive Strength

Le et al., 2012 [44] studied the compressive strength of 3D printed specimens and normally cast concrete. 100 mm printed elements were extracted from a slab and tested in different loading directions. The compressive strength of 3D printed specimens with loading perpendicular to the cutting surface and loading perpendicular to the printing surface was similar to the compressive strength of standard mold cast specimens. However, the compressive strength of 3D printed specimens with loading perpendicular to the side surface was found to be 15% lower than standard mold cast specimens.

Binrong et al., (2019) [43] developed 3D-printable engineered cementitious composites (ECCs) and studied the compressive strength of conventionally cast ECC and 3D-Printed ECC (3DP-ECC). They observed that the compressive strength of 3DP-ECC was 2-12% lower than that of corresponding mold cast specimens depending on the fiber content. The lower strength of 3DP-ECC might be inevitably due to the introduction of small voids in

between the consecutive layers during printing the specimens. They mention that although the slab they printed looked well, there were some small pores in the cross-sections.

2.1.7.3 Flexural Strength

Le et al., (2012) [44] studied the flexural strength of 3D-printed concrete with different loading orientations and compared it with mold cast concrete as shown in Figure 2.7. They printed a slab and cut the slab in different orientations to get the samples as shown figure. The flexural strength of printed concrete with loading directions I and II were higher than the standard mold cast concrete. However, the flexural strength of samples with loading direction III was less than the strength with loading direction I and II and also less than the traditional standard mold cast concrete. This is because the anisotropy due to the printing process and also strength is mainly dependent on the interlayer bonding.

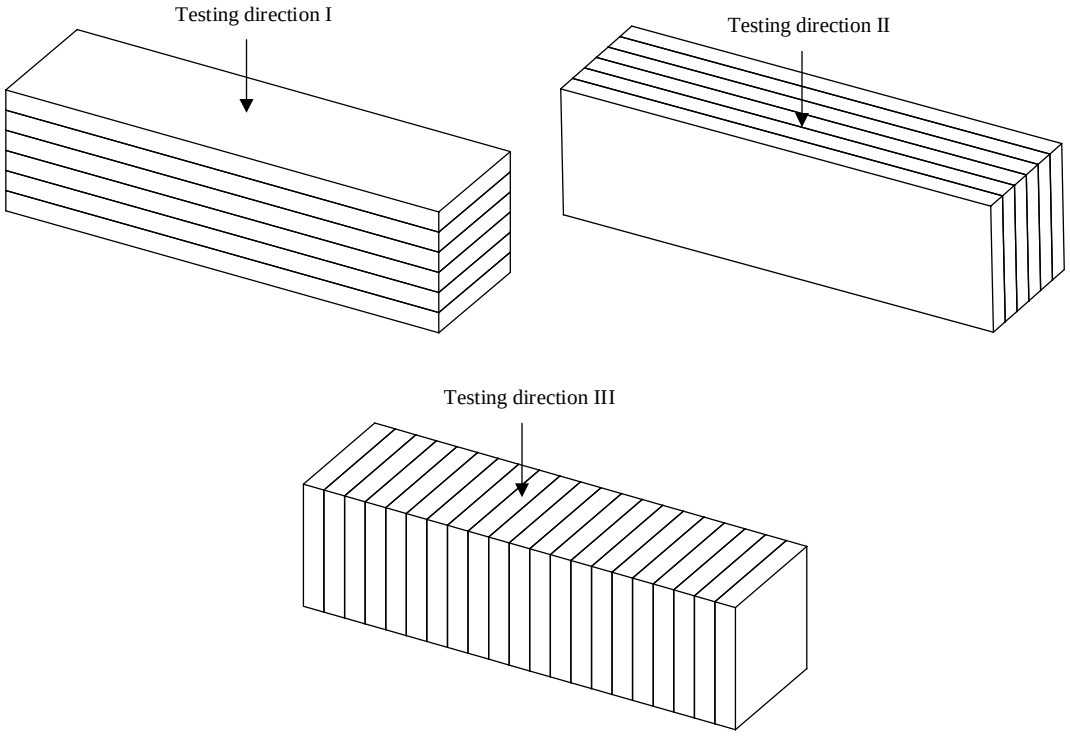

Figure 2. 7 Diagram of Cutting Slabs and Testing Flexural Strength. (Le et al. 2012)

Binrong et al., 2019 [43] developed 3D-printable engineered cementitious composites (ECCs) and studied the flexural strength of conventionally cast ECC and 3D-Printed ECC (3DP-ECC). They observed that 3DP-ECC exhibited superior flexural performance compared to the conventional mold cast ECC. They studied the 4 different ECC mixes. In one of the mixes with 2% fiber content, the ultimate tensile strength and tensile strain capacity of 3DP-ECC specimens were 6% and 14% higher than those of the corresponding mold-cast-ECC specimens. In another different mix with 1.5% fiber content, the ultimate tensile strength and tensile strain capacity of 3DP-ECC specimens were 13% and 12% higher than those of the corresponding mold-cast-ECC specimens. The superior tensile performance of 3D printed ECC is likely because there were more fibers parallel to the direction of the force. They performed the microstructural analysis using the scanning electron microscope (SEM) image and found that the number of fibers providing effective bridging stress parallel to the stress direction was much higher in the case of 3DP-ECC compared to conventionally mold cast ECC. In a statistical calculation, they observed that the number of fibers parallel to the direction of force for mold cast ECC and 3DP-ECC was 4241 and 6072 respectively. They concluded that the extrusion process can optimize the fiber orientation, making them more parallel to the direction of the force, which in return contributes to the higher ductility of the 3DP-ECC sample, as compared to the mold-cast-ECC sample.

2.1.8 Effect of Printing Pattern on Mechanical Properties of 3D Printed Concrete

3D-Printing of concrete is drawing the attention of researchers and industry personals around the globe. However, it is still limited to the unidirectional printing patterns in most of the studies to test the material properties of 3D-Printed concrete. Researchers at the

Royal Melbourne Institute of Technology (RMIT) [52] have studied the effect of different architectural printing patterns on the mechanical performance of 3D-Printed concrete and found that replicating the naturally inspired printing pattern can be beneficial in both compressive and flexural strength. Moreover, it lessens the directional dependencies of the mechanical properties of hardened 3D-Printed concrete. Pham et al., 2020 have studied unidirectional (0º), cross-ply (0º/90º), quasi-isotropic (0º±45º/90º), and helicoidal patterns (with pitch angles of 10º, 20º, and 30º) printing patterns to create unidirectional, bidirectional and multidirectional layers in printed objects with 0.75% of steel fibers and without fibers. Those architectural patterns already have been using in the fabrication of composite materials in additive manufacturing and laminated object manufacturing. Quasi-isotropic is the most used design in the aerospace industry using additive manufacturing.

As shown in Figure 2.8, they printed slabs and cut them in different directions and required sizes for the compression and flexural testing. For the same material mix, changing the printing patterns from unidirectional to cross-ply, quasi-isotropic, and helicoidal patterns, they observed an increase of up to 26.5% in the compressive strength of fibers. According to Pham et al. (2020), the increase in compressive strength may be because the change in the architecture of hardened concrete due to multiple directions of the matrix could lead to a stronger connection between layer and within the printed concrete.

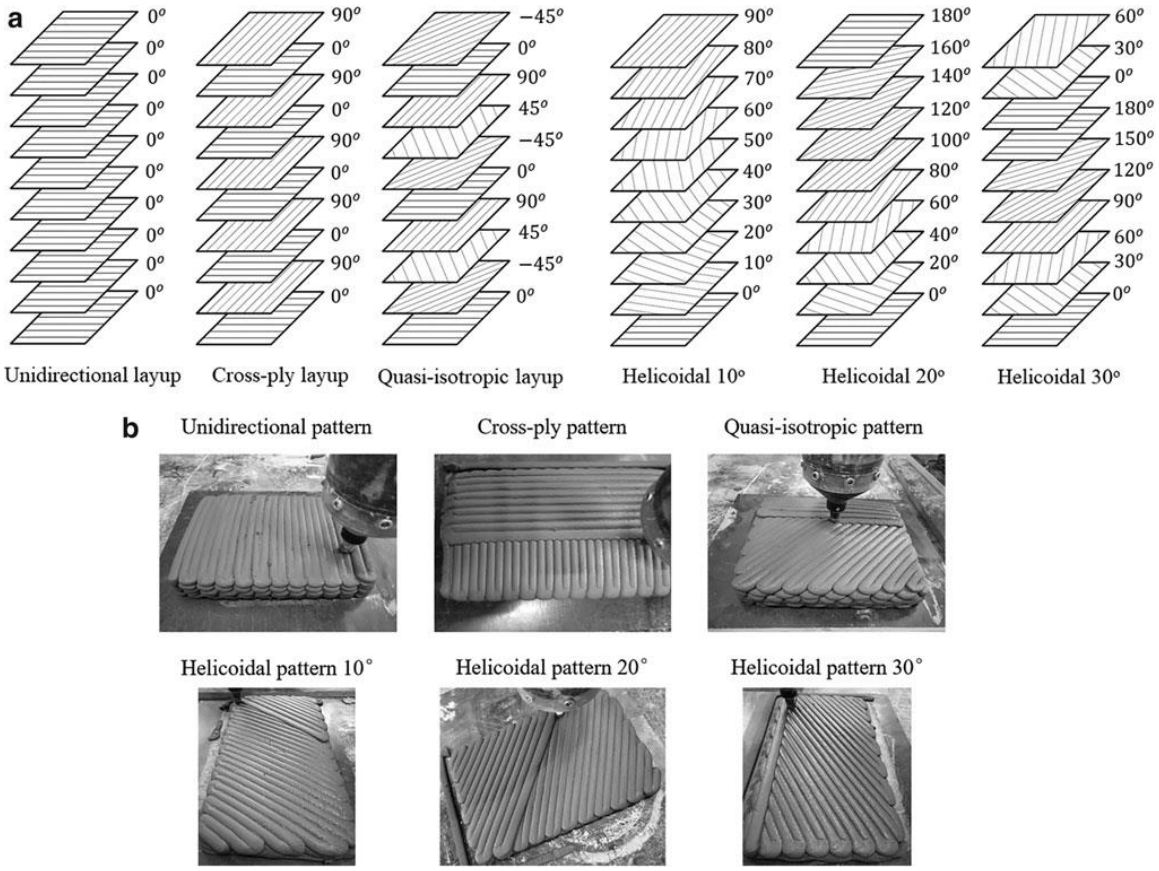

Figure 2. 8 Schematic Different Printing Patterns (Pham et al., 2020)

The multidirectional printing attributes to a firm connection within the printed sample resulting from each filament connected to multiple filaments. Well known fact that the inclusion of steel fibers in the mix increased the compressive strength of concrete in all patterns, however, the CV for the compressive strength test in the unidirectional pattern was observed highest while its counterpart without fiber has lowest. This reflects a single degree of freedom leads to a higher degree of anisotropy for the compressive strength test in the unidirectional pattern. Similar to the compressive strength, the flexural strength of specimens without fibers printed with bioinspired patterns was found to be improved in which pronounced effect was observed in the case of quasi-isotropic patterns and cross-ply

patterns. They noticed that an increase in flexural strength by 24.4% and 47.4% in the case of cross-ply and quasi-isotropic specimens. The increase in flexural strength was explained that the flexural strength is highly dependent on the tensile resistance of the first layer and crack might not propagate through the interface between filament perpendiculars to the longitudinal axis of the beam. In addition to that, the two consecutive layers stacked into two directions perpendicular to each other lead to one filament connected to many others resulting in a stronger connection compared to unidirectional layers. In a quasi-isotropic pattern, filaments are connected in multiple directions which leads to the most solid connection that boosts the flexural strength by 47.4%, which was the highest improvement of flexural strength among the studied patterns. A similar observation was found in the case of helicoidal patterns. The addition of fibers increased the flexural strength in any patterns however the pronounced effect was observed for the unidirectional pattern. Fiber alignment along the printed layer which can generate the bridging effect right after the initiation of flexural cracks is responsible for the significant increase in flexural strength in the case of unidirectional printing patterns. It was observed that rotation in any angle weakens the flexural strength in the case of fiber-reinforced printed concrete which is explained as the larger the angle of fibers rotate, the more stress is transferred through the matrix and fiber causing sudden changes in the direction of local stresses which leads to sudden failure and diminishes the effect of fibers.

2.1.9 Continuous Printing and Discontinuous Printing Process

The additive manufacturing process involves two strategies, pre-print and print in place (PIP). Print in place is similar to the cast-in-place concrete in traditional construction, is a method of 3D printing of structures where it stays for its entire service life. Because of its

onsite construction, it has limited control over curing conditions. Whereas, pre-print is a method similar to precast in traditional construction, where structural elements are printed somewhere in a static location and transported to the job site and assemblage together. Many researchers and industries have already employed the pre-print process.

Several example of segmental printing have already been implemented. Researchers at Eindhoven University of Technology, Theo et al., (2018) [25], printed different segment of bridge and assembled together applying post tension from the end, which was open for cyclist on 2017.

Eric et al., (2019) [49] printed a house called the Barracks Hut (B-Hut)-B at the Engineer Research and Development Center Construction Engineering Research Laboratory (ERDC-CERL) Champaign, Illinois USA. The area of the building is 512 ft^2 and it took continuous printing of 16.75 hours. The roof and wall, wall, and foundation was connected with the conventional techniques. The building was designed to sustain the minimum design loads specified by the ASCE 7. This experiment pushed the limits of continuous 3D printing operations.

2.2 Development of Slurry Infiltrated Fiber-Reinforced Concrete (SIFCON)

Slurry infiltrated fiber concrete was first introduced in 1979 by Lankard Materials Laboratory, Columbus, Ohio, USA, by incorporating large amounts of steel Fibers in steel Fiber reinforced cement-based composites (Lankard (1984) [57]). Steel fiber reinforced concrete (SFRC) is very difficult to mix at the fiber content excess of 2% volume. Only the SFRC with 2% volume was practiced at that time. Lankard (1984) and team examined the possibility of SIFCON and developed SIFCON where steel fiber content have been

provided up to 20% volume of concrete. Developed SIFCON has shown extremely ductile behavior in compression as well flexural loading. They observed high compressive strength more than 30 ksi and flexural strength range from 3 ksi to 7 ksi. They had attempted to test the impact resistant of SIFCON using ACI committee 544 on fiber reinforced concrete but it was not possible to cause any cracking in the most SIFCON composites which clearly demonstrates the developed SIFCON had very high impact resistance.

Naaman and Joseph (1989) [56], studied the tensile stress-strain properties of SIFCON for four different fiber volume fractions in the range of 11.7-13.8%. For a volume fraction of 12.1%, SIFCON performed direct tensile stress of 2.28 ksi with very high ductility which is 1.98 ksi residual stress for 2% equivalent strain. They experimented with hooked fiber and deform fiber and observed that the non-linearly stress-strain response of SIFCON is less pronounced in SIFCON with deform fiber. This is maybe at small tensile strain, fiber to matrix local bonding is dominants the fiber to fiber interlock of fibers.

Sengul (2018) [55] studied the mechanical properties of slurry infiltrated fiber concrete produced with waste steel fibers in which steel fibers recovered from scrap tires were used to produce slurry infiltrated fiber concrete (SIFCON).In his trial, he observed that there was a fiber bulking beyond the 5% fiber volume and he kept 5% as an upper limit of the experiment. The fiber bulking was observed because of the random orientation of intertwined fibers. For the 5% fiber volume fraction, the SIFCON attained 25.4 MPa (3.68 ksi) splitting tensile strength. For the same mix, SIFCON attained flexural strength of 63.8 MPa (9.25 ksi). This extremely high flexural strength might be due to the longer length (208 mm, 8.18 in) of fibers which led to a partial alignment of fibers parallel to the long

axis. His observation confirmed that waste steel fibers recovered from tires can be used for SIFCON production and the possibility of SIFCON.

Lankard at Lankard Material laboratory, Columbus Ohio developed SIFCON with a 12.5% fiber volume fraction that achieved ultimate flexural strength of 5.68 ksi. Based on his observation, the ultimate stress required to fail a steel fiber reinforced concrete composite in tension or flexure is controlled by the amount of fiber, fiber aspect ratio, fiber/matrix bond strength, and fiber orientation according to the following equation;

$$\sigma_{ult} = k \times V_f \times \delta \times \left(\frac{l}{d} \right)$$

$\sigma =$ ultimate post cracking tensile or flexural strength of composite

$k =$ Constant dependent on fiber orientation

$V_f =$ volume percent of fiber in the composite

$\delta =$ average sliding friction bond strength

$\frac{l}{d} = Fiber$ aspect ratio $\left(\frac{lenght}{diameter} \right)$

Wood (2001) [58] from North Carolina State University, Raleigh investigated the use of precast reinforced SIFCON flexural hinges to increase the seismic resistance of reinforced concrete moment frames. He tested seven long reinforced SIFCON hinge specimens under quasi-static cyclic loading. The fiber volume fraction was achieved from 9% to 11%. The SIFCON specimen performed outstanding performance in compression and flexure. Several specimens were reached the maximum compressive strain of over 15% and some

times more. Similarly, Strain at maximum tensile stress exceeds the yield strain of mild reinforcing steel and it reached almost twice the yield strain of mild reinforcing steel. The reinforced SIFCON hinge did not develop any flexural cracking until the mild reinforcing steel exceeded its yield strain. He observed a good distribution of cracking damage before a singular primary crack appears. Although developing multiple primary failure planes is difficult, finer distribution of cracks can be achieved. He reported that the tensile capacity of SIFCON was heavily dependent on the fiber orientation and can beneficially use the fiber alignment.

Halit et al., (2006) [59] studied the effect of incorporating high volume of Class C fly ash (FA) on mechanical properties of autoclaved SIFCON. They studied the replacement of cement in the SIFCON composition as much as 60% by fly ash for three different fiber volume fraction, 2%, 6% and 10%. They reported that the mechanical properties were positively affected with the fly ash replacement. By increasing the fiber volume fraction, the flexural strength and toughness was remarkably increased and the behavior was pronounced for 10% fiber volume fraction. The highest flexural strength reported was 7.9 ksi (55 MPa). Effect of fiber on the toughness was more impressive.

2.2.1 Slip Hardening of Bond

Slip hardening is an extremely important characteristics of some fibers. In the fiber reinforced composite, once the crack is formed, the fiber may acts as a bridging the cracks and may provide additional resistance to the crack openings (Naaman, 2017). This helps to redistribution of the force and creates the multiple cracking in the specimens and leads to

the strain hardening behavior in tension as well as large composite strains at failure. The Figure 2.9 shows the bond shear stress versus local slip curve.

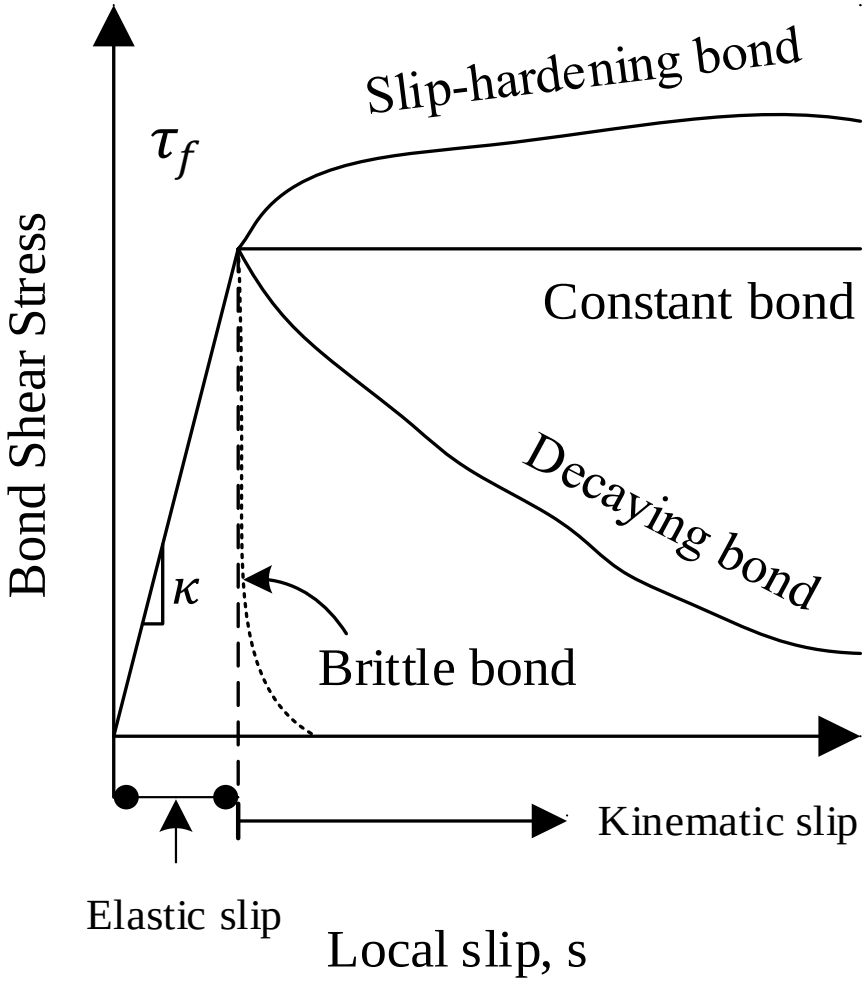

Figure 2. 9 Typical Bond Shear Stress versus Slip Curve (Naaman, 2017)

The straight and smooth fibers do not participate in the slip hardening behavior but the deformed fibers, hooked end fibers and twisted fibers participate in the slip hardening behavior. The mechanical bond, anchorage, and slip resistance characteristics of fibers contributes the slip hardening behavior of the composites. The mechanical bond of steel hooked fibers comes from the hooked ends, which contribute to bond strength through the

work needed to straighten the fiber during the pullout (Chao, 2005). Short-length fibers may perform better slip hardening slip properties than long fibers. Slip hardening characteristics have been observed with hooked end steel fibers, but hardening was limited mostly along the length of hook prior to decaying. Also, the fiber diameter and embedment length do not affect the characteristics of the pull-out load versus end slip relationship (Naaman, 2017). Although both Hooked and Twisted fibers leads to better performance with an increase in matrix compressive strength, twisted fiber showed much more sensitive behavior than hooked end fiber, that is, twisted fiber is more effective in high strength matrices than hooked end fiber. Bond stress for twisted fibers increases continuously with increasing slip, leading to slip, leading to very high bond stresses at large slips, prior to complete pull out. Maintaining a high equivalent bond strength at increasing slip is a one key feature and advantages of the twisted fiber (Naaman, 2017). For the examination of maximum bond stress with smooth steel fibers, hooked fibers indented deformed fibers, it was found that 1 to 2.8 MPa for smooth fibers, 3.5 to 7 MPa for hooked fibers, and 2.8 to 6.7 MPa for indented deformed fibers (Naaman, 2017). Torex fiber is a twisted polygonal steel fiber, which has an optimized geometry that offers a ratio of lateral surface area to cross sectional are larger than that of round fiber. An increase in this ratio of a fiber leads to a direct increase in the contributions from the adhesive and frictional components of bond. In addition, the twisted ribs create a very effective mechanical bond. Unlike conventional steel fibers, when pulled out from a cement matrix, Torex fibers can maintain a high level of resistance up to slips representing 70% to 90% of the embedded length. This unique bond behavior is due to the successive untwisting and locking of the fiber embedded portion in its tunnel of matrix during slip (Naaman, 1999).

2.2.2 Application of SIFCON

SIFCON have higher compressive strength, higher flexural strength, higher modulus of elasticity combined with high ductility which made it more suitable to impact resistant structures or resistance to explosive loading like contaminants for explosives, bank vaults, shelters and bunkers. Having a very high impact resistant it can be used as a platform for aerospace launching, where high temperature shocks and high stress gradient occur. It can be used to repair the bridge decks, airfield overlays, taxiways and potholes in pavements. Critical points in any structures where ductility and energy absorption are demanding such as plastic hinges, fuse connectors in seismic resistant structures, end blocks in highly Prestressed beams, transverse shear keys for precast bridge girders and central core in high rise buildings may utilize the superior mechanical properties of SIFCON.

However, the SIFCON is relatively a naïve construction technique it has been already implemented in the real field since the 1970s. In 1979, SIFCON was used as an overlay in a 900 square feet parking lot slab where a 1-inch fiber bed was infiltrated with cement/fly ash slurry, the slurry was poured through a vibrating steel grate to help in the infiltration process. 2-inch SIFCON slabs have been used as an impact-resistant and wearing surface over a convention PCC in Port Columbus International Airport, in October 1984. 8 ft. 10 ft. slabs had prepared and installed containing fresh Portland cement concrete. They are located within the existing AC overlay area supporting the main aircraft wheel carriages. In addition, SIFCON was used for fast and sustainable repair of bridge deck pavement in June 1984 by the New Mexico Engineering Research Institute to repair spalled areas on the decks of three Interstate highway bridges near Albuquerque, New Mexico. The slurry was infiltrated with gravity flow alone, no external vibration was applied through the

infiltration process. Because of its high compressive and flexural loading capacity accompanied by high ductility, SIFCON is being considered for the structures with explosive loading. A 1/8-scale model of a hardened silo structure was constructed of SIFCON by the New Mexico Engineering Research Institute, Albuquerque, New Mexico [57]. SIFCON is a unique engineering material with the potential application where superior ductility and strength requirement is required, and that cannot be served with the traditional fiber reinforced concrete material. The use of SIFCON in the above-mentioned projects demonstrated the constructability of SIFCON.

3 EXPERINMENTAL PROGRAM

3.1 Development of Proprietary AM-UHP-FRC Mix

The mix components have been chosen from available US market and used in this experimental program which have presented in the following table. Also the mix components have shown in the following figure. The ingredients investigated in this project include three types of ordinary Portland type I cement, ordinary Portland type III cement, and ground granulated blast-furnace slag (GGBS), fly ash, silica fumes, two types of sands, polyethylene fibers, High Range Water Reducers (HRWRs), and water.

Portland Type I and Type III cement is readily available on several major US supplier. Portland type III cement, speeds cement hydration and drives faster reaction times than Portland Type I and II cement so have a high early strength, have been used to maintain the buildability of mix. Since UHP-FRC have a lot of cement, which surges the cost of UHP-FRC also burdens on environment and ecology, GGBS is added to make the mix more environmentally and ecologically friendly. Also GGBS is byproduct of steel making industry, and have a beneficial mineral mixture it have a positive effect on the durability of concrete [12].

Fly ash is a fine powder and is a byproduct of burning pulverized coal in electric power generation plant. Being spherical in shape, fly ash increases the flowability of mix, reduces the voids and decreases the permeability and subsequently increases the compressive strength of mix. Moreover adding fly ash in large volume concrete will decrease the heat

generation from cement hydration on mass concrete placement and also reduce drying shrinkage and creep [13].

Since the addition of fly ash increases the workability but reduces the shape stability of fresh printed specimens. So the fly ash content was reduced to 15% of weight cement from the base mix.

Silica fume densify the microstructure of UHP-FRC and significantly improves the compressive strength of concrete. Addition of silica fumes improves cohesion of fresh concrete and ultimately impermeability of hardened concrete [18]. Although several silica fumes are available in market, Norchem silica fume have used throughout this research. The Norchem silica fume have relatively higher carbon content compared to other silica fumes which are available in market, it makes the mix relatively stiff, and utilized this property to make the buildable mix in AM-UHP-FRC.

Eliminating the coarse aggregates makes the concrete dense promoting the compressive strength. This research uses two types of sand 1 and sand 2 with (Coarse Sand) (400-800 Micron, and (Fine Sand) (80-200) Micron. Coarse sand is equivalent to 30/70 filter sand and fine sand is equivalent to glass sand produced by US supplier Short Mountain Silica.

The use of fiber in concrete enhances the mechanical performance of concrete in terms of tensile strength and ductility properties. The use of fiber in UHPC increases the post cracking performance, energy dissipation capacity, cracking spacing and crack width. In addition to the enhanced mechanical performance, the use of fiber acts as a shrinkage reinforcement in AM-UHP-FRC mix. Polyethylene fiber (PE fibers) have been used throughout this research, which controls the plastic and drying shrinkage cracking of 3D printed specimens. Since 3D printing

of concrete is a formwork free construction, there is high chances of rate of evaporation of water from the concrete surface. Moreover, the addition of polyethylene fiber helps to improve the shape stability of extruded 3D printed elements.

High Range Water Reducer (HRWRs) have significant impact on the fresh properties of UHP-FRC. The use of appropriate amount of HRWRs makes the UHP-FRC flowable and helps to evenly distribute the fiber in it. The excessive use of HRWRs makes the fiber segregation in the mix resulting the non-homogenous mixing and leads the porosity and resulting the lesser compressive strength. However, insufficient use of HRWRs makes the concrete stiff and make it difficult to compaction.

Table 3.1 Mix Components Used in Experimental Program

Mix Components used in experimental program		
Cement type I	0.00079 in. (20 µm)*	Any US supplier
Cement type III		Any US supplier
GGBS		Any US supplier
Fly ash	0.00079 in. (20 µm)*	Class F
Silica fume	0.00047 in. (1.2 µm)*	Norchem
Silica sand 1	0.02 in. (500 µm)*	OK75
Silica sand 2	0.0047 in. (120 µm)*	#1 Q ROK
Polyethylene fiber	0.000059 in. (1.5 µm)	UHMW PE Fiber
HRWR	Poly-carboxylate based	ADVA CAST 575

3.1.1 Methodology

This research first focuses on first developing additive-manufactured ultra- high performance fiber reinforced concrete (AM-UHP-FRC) for accelerated digital construction. Aghdasi et al., (2017) [10] developed Ultra-High-Performance Fiber-

Reinforced Concrete for Large-Scale Structural Applications. However, it was required to change and optimize the materials and their proportions. This research program uses Aghdasi, et al., (2017) as base mix and studies the different possibilities of additive manufacturing of ultra-high performance fiber reinforced concrete. While 3DP of concrete have gained the attention from the researchers and several researchers have printed the structures using different cementitious components. Binrong et al., (2019) [11] developed a 3DP mix using Portland cement (OPC), sulfoaluminate cement (SAC) based on 100% industrial solid wastes, and fly ash (FA). To the best of author's knowledge till date, no such study have been done on the 3DP of UHP-FRC. Although UHP-FRC uses variety of fibers (different types of steel fibers, polyethylene fibers), this research used polyethylene fibers (PE Fibers). This is because PE Fibers allows for easier handling and no chances of clogging inside the pump. There are limited availability of 3D printing concrete inside the US market and they are still to be customized for ultra-high performance fiber reinforced concrete, this research uses manual printer made by researchers at made at Civil Engineering Laboratory, University of Texas at Arlington. Manual printer uses the same principal of digital printer.

AM-UHP-FRC Development

a) Mix 1 (Base mix)

Aghdasi et al., (2017)[10] developed Ultra-High-Performance Fiber-Reinforced Concrete for Large-Scale Structural Applications by using the dense particle packing concept using normal mixing and curing. This mix have sufficient flowability, high compressive strength up to 30 ksi (207 MPa) [10], compressive and tensile behavior

resembles the real structure behavior. Due to the higher flowability this mix was not printable.

b) Mix 2 (Replacement of coarse silica sand by no #8 (nominal size: $\frac{3}{8}$) coarse aggregate)

The coarse sand used was replaced by coarse aggregates. The replaced coarse aggregates have smaller total surface area than coarse sand so it demands less amount of water which increases the flowability of mix. This mix was not printable because of its higher flowability. Moreover, during the printing process the concrete should be pumped from the nozzle, but the aggregate hinders the concrete to be pumped.

c) Mix 3 (Increase of PE fibers to 1% of weight of cement)

The increase in fiber was not helpful to lower the flowability of the designed mix. Because of higher fiber content, clumping of fibers in the mix was observed. Due to the high flowability and fiber clumping, the mix was not suitable for 3D printing.

d) Mix 4 (Reduction of fly ash content)

The addition of fly ash leads to better flowability without considerable dropping in compressive strength. Addition of fly ash was varied in different amount to examine the effect of this application in the mixes.20% fly ash by weight of cement caused the high flowability and the mix was not printable. And 10% fly ash by weight of cement made the mix stiff which need high pressure in the pumping during the printing process. Therefore the optimum value of 15% fly ash by weight of cement was chosen for this experimental program onwards.

e) Mix 5 (Reduction of superplasticizer content)

Poly-carboxylate based high range water reducer (HRWRs) has been used to make the paste more flowable. To achieve optimum flowability, like a high viscous liquid, a small portion of HRWR or 1.3% by weight of cement has been used through this research onwards. ADVA CAST 575 (powder form) has been used throughout this research. To get the early activation of superplasticizer, HRWR was mixed with dry materials and mixed throughout for homogeneous mixing.

f) Mix 6 (Replacement of Type I cement by Type III cement)

Initially 50% of OPC type I cement was replaced by high early strength (type III) cement to examine the shape stability of 3D printed layers. Type III cement is available in white or gray color. Lehigh White Type III cement was used in this research. Type III cement accelerates the rate of hydration so that the viscosity and yield stress of mix cannot maintain for a prolonged time. Which necessitates the optimization of the threshold value of open time before which the concrete has to be printed. To alleviate the issue mentioned above instantaneous mixing procedure might be adopted. After approximately 10 minutes of printing, it required higher pumping force to print the concrete so different ratios of Type III and Type I cement were examined. The optimum ratio of 0.38:0.62 gave the sufficient buildability with optimum pumping force.

g) Mix 7 (Optimization of fiber volume percentage)

1% of PE fiber (Figure 3.1) by volume made the mix clumping of fibers in the mixer. To avoid the fiber clumping and better dispersion of fiber throughout the mix, different percentage of fiber were used in the mix and examined their effect. Fiber volume

fraction of more than 0.75 effects the fresh properties of concrete clumping the fiber in mixer during the mixing creating non homogeneous mix. Although fiber volume fraction less than 0.6 does not have any adverse effect on fresh properties of concrete mix, it have an inimical effect on the hardened mechanical properties of 3D printed structures.

Figure 3.1 Ultra High Molecular Weight (UHMW) Polyethylene fiber

Three 3D printed beams with 0.60% fiber volume fraction were tested following ASTM C78/C78M – 21 Standard Test Method for Flexural Strength of Concrete (Using Simple Beam with Third-Point Loading) [15]. They show formation of only few cracks (less than 3) on the tension side of the beams and sudden drop in load carrying capacity of beams. The fiber volume fraction was increased to 0.75% by volume and tested three in plane beams and three out of plane beams (Section 3.1.6.2. Beams with 0.75% fiber volume fractions showed sufficient ductility with formation of multiple cracks (Section 3.1.6.2). Figures 3.2 and 3.3 shows the 3D printed samples developed at UTA.

Figure 3.2 3D Printed Sample

Figure 3.3 3D Printed Sample (wall)

3.1.2 Mixing Procedure

Figure 3.4 BakeMax Planetary Mixer

The high-performance printing concrete is mixed using high energy/shear capacity BakeMax planetary mixer (Figure 3.4) having volume of 40qt (37.85L). This mixer have rotating blade which scarps all the materials attached to the wall and bottom of the mixer and produces homogeneous mix. All the dry materials expect superplasticizer are premixed for five minutes to attain the consistent distribution of dry materials. HRWR is added to the mix and continued mixing it for two more minutes. Then water is added slowly and continuously for a minute to the mix while mixing. After the turnover is obtained in 6-7 minutes, fibers have added to the mix and mixing is continued to 10 to 12 minutes with the mixing speed of 127 RPM to get consistent mix.

3.1.3 Fresh Mix Properties

3.1.3.1 Turnover Time

This mix contains a high amount of cementitious materials, high powder content as well as low water to cement ratio, which needs more energy input and high shear capacity of a mixer than conventional concrete. Low energy input mixer needs more turnover time, surging the temperature of the mix which hinders the 3D Printing process. Due to the low water dosage and high powder content, partially wetted clods are formed with high viscosity. This is because the water capillary force between dry parti-cles creates a bonding force (that is, viscosity) between particles [10]. High energy shear mixer is required to break those lumps and for proper water distribution throughout the mix. Unbroken lumps hoard water and superplasticizer depriving other particles to involve in the mixing and share the moisture [20]. The mixer (BakeMax mixer) used in this research is capable of breaking those lumps formed and able to shear the mix homogeneously. With the mixing speed of 1 (127 RPM), it was observed that the turnover time is approximately 6.5 minutes.

3.1.3.2 Flowability

The workability of freshly mixed UHP-FRC was determined by flow test accordance with ASTM C1437 ‘Standard Test Method for Flow of Hydraulic Cement Mortar’ [14]. After mixing the UHP-FRC, the freshly prepared mix should be place on the truncated cone as shown in figure below. Fill the cone and rotate the handle attached to the base plate so that it gives an impact on the base for 25 times. The spread cone should be lifted without shaking so that the mix get spread over the plate. After 2 mins, the diameter of the flow should be measured in two mutually orthogonal directions (Figure 3.5) and average

diameter of flow should be taken as the spread value of UHP-FRC. The developed 3DP UHP-FRC mix have average spread value of 100 mm.

Figure 3.5 Flow Measurement of 3D Printed Mix

3.1.3.3 Temperature

AM-UHP-FRC contains type III cement along with a lot of cementitious materials. It takes around 6.5 minutes to become a liquid paste after addition of water. Heat of hydration was observed after 25 mins of powder form changed to liquid state. For this AM-UHP-FRC maximum temperature of the mix have been 80.9^{o}F and has been shown in Figure 3.6. The mix starts to become stiff and it makes difficult to printing process. It depicts the need of continuous mixing and printing machine at the same time. Replacement of one fourth of water by ice prolongs dormant period of cement hydration and reduces the early surge in temperature due to hydration that gives the longer printing time with the same mix.

Figure 3.6 Recorded Temperature of Mix

3.1.3.4 Buildability of Mix

Buildability, some researchers refer to as shape stability, is a critical property of 3D Printable concrete mix. Which is the ability to resist the deformation of the printed layer on its self-weight, the weight of the deposited layer above it, and the pressure due to extrusion during the printing process. The latter two parameters may lead to undesirable deformation of 3D printed layers. The Buildability of the mix depends on the material rheology and open time between the successive layer depositions. Although the longer time is favorable for shape stability, many researches indicate that a longer interlayer deposition gap leads to lower bond strength degrading the mechanical performance of 3D printed structures or elements. Which amplifies the importance of reducing the time gap between

the successive layer depositions. Ideally, the time gap should be zero, which is possible only if the deposited layer beneath it has sufficient stiffness to poses high shape stability.

Kazemian et al., 2017 [19] proposed two different methods namely 'layer settlement test method' and 'cylinder stability method' to observe the buildability and shape stability of 3D printed concrete specimens. Comparing the aforementioned methods, the layer settlement test method is a realistic indicator of mixture performance in layer-based 3D printing of concrete, however, cylinder stability test eliminates the need to print concrete layers, easy, convenient and saves time during the mix design phase and can be used for comparing the shape stability of different mixes, as well as to study the influence of the addition of new materials or any new admixtures. So this research have used both of the methods to examine the buildability of the developed mix.

3.1.4 Determination of Buildability of Mix

3.1.4.1 Layer Settlement Method

In the layer settlement method, two concrete layers should be printed on top of each other with a specific time gap as shown in Figures 3.7-3.9. A measuring scale or tape should be placed in front of printed layers. The photos should be taken before and after the 2^{nd} layer deposition. Those photos should be analyzed with the aid of computer software. This research uses the same principle as the layer settlement method. 5 layers (approx. thickness $\frac{3}{8}$ inches) were printed with the manual printer with a time gap of 4 mins in each layer and recorded the thickness of individual layer observed with vigilant eyes. No visible deformation of the bottom layer was observed also not statically measurable deformation

was recorded. This signifies the developed AM-UHP-FRC mix has good shape stability and buildability.

Figure 3.7 Double Layers (3D Printed UHP-FRC)

Figure 3.8 3 Layers (3D Printed UHP-FRC)

Figure 3.9 Multi Layers

3.1.4.2 Cylinder Stability Method

The cylinder stability test (Kazemian et al., 2017) [19] is based on the application of a certain load (4.77 kpa,0.688 psi stress) from the top on the freshly prepared cylindrical specimen of a certain height (80 mm, 3.15 inches) with two layers and analyzed the resulting deformation. Similar type of experiments have used by other researchers Perrot et al [21]. 40 mm (1.5 inches) of concrete was powered into a cylinder having open base resting on some smooth surface. The concrete was consolidated with the help of tamping rod 15 times evenly around the surface. Same procedure was repeated for the second layer as well and the excess concrete was wiped out. The cylinder was gently taken out and recorded the possible change in height due to self-weight of concrete as shown in Figure 3.10. Then the load equivalent to 4.77 kpa (0.688 psi stress) was applied and resulting

deformation of the freshly prepared cylinder was measured in terms of difference in height of cylinder as shown in Figure 3.11. The following Table 3.2 gives the result of this experiment as well as compares the deformations results with (Kazemian et al., 2017).

Table 3.2 Cylinder Stability Test Results

Mixtures	Test 1 (mm)	Test 2 (mm)	Test 3 (mm)	Average reading	Remarks
AM-UHP-FRC	23	18	20	20.3 mm (0.80 in)	Studied Mix
PPM	41	37	38	38.7 mm (1.52 in)	Kazemian et al., 2017
SFPM	15	15	14	14.7 mm (0.58 in)	
FRPM	34	29	31	31.3 mm (1.23 in)	
NCPM	12	15	11	12.7 mm (0.50 in)	

**Values were measured in mm and converted to inches.*

Figure 3.10 Deformation before Application of Load

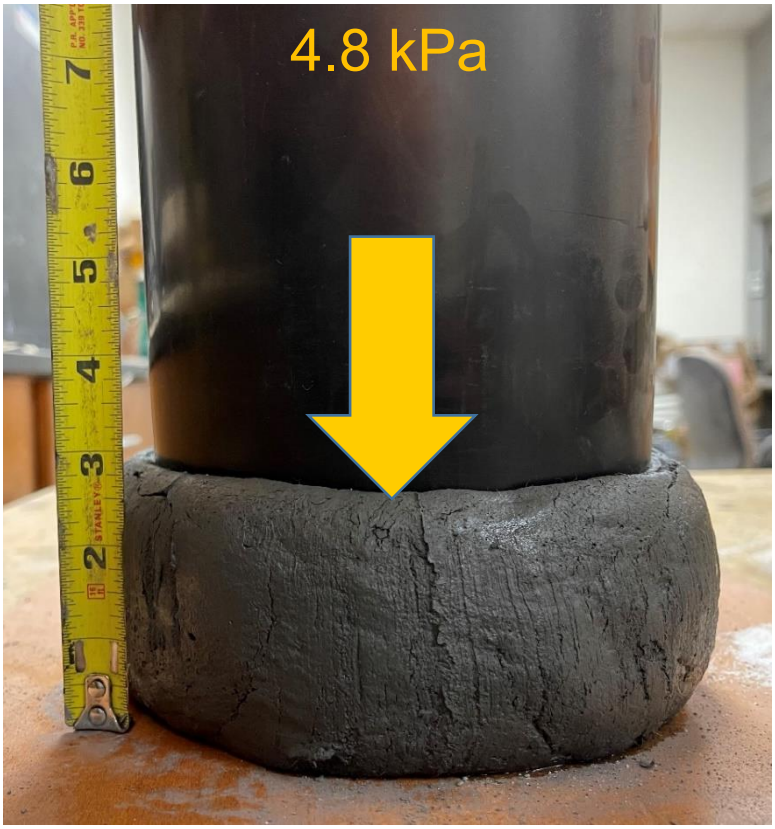

Figure 3.11 Deformation after Application of Load

3.1.5 Determination of Yield Stress of Developed 3D Printable Mix

Proctometer has been used to determine the yield stress of the developed mix. Proctometer is an instrument where a needle is mounted on a spring, which displays the force applied when the needle is pushed into the sample. The proctor has a load-bearing surface see figure. When the needle is pushed to the concrete and taken out, the concrete with yield stress above a minimum value does not close the gap created by the proctor.

The concrete was placed in a 6 in × 6 in × 6 in a test container immediately after the mixing up to below 0.5 in from the top edge of the container to provide space for the collection of excess concrete if any while penetrating the needle. The specimen was stored at room temperature at the lab. A proctor with a tip area of 0.5 in^2 was inserted in the spring-

mounted Proctometer as shown in Figure 3.12 and the tip of the proctor was brought to the bearing surface to make the contact with the concrete surface

Figure 3.12 Proctometer to Determine the Yield Stress

Gradually and uniformly the vertical downward force was applied until the needle penetrates the concrete to a depth of 1 inch and the maximum force displaced by the gauge was recorded. To maintain consistency in the testing the time required for each time penetration was 10 seconds. The yield stress was calculated by the dividing recorded force by bearing area which is 0.5 in^2 and has plotted in Figure 3.14. In the subsequent penetration test to avoid the areas where concrete has been disturbed by the previous test the clear distance between needle, the impression was at least 0.5 in as shown in the Figure 3.13. As per ASTM C403 [48], Standard Test Method for Time of Setting of Concrete

Mixtures by Penetration Resistance the clear distance between any needle impression and the side of the container shall be at least 1 in. [25 mm], but not more than 2 in [50 mm].

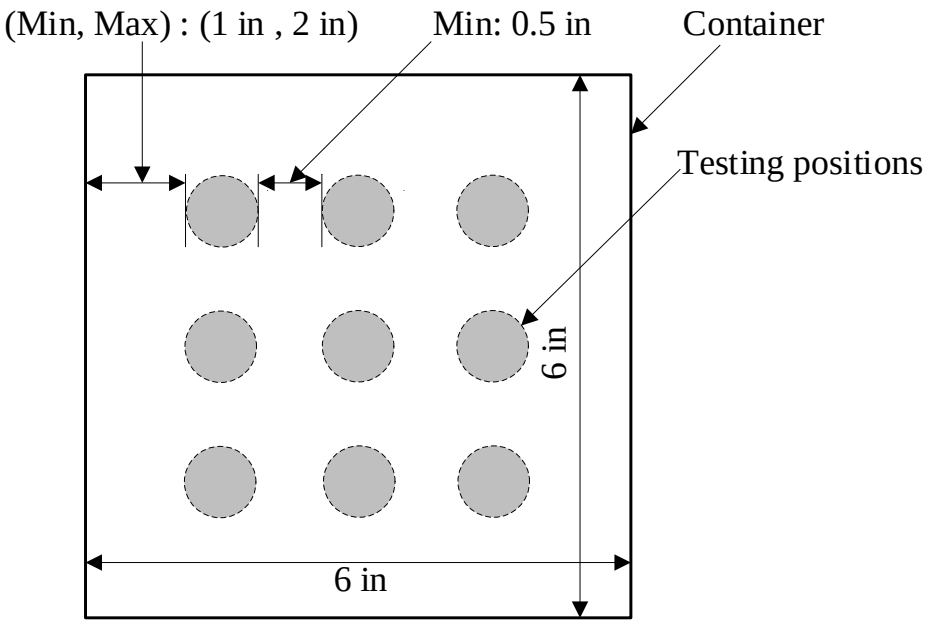

Figure 3.13 Proctor Test with Measuring Positions

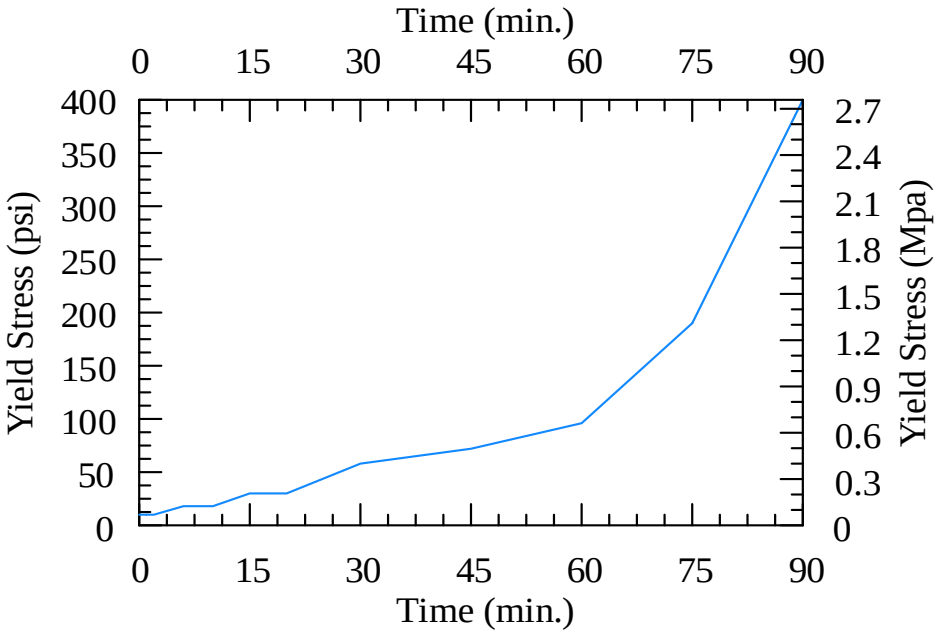

Figure 3.14 Yield Stress vs Time (3D Printing Mix)

3.1.6 Hardened AM-UHP-FRC Properties

3.1.6.1 Compressive Strength

Table 3.3 Compressive Strength of Developed Mix

Sample Age	Compressive Strength (ksi)
1	9.31
3	12.51
7	13.9
14	15.25

Values are based on the average compressive strength of 3 cubes

The uniaxial compressive strength test was carried out on a 400 kips capacity servo-hydraulic testing machine. The compressive strength on various days have been summarized in the table 3.3. 2 inch (50 mm) brass molds have been used to ensure sufficient smoothness and parallel loading surfaces. A displacement control method with rate of loading 0.04 in/min have been used to test the specimens.

3.1.6.2 Out of Plane Flexural Strength

Sample preparation and testing

Three 3D printed beams each of length more than 21 inches, and width of 4 inches, and 4 layers with an interlayer thickness of approximate $\frac{5}{8}$ inches as shown in Figure 3.15 were printed using the manual printer. After printing the beams to maintain the humidity, they were stored in a curing room with 76^{o}F temperature for 28 days until the time of testing. The beams were cut each of length 21 inches on testing day prior to testing to follow the ASTM C78/C78M – 21 Standard Test Method for Flexural Strength of Concrete (Using Simple Beam with Third-Point Loading) [15]. The measurements were taken and stored in

data acquisition system. The load were obtained from load shell of machine and displacement were obtained from LVDT's placed at mid span on either side of the beam. Displacement control loading was applied from servo hydraulic 55 kips machine with a constant loading rate of 0.04 in/min.

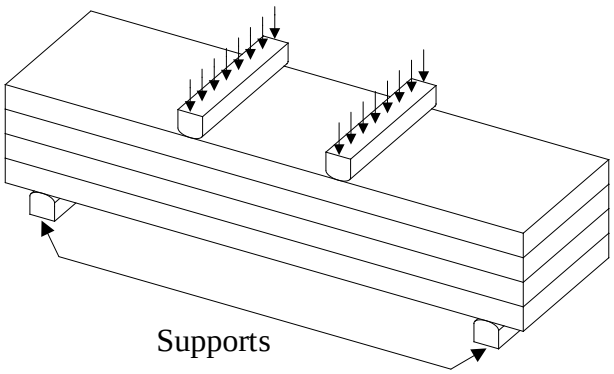

Figure 3.15 Flexural Testing Position of Beam (out of plane)

Results:

Figures 3.16 and 3.17 gives the load deformation curve of 3D printed specimens. The onset of cracks and its development, their propagation and crack width were carefully monitored visually. The following curve illustrates the performance of the 3D printed beam in out of plane flexure. The load was constantly increasing from zero to nearly 1.5 kips and cracks formation occurs. Multiple cracks occurs on the tension side of beam with good ductility. Since the beam have multiple layers, crack occurs on the lowest layer and it propagates upwards. During the crack extension, the upper layer does not have stress concentration so load increases for a while and again drops as depicted by the figure below. The developed mix shows very good ductility and high modulus of elasticity.

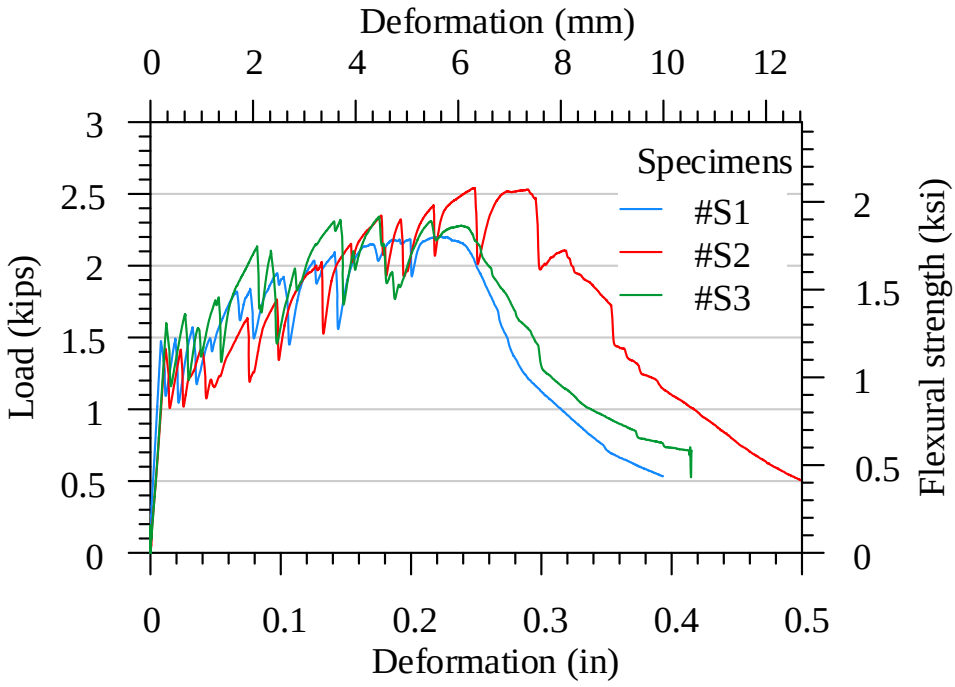

Figure 3.16 Load vs Deformation Curve up to 0.5in Deflection

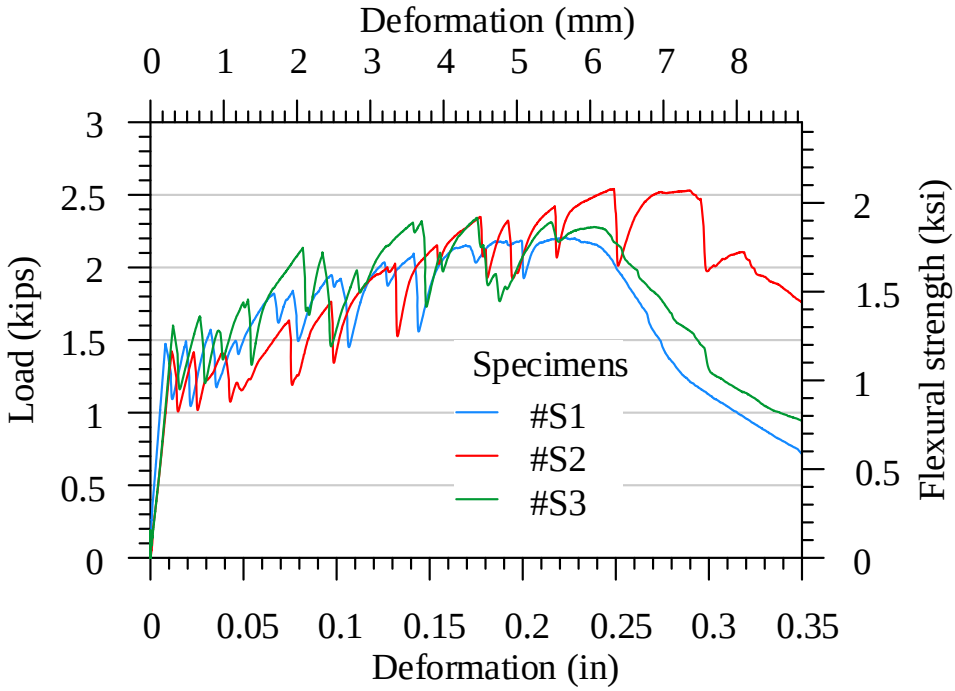

Figure 3.17 Load vs Deformation Curve up to 0.35 in Deflection

3.1.6.3 In Plane Flexural Strength

Sample preparation and testing

Three 3D printed beams each of length more than 21 inches, and width of 2.5 inches, and 6 layers with an interlayer thickness of approximate $\frac{2}{3}$ inches were printed using the manual printer. The specimen preparation, load testing set up and testing method were followed procedure explained in Section 3.7.2. The samples were cast and they were turned to 90 degree as shown in Figure 3.18 to maintain the in plane loading direction as shown in figure.

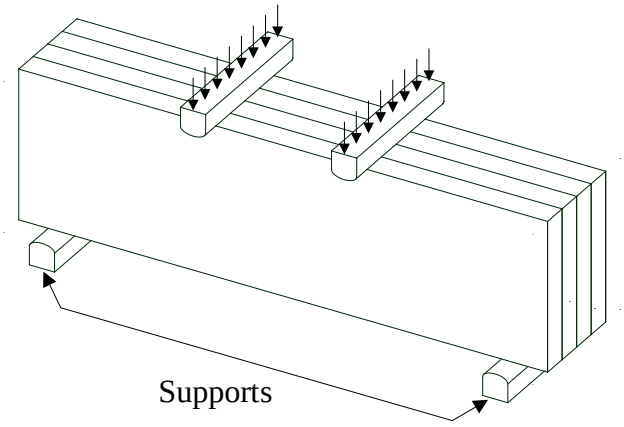

Figure 3.18 Flexural Testing Position of Beam (in- plane)

Results

The onset of cracks and its development, their extension and crack width were carefully monitored visually. The following curve illustrates the performance of the 3D printed beam in in-plane flexure. Multiple cracks were observed on tension side of beam and beams have shown very good ductility with high modulus of elasticity. Observed multiple cracks can also be explained from the figure below (Figures 3.19 and 3.20).

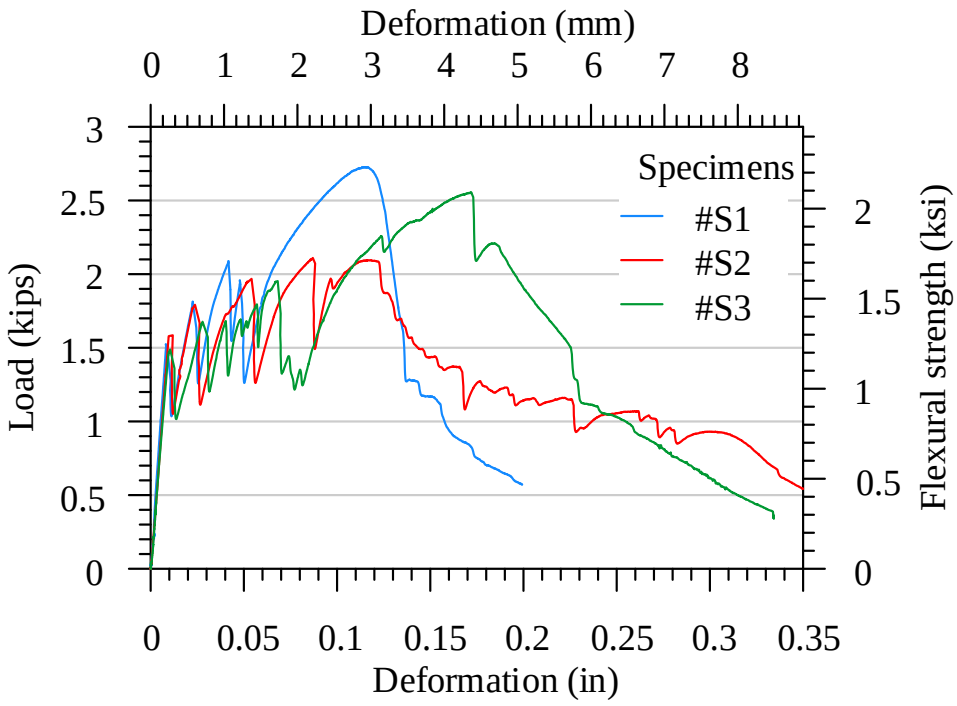

Figure 3.19 Load vs Deformation Curve Up to 0.35 in. Deflection

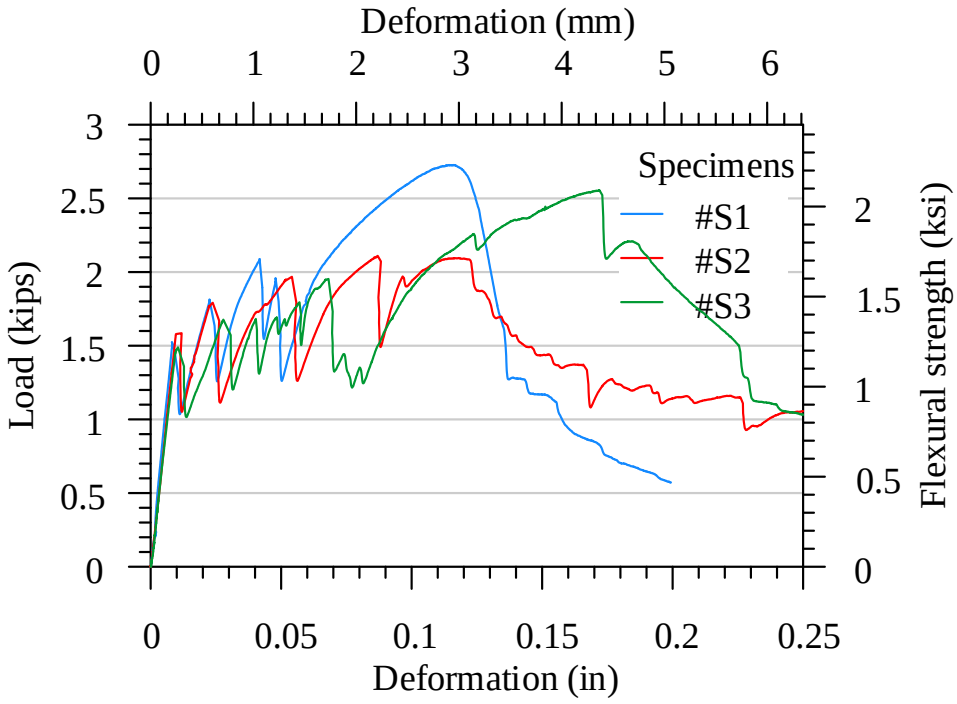

Figure 3.20 Load vs Deformation Curve up to 0.25 in. Deflection

Figure 3.21 gives the comparison of flexural performance between in-plane bending and out of plane bending of 3D printed specimens.

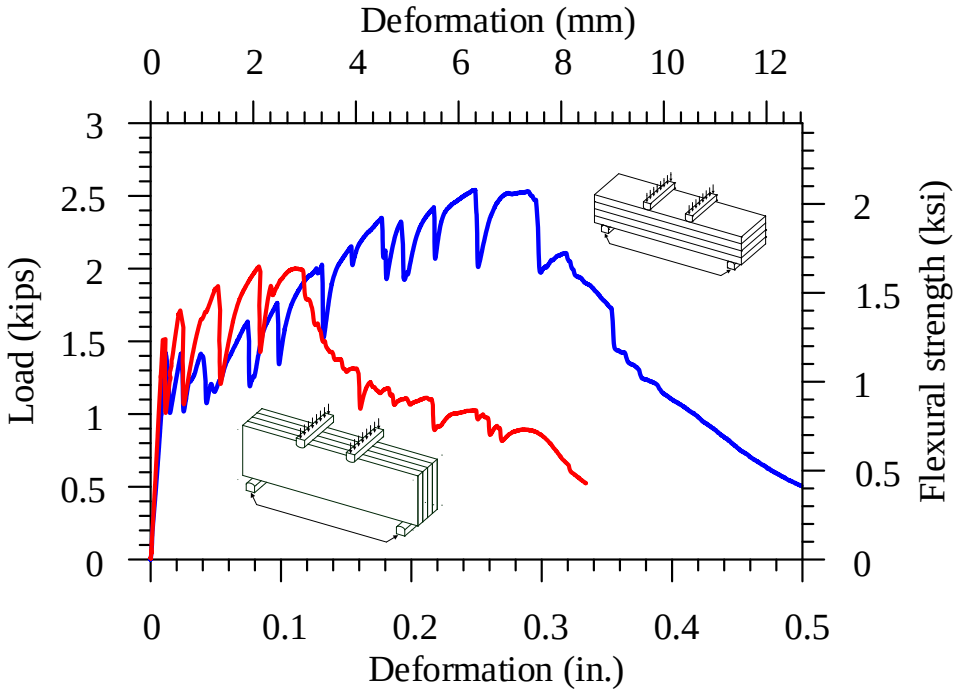

Figure 3.21 Comparison between Out of Plane Bending and In-plane bending of 3D Printed Specimens

3.1.6.4 AM-UHP-FRC Mix Normal Casting

Sample preparation and testing

For the comparison purpose with the 3D printed beams explained in Section 3.7. Three normal beam with the same dimensions (length 21 inches, width 4 inches and depth 2.5 inches) were cast using the same mix but without 3D printing. The curing procedure, test set up, and testing methods were same as those explained in the Section 3.7.2.

Results

The beam shows sudden drop in load due to formation of only one crack that propagate too quickly as shown in Figure 3.22. The issue with this beam is thought to be related to the

concentration of stress in only one crack which propagates quickly upwards. 3D printed beams perform better performance than normally cast beams of same materials. This is due to preferential fiber alignment parallel to the direction of extrusion during the printing process.

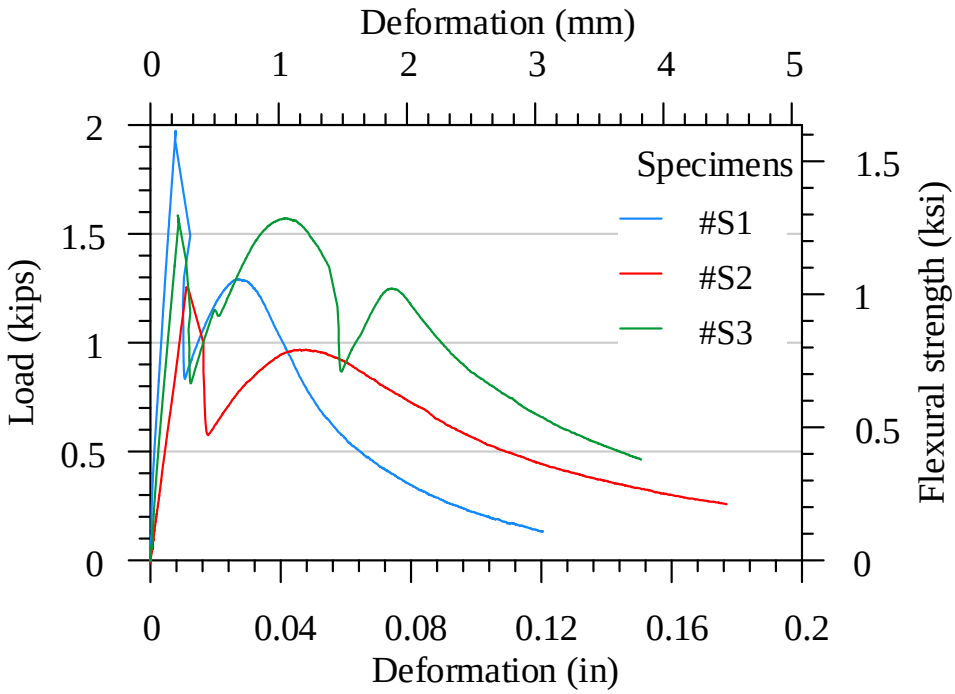

Figure 3.22 Load vs Deformation Curve (Without 3D Printing)

3.1.6.5 Comparison Between 3D Printed (AM-UHP-FRC Mix) Beam Vs Normally Cast Beam

Sample preparation and testing

A 3D printed beam normal concrete beam were prepared and tested in 14 days for the observation of performance of AM-UHP-FRC and normal concrete in flexure. The specimen preparation, load testing set up and testing method were followed procedure explained in Section 3.7.2.

Figure 3.23 3rd Point Bending Testing of Conventional Plain Concrete Beam

Figure 3.24 3rd Point Bending Testing of 3D Printed Beam

Results

The following Figure 3.25 illustrates the comparison between the 3D printed beam and normal beam in flexural testing following ASTM C78/C78M – 21 Standard Test Method for Flexural Strength of Concrete (Using Simple Beam with Third-Point Loading) [15]. 3D printed beam shows sufficient ductility, multiple cracks, and high energy dissipation. However, normally cast normal beam shows the brittle failure.

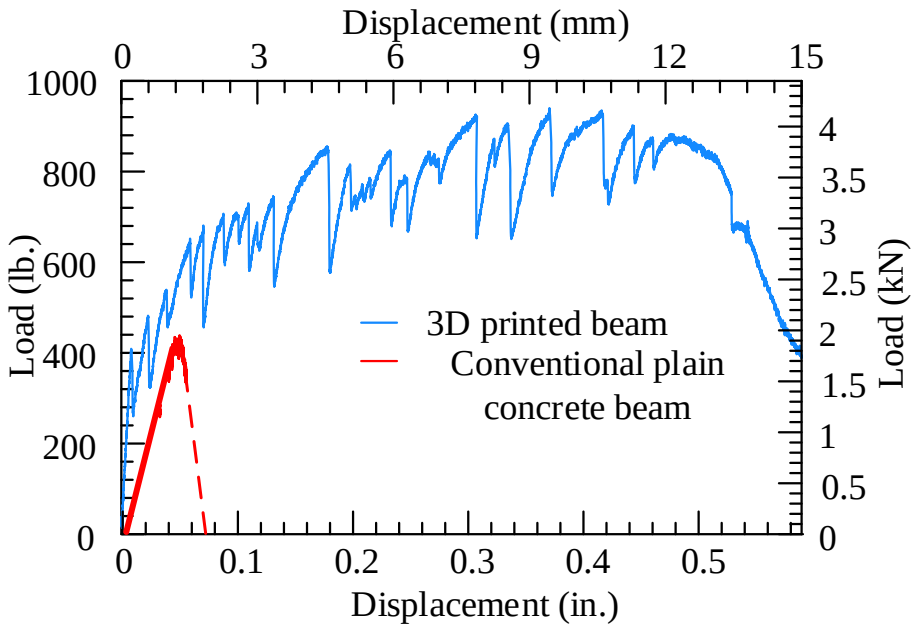

Figure 3.25 Load vs Displacement Curve (3D Printed Beam and Conventional Plain Concrete Beam)

3.1.6.6 Interlayer Bonding

Interlayer bonding is one of the major criteria of 3D printing of concrete. The lack of cohesion between the two interlayers of 3D-printed specimens is one of the bottlenecks of additive manufacturing. Lack of interlayer bonding limits the scope of 3D printing on large scale. Interlayer bonding on 3D printing depends on the roughness of the surface, successive time of deposition of a new layer, types of fiber used, and material rheology.

Successive time of deposition of a new layer can be programmed and controlled during the printing process. The roughness of surface and material rheology depends on the material used in the AM-UHP-FRC mix. In some studies, Hosseini et al., (2019) [16] used a new polymer consisting of black carbon and sulfur to glue the two layers together to ensure sufficient interlayer bonding. Of course, the application of new materials in between every layer delays the printing process and burdens the extra cost which undermines the principle of 3D printing. This research uses a special mix that does not require exotic materials between the successive layers for sufficient bonding.

Sample preparation and observation

Sample 1:

A square prism of size 8 inches width, 8 inches length, and 6 inches depth was prepared and rectangular prism was printed with the manual printer with ten layers of approx. $\frac{3}{5}$ inches depth. The prism was stored in the room temperature in the lab. After 28 days of printing, the prism was cut using a rotary cutting tool with diamond bits. The visual observation of cored sample (Figure 3.27) does not show any traces of layers that depict full bonding between two successive layers.

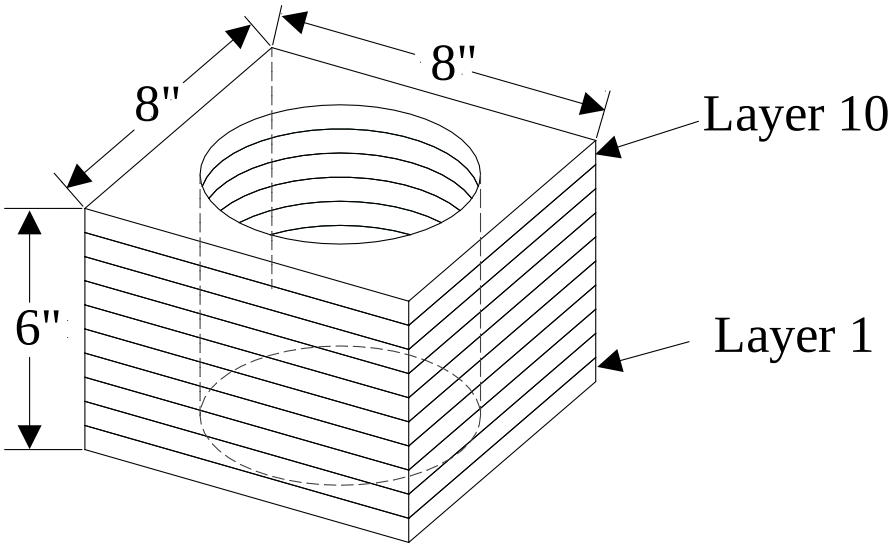

Figure 3.26 Schematic Diagram of Cored Sample

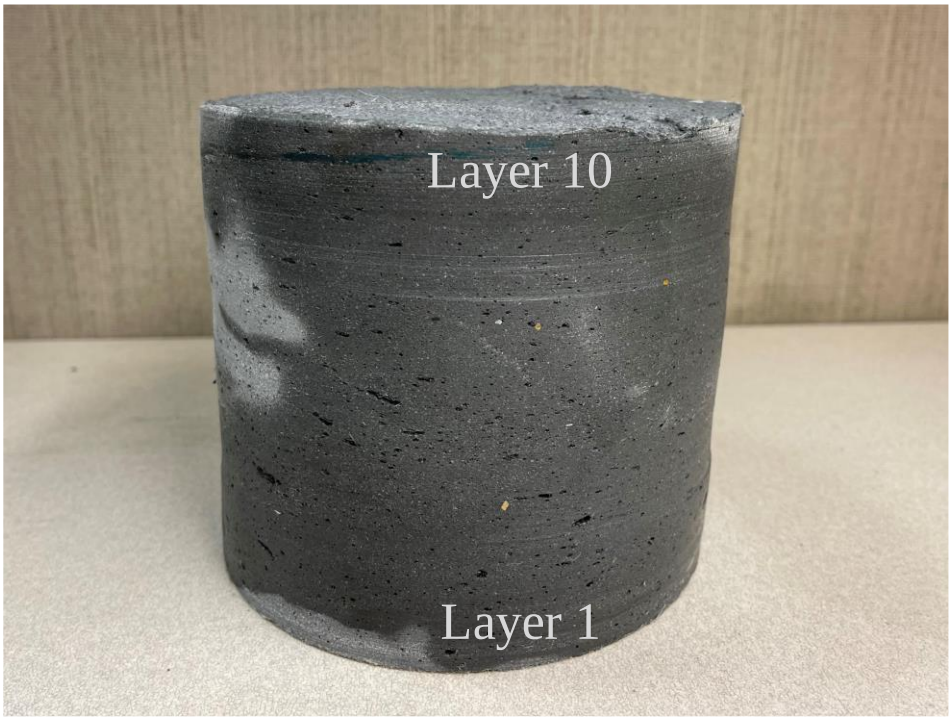

Figure 3.27 Cored Sample From 3D Printed Slab

Sample 2:

Six 3D printed beams were tested for out of plane loading and three 3D printed beams were tested for in-plane loading (refer to the Section 3.7) following ASTM C78/C78M – 21 Standard Test Method for Flexural Strength of Concrete (Using Simple Beam with Third-Point Loading) [15]. There was no any observation of splitting of layers during loading which proves sufficient bonding between the layers to prevent interfacial shear failure. In addition, 3D printed specimen was cut as shown in Figure 3.28, but no any traces of layers were observed.

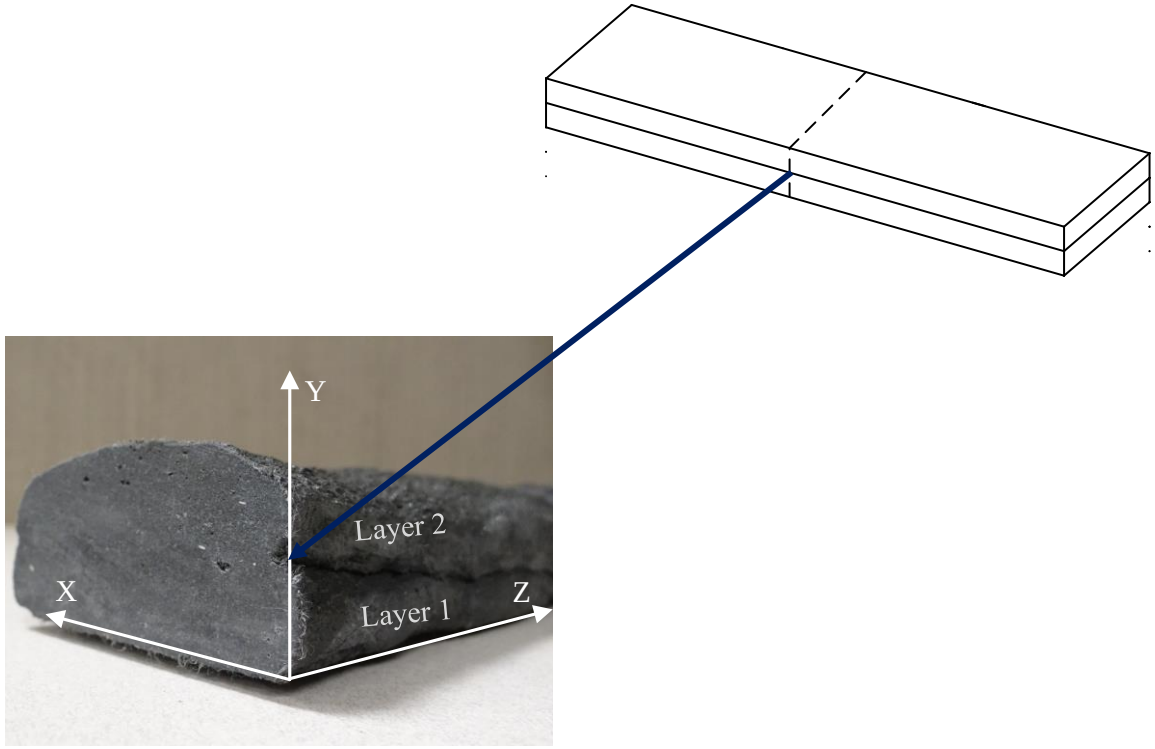

Figure 3.28 Seamless Interlayer

3.1.7 3D Printing on Slopes

3D printing of concrete can be used in slopes in many cases like to repair potholes in pavements on steeply roads. During the printing process, the concrete is still in its plastic

state, where particles movement may occur and objects the shape stability of 3D printed members. In inclined members, two downward forces (gravity on the whole member and gravity on the particles which is still in its plastic stage) involves that tries to drag the specimen down. This research studies 3 different slopes 10 degree, 20 degree and 30 degree slope as shown in Figure 3.29, and found no particles movement. However, no particle movement in 30 degree slope, there is high chances of either movement of single layer from adjacent layer or movement of whole block from the base.

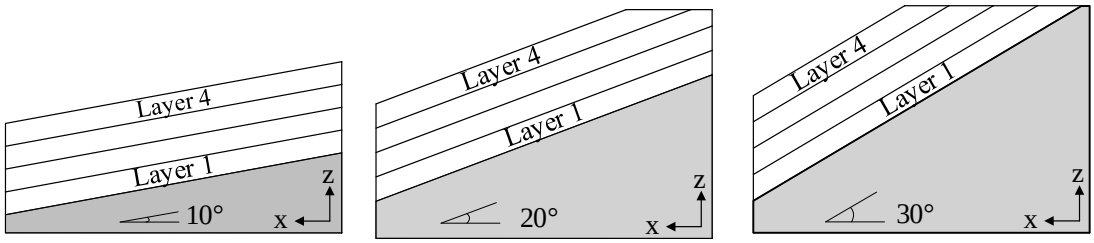

Figure 3.29 3D Printing on Slopes

3.1.8 Limitations of the Study

Mix design also depends on several printer parameters such nozzle shape and dimension, extrusion speed, printing speed, and type of printer. Such parameters were not studied in this research.

3.2 Development of Ultra-High-Performance Slurry Infiltrated Fiber-Reinforced Concrete (UHP-SIFCON)

3.2.1 Types of Fibers Used in Experimental Program

The following two hooked fibers have been considered for the initial experiment purpose of SIFCON and later on only fiber B was used throughout and compared with UHP-FRC having micro straight fiber. Figures 3.30 and 3.31 gives the information about the fibers used in this research program.

Figure 3.30 Different Fibers Used in Experimental Study

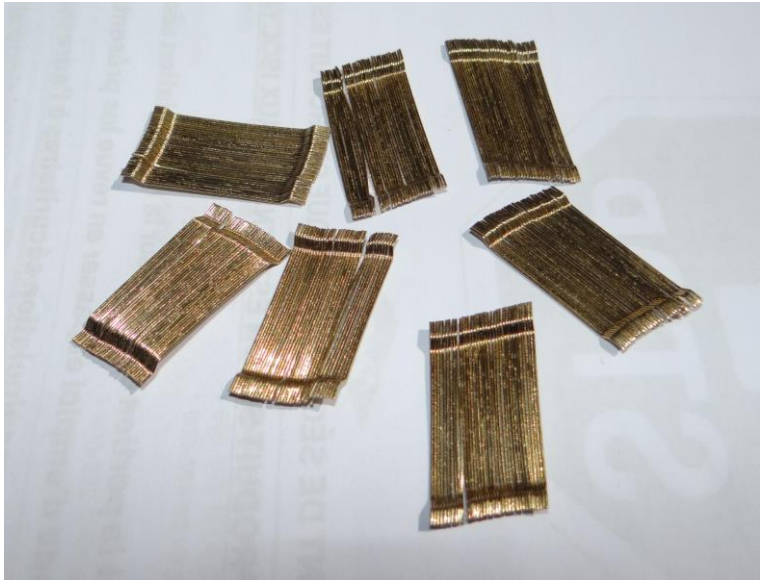

Figure 3.31 Fiber Type B (3D fiber)

Table 3.4 Fiber Types and its Properties Used In Experimental Study

Fiber	Diameter (mm)	length (mm)	Aspect Ratio	Tensile Strength (MPa)	Fiber Volume Fraction (V_f)	Reinforcing index (V_f l/d)
1D Hooked fiber (A)	0.8	40	49.6		(10-12)%	496
3D Hooked fiber (B)	0.38	30	80	3,070	7.5% (approx.)	600
Micro straight fiber (C)	0.175	12.5	71.4	2,000	3%	214.8

***Length and diameter of fibers are the average of 5 random samples taken.*

3.2.2 Determination of Maximum Fiber Volume Fraction

The fiber volume fraction depends on the fiber type and vibration energy input. The smaller or shorter the fiber higher the fiber volume fraction can achieve than longer fiber. The larger the diameter of the fiber it is easier to get a higher fiber volume fraction but it reduces the total number of fiber, which reduces the number of fibers bridging the crack. So the larger fiber diameter is also not desirable. A higher volume fraction can be achieved with increased vibration energy input. If the fiber density is too high, UHPC paste cannot infiltrate the fiber bed, at the same time if the fiber density is too less, the fibers will settle down during the UHPC paste pouring. The optimum fiber volume fraction should be determined and which varies with fiber size and type.

Naaman, et al, 1987; Homrich and Naaman 1987; Naaman et al.,, 1991 used 30 mm long and 0.5 mm diameter (Bekaert ZL 30/50 fibers) fibers and get the fiber volume fraction of 10% to 12%. And the same team reported the fiber volume fraction was limited to 5% to 6% for the same 50 mm long fiber with the same diameter of 0.5 mm (Bekaert ZL 50/50

fibers). It demonstrates the increasing the length of the fiber, decreases the maximum attainable fiber volume fraction.

In this research for our initial experiments, fiber type A with fiber volume fraction 10% to 12% have been chosen. For a higher fiber volume fraction of more than 12%, it is difficult to infiltrate the UHPC mix. For a 10% volume fraction of fiber A, UHPC paste easily infiltrates up to the bottom of the mold. In the second phase of the experiment, fiber type B, Bekaert 3D 80/30 BGP fiber has been used. It means the fiber diameter of 0.38 mm, 30 mm length, an aspect ratio of 80, and bright glued fiber. The fibers were glued together and supplied in the bundles (refer to figure 3.4). The fibers had to put in the water and apply external force (using the mixer). In this entire process, many fibers were entangled already which led to the lower fiber volume fraction. Because of the fiber entanglement, small diameter, and short length of the fiber type B, the maximum fiber volume fraction that can be achieved is limited to 7.5%.

Homrich and Naaman (1987) observed that the SIFCON with similar matrices and same reinforcing index have similar performance on the tension test. This suggests different types of fibers with different volume fractions can perform similarly. Thus reinforcing index is an important factor affecting the performance of SIFCON. Also from the Lankard 1984 equation, it is expected to have higher ultimate post cracking strength 3D hooked fiber.

3.2.3 Process of SIFCON Formation

Empty molds were cleaned and weighed on a weighing scale. Those molds were kept over a small vibrating table and gentle vibration was turned on. Then the fibers were placed

from the top slowly to allowing the fibers to settle and maintain sufficient packing to achieve the higher volume fraction. Fiber placement can be done by hand or commercially available fiber dispensing unit. The gentle vibration also helps to ensure uniform fiber distribution throughout the mold. In general, the fibers are randomly distributed to the horizontal direction. But at near the edge of the mold, some of the fibers are oriented vertically. UHPC was mixed in a mixer until sufficient flowability was achieved. Attention should be given to make sure that there was not any lumps formation during mixing. The formation of lumps block the infiltration process and make the infiltration process delayed and difficult. After the paste becomes ready, it was added from the top of the molds. The paste can be added to the fiber bed from the bottom using pressure grouting. During the infiltration process, molds were placed on the vibrating table with light vibration turned on. The specimens were unmolded after 24 hours and submerged in water. The specimens were taken out from water before 48 hours of testing and stored in the laboratory environment. Figures 32-36 depicts the process of SIFCON formation.

Figure 3.32 Dog Bone shaped specimen (showing side reinforccement)

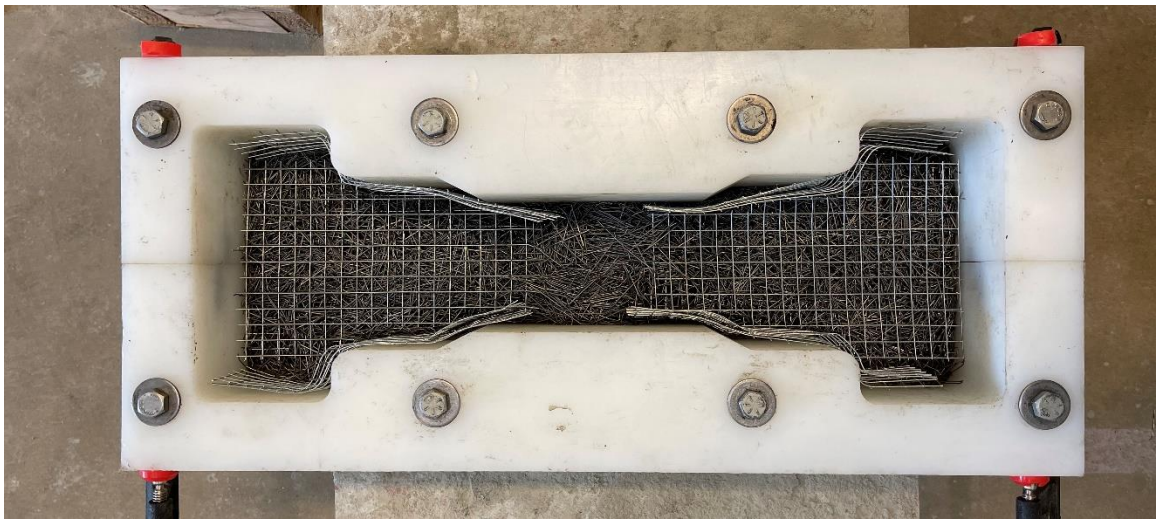

Figure 3.33 Dog Bone Shaped Specimen (showing reinforcing mesh)

Figure 3.34 Dog Bone Shaped Specimen (filled with steel fibers, fiber type A)

To make sure the failure happens within the central portion, the desired area is reinforced with reinforcing mesh as shown in Figures 3.30 and 3.31. 5 layers of mesh in the larger ends and 2 layers of mesh in the side where the cross-section of the specimen changes.

Figure 3.35 Dog Bone Shaped Specimen (filled with steel fibers, fiber type A)

Figure 3.36 Dog Bone Shaped Specimen (filled with steel fibers, infiltration of concrete)

While pouring the UHPC paste in the narrow shaped fiber bed, the UHPC blocks the air coming from the bottom of the fiber bed and the air bubbles inside the concrete forms as

shown in Figure 3.37. Wide shaped specimens does not have this type of problem. Entrapped air bubbles affects the mechanical properties of SIFCON. The vibration during the infiltration process helps to escape the entrapped air inside the concrete.

Figure 3.37 Formation of Air Voids during the Infiltration of UHPC paste

3.2.4 Study on the UHPC Paste for SIFCON

UHPC paste is the backbone of the SIFCON matrix. The compressive strength, elastic modulus and tensile strength affects the final properties of the SIFCON matrix. The tensile and flexural strength of the SIFCON is greatly depends on the fiber pull out from the matrix, higher the compressive strength of the matrix, the higher will be the pull out strength. Also, the voids created after the placement of hooked fibers are filled by the UHPC paste. Therefore, the maximum size of particles plays a crucial role in the infiltration process. In the preliminary study, having the finer particle size, type III cement was proposed to use as a replacement for type I cement. However, because of the high early

heat of hydration, the paste UHPC paste became more viscous and it was difficult to infiltrate the steel fibers. The surface temperature of UHPC paste, measured from an infrared thermometer, was found 76F which could be felt by bare hands. So the type I cement has been used throughout this experimental study. Two types of silica fumes; Norchem Silica Fume and Elkem Silica Fume, were studied in the UHPC paste to examine the flowability of the mix. UHPC with Elkem Silica Fume has been used in this study having more flowable UHPC paste. The Elkem Silica Fume has a relatively lower carbon content compared to Norchem Silica Fume, it makes the mix more flowable, and utilized this property to make UHPC paste which easily infiltrates into steel fiber. The superplasticizer content on the parenting mix was 2.1% by weight of cement and which have been increased to 3.5% by weight of cement to increase the flowability that makes easier infiltration. Superplasticizer dosage and flowability were limited to a certain limit to avoid the segregation of the steel fiber in the conventional fiber reinforced concrete but in SIFCON steel fibers are prepacked to a maximum limit which avoids the possibility of fiber settlement during the infiltration process.

3.2.5 Mechanical Properties of UHP-SIFCON

3.2.5.1 Compressive Stress-Strain Plot (SIFCON and UHP-FRC)

Sample preparation and testing

Three 4 in. diameter and 8 in. height cylinder (Figure 3.38) SIFCON with fiber type A and three 4 in. × 4 in. × 3 in. cuboid (Figures 3.40-3.41) with fiber type B were cast as per the process explained in section 3.2.3. For the initial study cylinders with fiber type A were prepared and tested and later the cuboid with fiber type B was prepared and tested. To maintain the nearly same cross-sectional area as cylinders, cuboid with 4 in. × 4 in. × 3 in. were chosen and tested from the 4 in. × 3 in. side on the top and bottom.

Figure 3.38 Compression Testing Setup

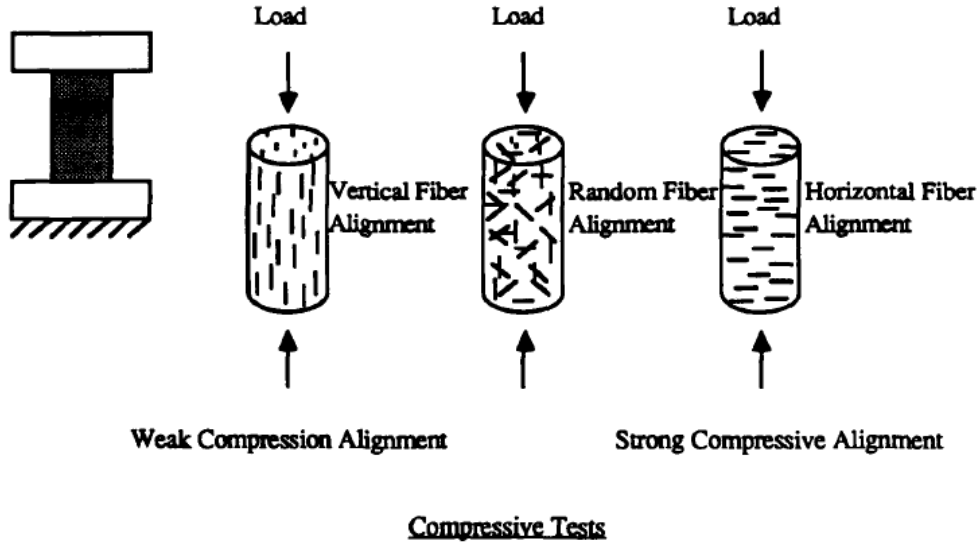

Figure 3.39 Anisotropic Behavior of SIFCON (Naaman et al., 1998)

Figure 3.40 SIFCON Cuboid Mold

The compression testing setup consists of a compression testing machine, load shell, two LVDTs (Linear Variable Differential Transducer), and DAQ (Data Acquisition System). During the testing, the cylinder or cuboid was placed on the top of the load shell and two LVDTs were installed on the two opposite sides to measure the vertical axial deformation. LVDTs and load shell were connected to the DAQ and recorded the load and deformation. The load and deformation values are converted into stress and strain and have plotted.

Figure 3.41 shows the loading direction of compression testing of specimen. Figures 3.42-3.43 shows the inside the SIFCON after cutting the specimen.

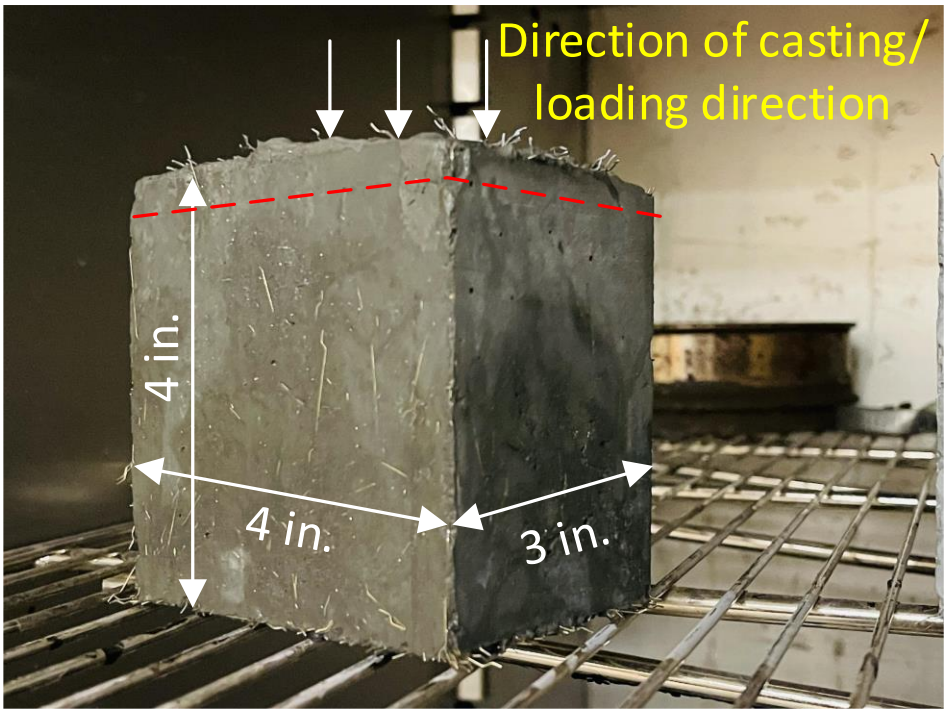

Figure 3.41 SIFCON Cuboid Specimen

Figure 3.42 SIFCON Cylinder After Cutting the Top (fiber type A)

Figure 3.43 SIFCON Cylinder after Cutting the Top (fiber type A)

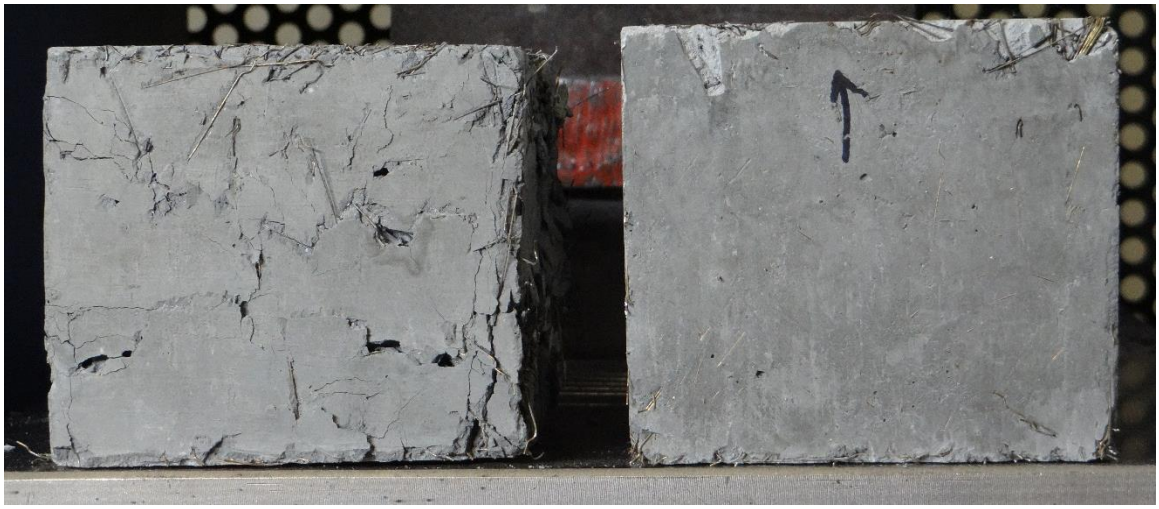

Figure 3.44 SIFCON Cube After and Before the Testing

Results

The following (Figure 3.43) figures is the stress-strain curve of SIFCON. The specimens were demolded at one day and cured in oven at 76 degree centigrade for 7 days. The specimen with fiber type B was cured in water for 7 days after it was cured for 7 days in oven. Figure 3.44 shows the SIFCON cube specimens before and after the testing.

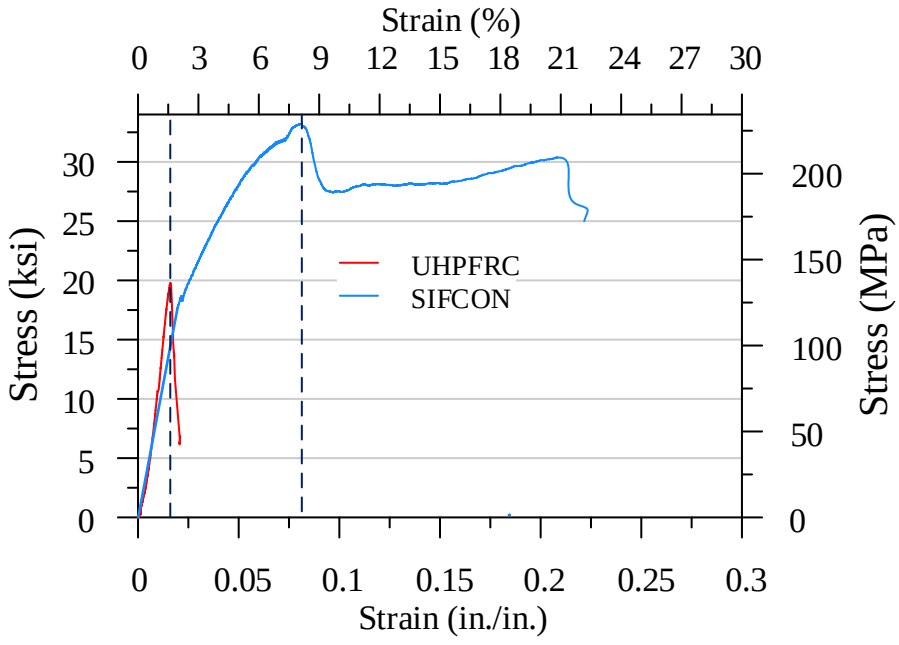

Figure 3.45 Stress Strain Curve (UHP-FRC and SIFCON)

For fiber type A, maximum compressive strength achieved was 22 ksi for corresponding compressive stain of 1.7%. For fiber type B, the maximum compressive strength was recorded as 33.17 ksi for corresponding compressive strain of 8%. UHP-FRC also performed similar to the fiber type A but less compressive strength about 19 ksi. The specimen can exhibit 90% of the peak load for corresponding compressive strain up to 21%. The Bulging-like failure is observed when the compressive strength of matrix is relatively low and shear like failure was observed when the compressive strength is high. It shows that fiber type B is effective for SIFCON application. Although the fiber volume fraction of the specimen with fiber type A (10%) is higher than the fiber volume fraction of specimen with fiber type B (7.5%), the performance of SIFCON with fiber type A surpasses the performance of SIFCON with fiber type A. Early drop in stiffness of the cuboid is due to the presents of micro cracks at the surface of the specimen due to the cutting the top part of the specimen as shown in red line in figure 3.23. The cuboid was cut from the top after 4 days of casting to make sure the top and bottom surface are smooth and perfectly leveled.

Figure 3.46 Typical Shear-Like Failure of SIFCON (fiber type A, 10% Vf)

Figure 3.47 Typical Bulging-Like Failure of SIFCON (fiber type A, 10% Vf)

Figure 3.48 Typical Bulging-Like Failure of SIFCON (10% Vf)

Figure 3.49 Typical Bulging-Like Failure of SIFCON Followed by Shear-Like Failure

(10% V_f)

Figures 3.50-3.52 shows the SIFCON cutting location and inside the SIFCON after cutting at different location. Figure 3.53 shows the SIFCON specimen where infiltration was not sufficient.

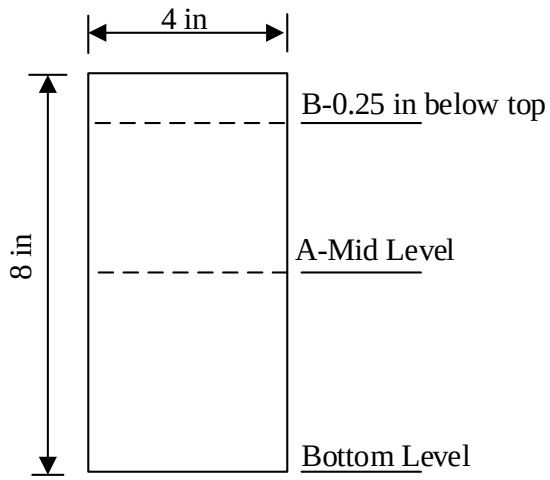

Figure 3.50 Cylinder Cutting at Different Level After Testing

Figure 3.51 Section of Cylinder at Section B in the Figure 3.47

Figure 3.52 Section of Cylinder at Section A in the Figure 3.50

Figure 3.53 SIFCON Cylinder with Hooked-Ends Steel Fibers Half Infiltrated by UHPC Slurry

3.2.5.2 Edge Effect

The fibers are placed in the mold before pouring the concrete. In general, the fibers distribution in the middle section of mold is uniform however the fiber distribution is relatively poor in the edge section of the mold as shown in Figures 3.54-3.55. Poor distribution of fiber is due to the length of the fiber [3], and it makes the lower fiber density near the edge of the specimen. Also, some of the fibers align themselves vertically during placing the fiber and also during pouring the concrete with the application of little vibration. The edge effect tends to reduce the effective cross-sectional area of the tested specimen and ultimately the lower force.

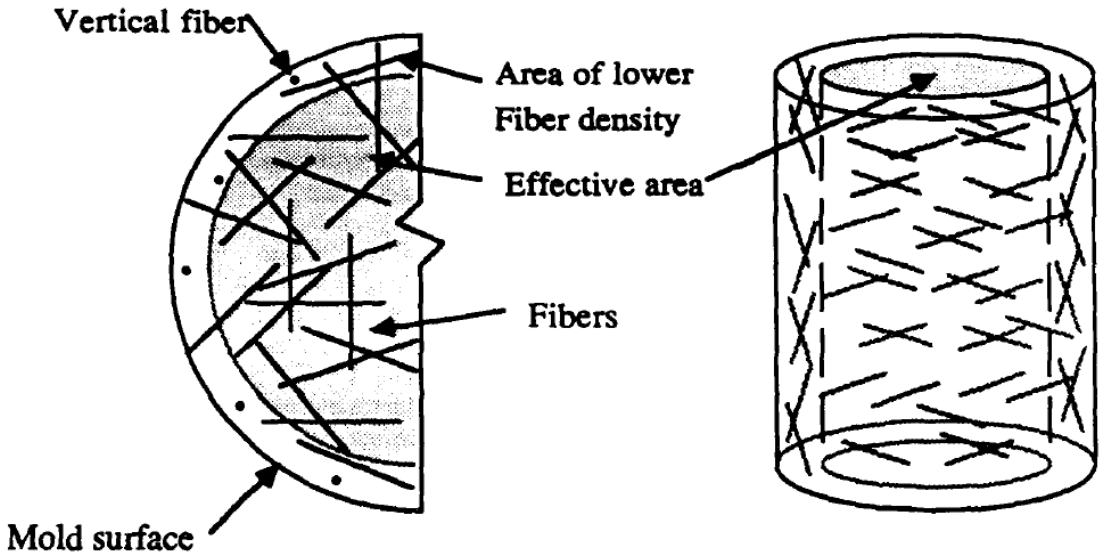

Figure 3.54 Edge Effect in Cylinder (Naaman et al., 1998)

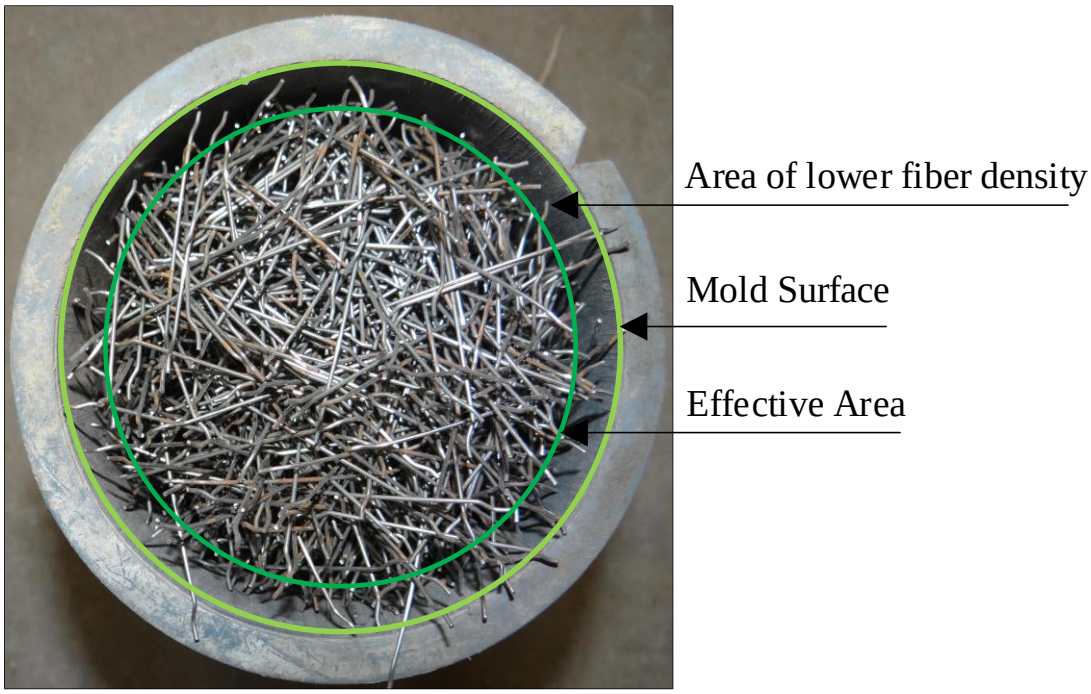

Figure 3.55 Edge Effect in Cylinder

During the uniaxial compression testing of a cylinder, the outermost surface of the cylinder was spalled off leaving the central core of the cylinder to resist the loading applied as shown in Figure 3.56. Similar situation was observed in the case of SIFCON cube specimen as shown in Figure 3.57. Similar behavior was observed in Joseph et al. (1998) [1]. Joseph et al. (1998) observed that cored specimens showed a 30% increase in ultimate strength over the mold cast specimens. A lesser edge effect was observed with a smaller diameter and smaller length of the fiber. Vertically aligned fibers plays less in the compressive capacity as well as ductility. They are not entangled each other acts as separate piece. A similar situation was observed for the SIFCON beam tested in flexure. Lankard 1984 [5] observed the flexural specimens molded as beams have shown 2 to 3 times the flexural capacity than the specimens molded as column. This is due to the preferential fiber orientation.

Figure 3.56 Failure Starting From the Outside Surface (Cylinder)

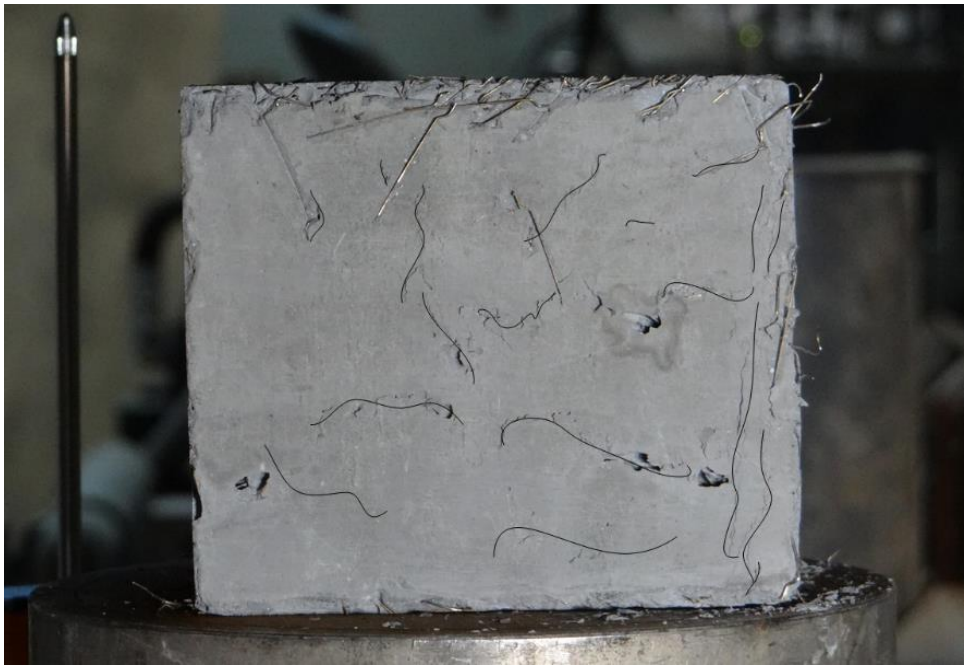

Figure 3.57 Failure Starting From the Outside Surface (Cuboid)

3.2.5.3 Double Punch Testing of SIFCON Specimens

Sample preparation and testing

6 in. diameter and 12 in. height cylinders were filled with the fibers and the resulting fiber bed was infiltrated by the UHPC paste. During the infiltration process, molds were placed on the vibrating table with light vibration turned on. The specimens were unmolded after 24 hours and put in the oven for 6 days at a temperature of 76 F with water placed on side of them to maintain the humidity. The specimens were taken out from the oven before 24 hours of testing, cut them half to 6 in. × 6 in. using the concrete cutting machine and stored in the laboratory environment. The top and bottom of the specimen were smoothened using the sandstone to make sure both the surfaces were perfectly leveled. Figure 3.58 shows the testing setup of double punch test.

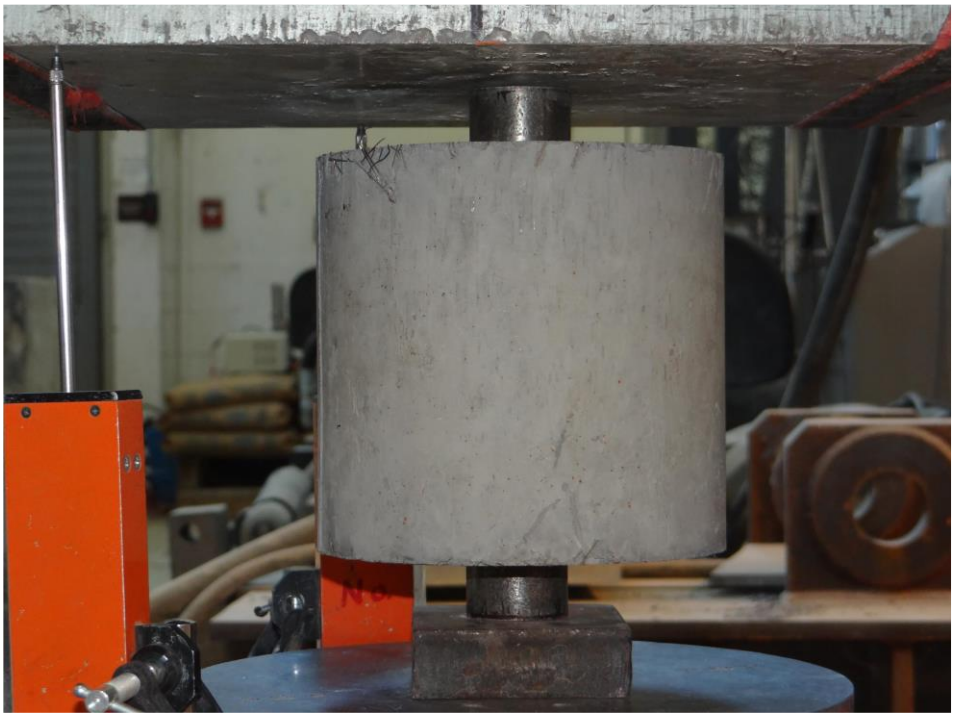

Figure 3.58 DPT Test Set Up

Figure 3.59 Side View of Tested DPT Specimens

Figure 3.60 Top View of Tested DPT Specimens

Three cylinders with 1D fiber (fiber type A) and a cylinder with 3D fiber (fiber type B) were cast. Each of them were cut into halves so that there were three bottom halves specimens for fiber type A, three top halves for fiber type A and a bottom and a top specimen for fiber type B were prepared.

The double punch testing set up consists of a compression testing machine, load shell, two steel punches, two LVDTs ((Linear Variable Differential Transducer) and DAQ (Data Acquisition System). During the testing, a bottom steel punch was placed on the top of a plate which rests on the loaded shell. 6 in. × 6 in. specimen was placed on the top of the bottom steel punch and the top steel punch was placed. The top and bottom punch should be perfectly aligned at the center of the specimen to make sure that there is no eccentric loading applied. And the load is applied from the compression machine at a constant loading rate of 0.04 in./min. The load shell measures the load applied and two LVDTs measure vertical axial deformation and the data was recorded by DAQ.

Results

The figure 3.63 to figure 3.66 shows the load versus displacement curve of the bottom specimens. The duplicate y axis represents the equivalent tensile stress of the SIFCON calculated using the following equation.

$$f_f = \frac{0.75 \times P}{\pi(1.2bh - a^2)}$$

Where f_t is equivalent tensile stress, P is applied load, b is radius of cylinder, h is height of cylinder, and a is radius of punches.

The Figure 3.64 shows the load versus deformation up to 0.9 in. and the figure shows the load versus deformation up to 0.6 in for the bottom specimens. One average response of UHP-FRC, three response of SIFCON with fiber type A and one response of SIFCON with fiber type B have been presented. The SIFCON with fiber type B surpasses the all the results and the maximum equivalent tensile stress obtain is 2.1 ksi for the corresponding displacement of 0.4 in. The direct tensile stress using the dog bone specimen was recorded as 2.3 ksi explained in the Section 3.3.

The Figure 3.65 shows the load versus deformation up to 0.9 in. and the figure shows the load versus deformation up to 0.6 in for the top specimens. One average response of UHP-FRC, three response of SIFCON with fiber type A and one response of SIFCON with fiber type B have been presented. Similar to the bottom specimens, the SIFCON with fiber type B surpasses the all the results and the maximum equivalent tensile stress obtain is 2.1 ksi for the corresponding displacement of 0.38 in. The direct tensile stress using the dog bone specimen was recorded as 2.3 ksi explained in the Section 3.2.5.4.

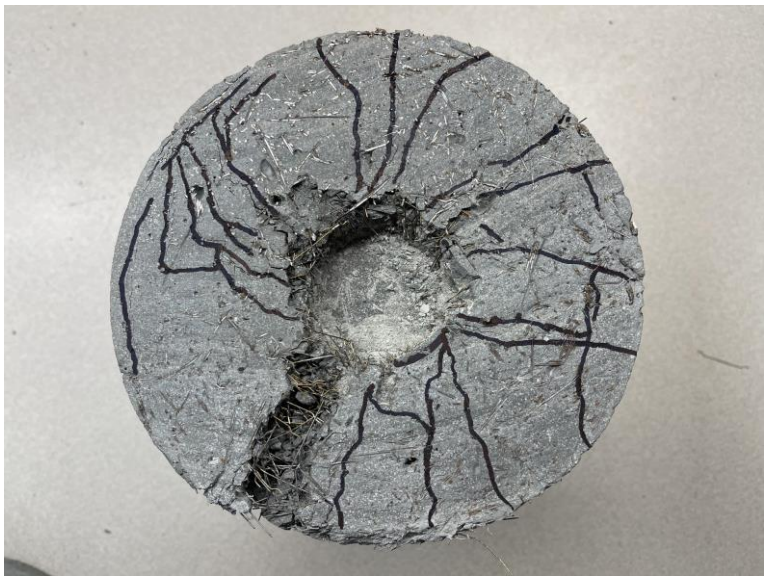

Figure 3.61 DPT Top Specimen

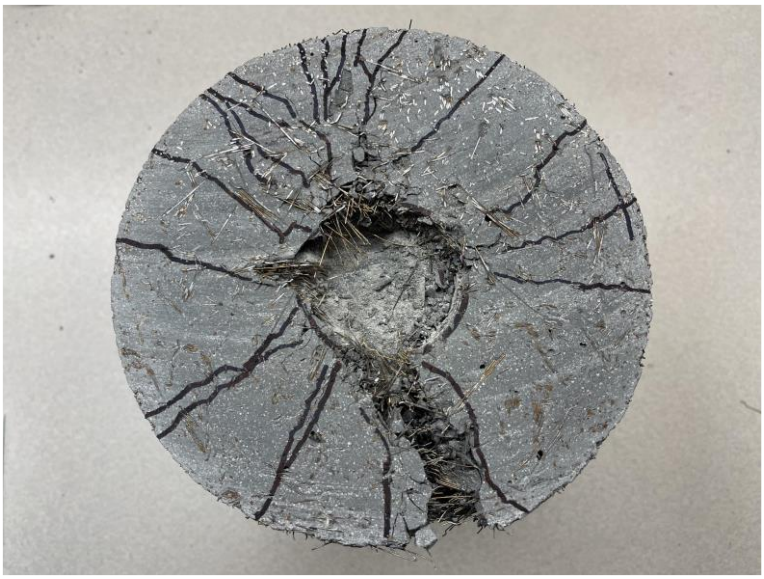

Figure 3.62 DPT Bottom Specimen

Comparison between DPT of SIFCON and UHP-FRC

A. Bottom DPT of SIFCON and bottom DPT of UHP-FRC (Average)

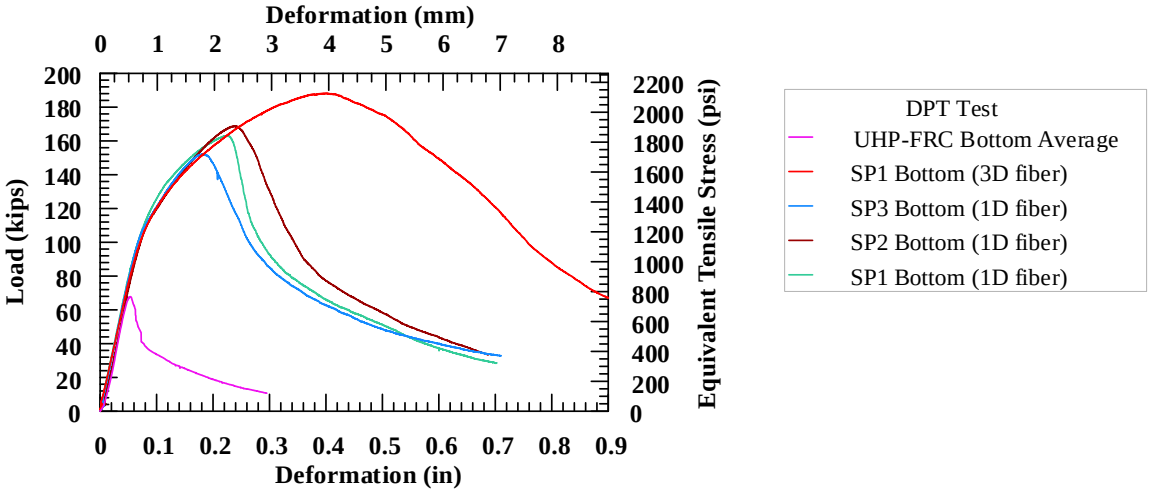

Figure 3.63 Load vs Deformation SIFCON and UHP-FRC (bottom specimen, full curve)

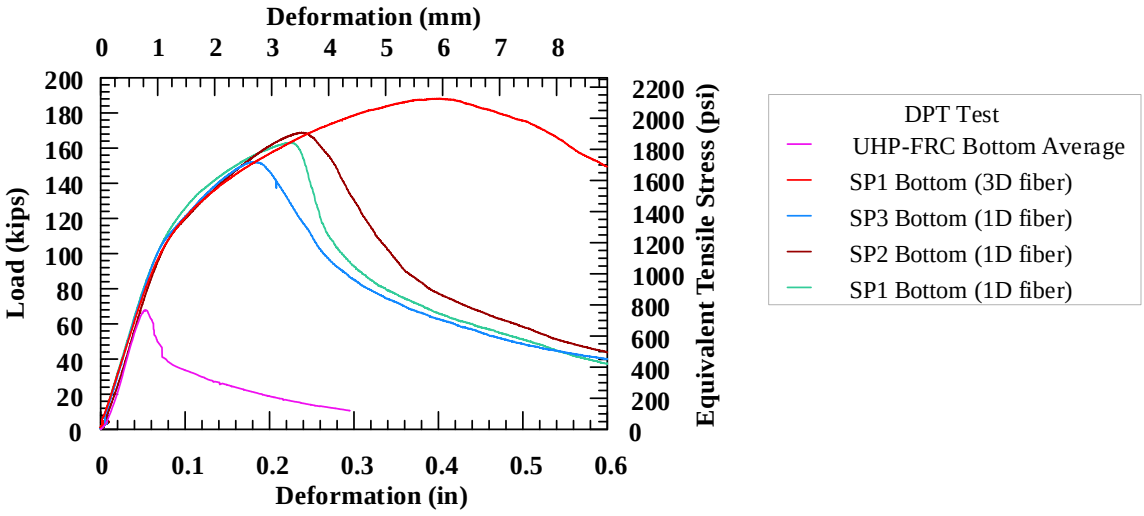

Figure 3.64 Load vs Deformation SIFCON and UHP-FRC (bottom specimen, up to 0.6 in. deformation)

B. Top DPT of SIFCON and top DPT of UHP-FRC (Average)

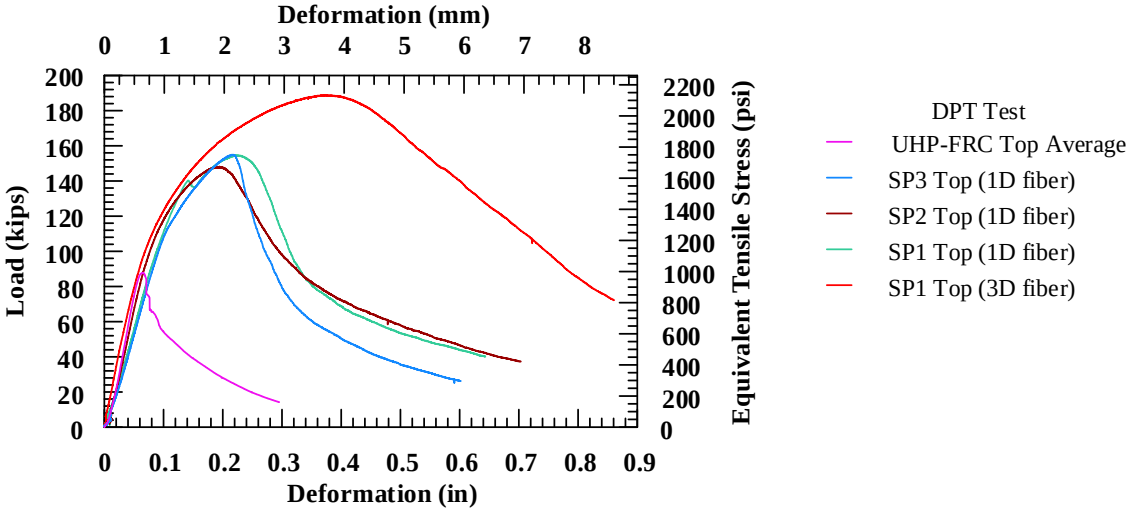

Figure 3.65 Load vs Deformation SIFCON and UHP-FRC (top specimen, full curve)

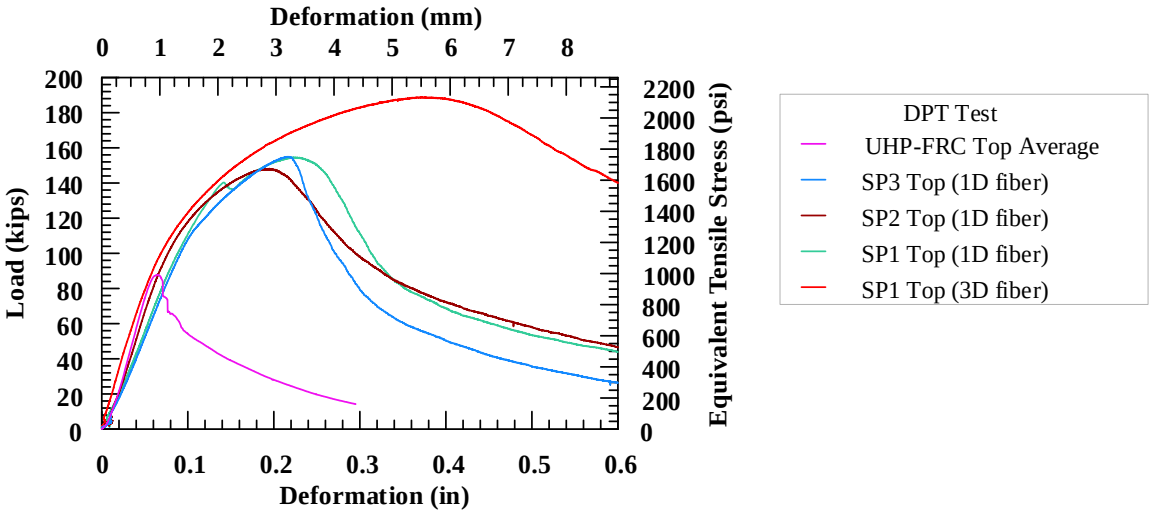

Figure 3.66 Load vs Deformation SIFCON and UHP-FRC (top specimen, up to 0.6 in. deformation)

3.2.5.4 Direct Tensile Testing of SIFCON

Sample preparation and testing

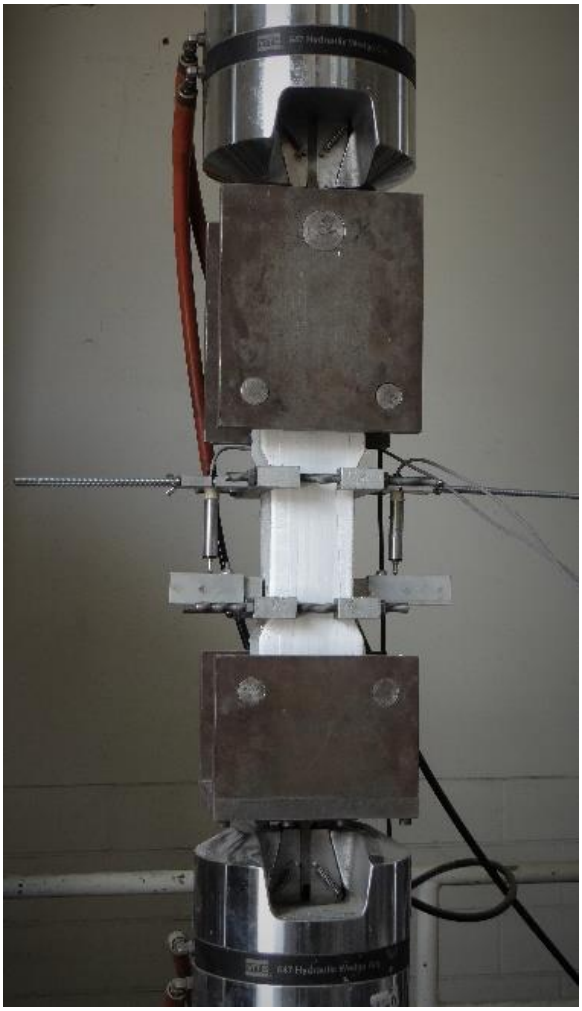

Figure 3.67 Direct Tensile Testing Setup

Six dog bone specimens with fiber type A and six dog bone specimens with fiber type B were prepared as per the process described in Section 3.2.3. After unmolding them in 24 hours, three dog bone specimens with fiber type A were put in the oven for 6 days at a temperature of 76 F with water placed on side of them to maintain the humidity and tested them in 7 days of age. Three dog bone specimens with fiber type A and three dog bone

specimens with fiber type B were submerged in water and taken out from water before 48 hours of testing and stored in the laboratory environment and tested in 28 days. Three dog bone specimens with fiber type B were submerged in water and kept for long-term testing.

The testing system consisted of a computer-controlled universal testing machine having a hydraulic wedge grip, two steel fixtures for dog bone specimens as shown in Figure 3.67, two LVDTs ((Linear Variable Differential Transducer), and DAQ (Data Acquisition System). The hydraulic grip grips the two steel fixtures as shown in the figure. During the testing, two LVDTs were connected on the opposite of the specimens to measure the deformation of the specimens and connected to the DAQ. The load signal was taken directly from the testing machine and it is connected to the DAQ. The tension test was performed on the displacement control mode with a constant rate of 0.04 in./min.

1. DTT of SIFCON and UHP-FRC (Full Curve)

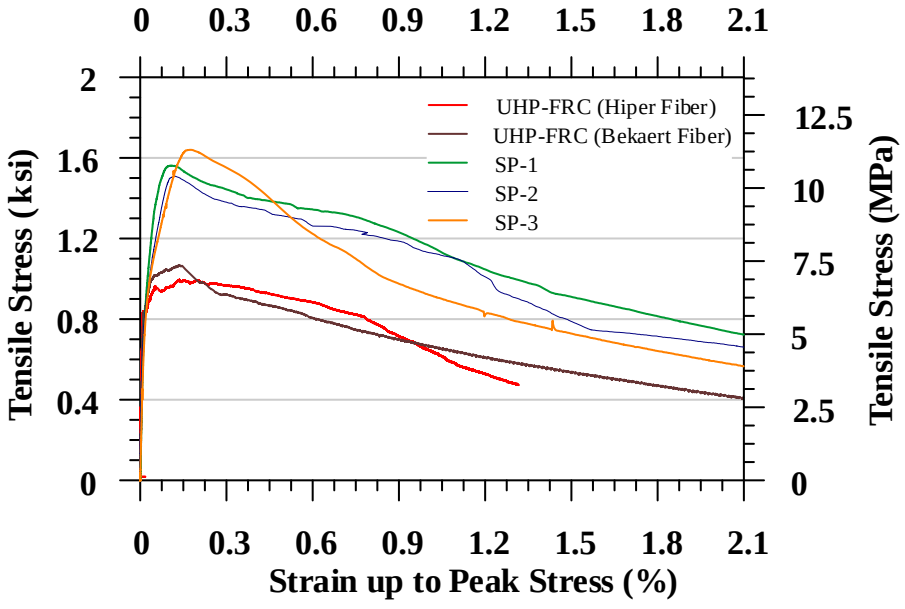

Figure 3.68 Stress Strain Plot of SIFCON and UHP-FRC (fiber type A)

2. DTT of SIFCON and UHP-FRC (Strain up to 1%)

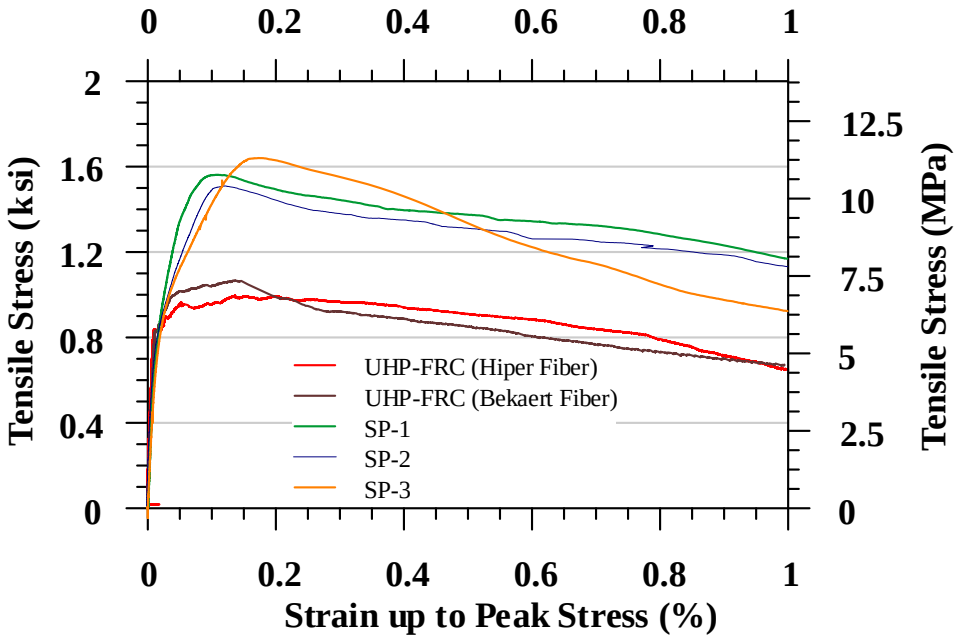

Figure 3.69 Stress Strain Plot of SIFCON and UHP-FRC (Strain up to 1%, fiber type A)

3. DTT of SIFCON and UHP-FRC (Strain up to 0.5 %)

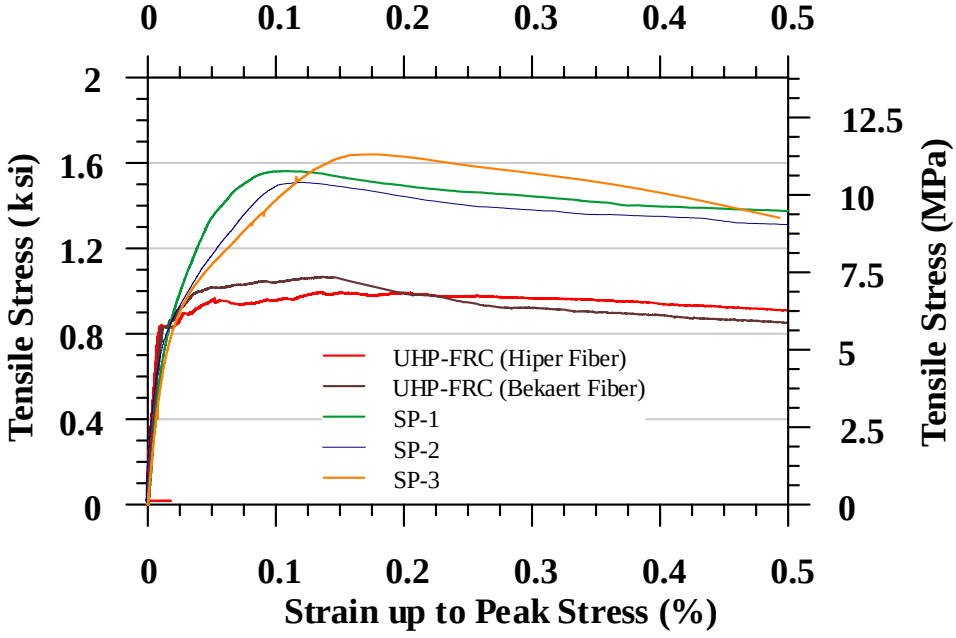

Figure 3.70 Stress Strain Plot of SIFCON and UHP-FRC (Strain up to 0.5%, fiber type A)

4. DTT of SIFCON and UHP-FRC (Full Curve)

Figure 3.71 shows the tensile stress and tensile strain response up to complete separation. The SIFCON can hold the stress up to 5% stain level while UHP-FRC fails around 2% strain level. The curve may be divided into two parts, ascending branch up to peak load and descending branch from peak load. Figure 3.72 shows the stress-strain results where strains are plotted up to an equivalent 2 percent value.

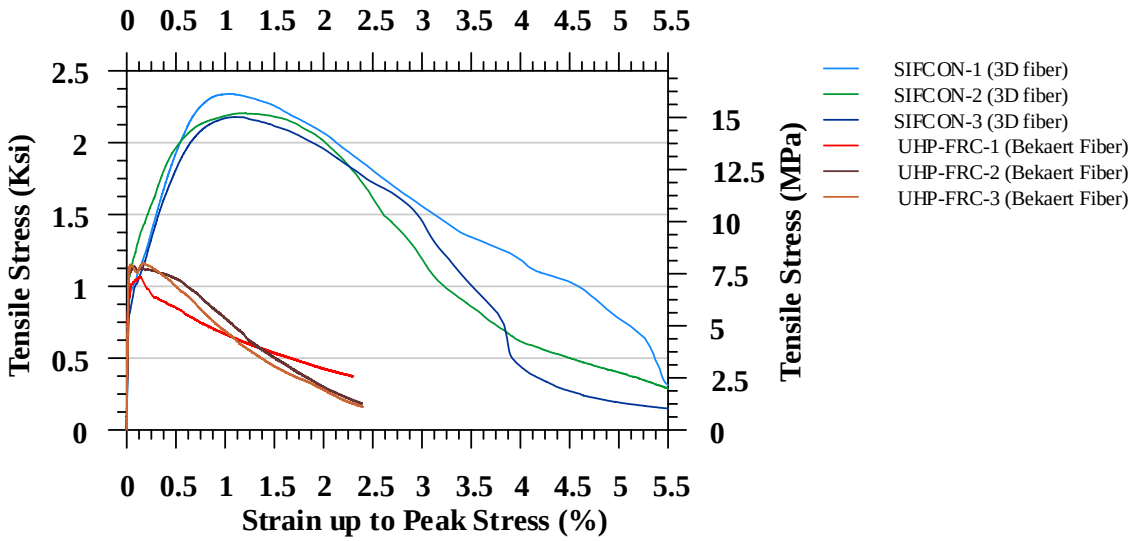

Figure 3.71 Tensile Stress vs Strain up to Peak Stress (strain up to 5.5) (UHP-FRC and SIFCON, fiber type B)

The maximum tensile stress recorded was 2.34 ksi for an equivalent tensile strain of 1.07%. The same specimen continues to hold 2.1 ksi stress at the strain level of 2%. The specimen continues to hold the stress of 1.55 ksi for a strain level of 3%, 1.2 ksi for 4%, and 0.75 ksi for 5% tensile strain. This superior ductility of the SIFCON is due to the slip hardening

properties of 3D Hooked fiber. The outstanding frictional and mechanical interlock of the 3D Hooked fiber and the bond strength is higher in the case of 3D fiber.

5. DTT of SIFCON and UHP-FRC (up to 2%)

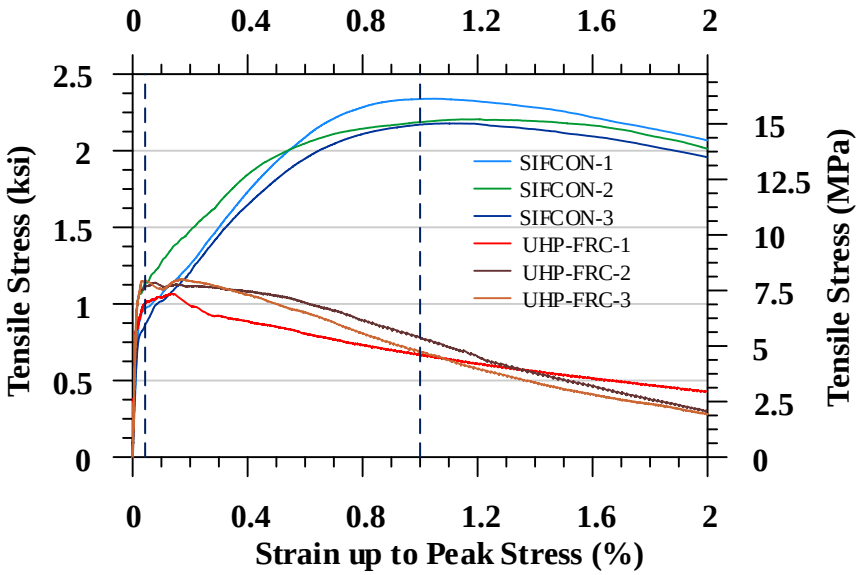

Figure 3.72 Tensile Stress vs Strain up to Peak Stress (strain up to 2%) (UHP-FRC and SIFCON, fiber type B)

During the testing, several multiple fine cracks were observed and a single primary crack was developed later on in the middle of those fine cracks. Failure was due to the fiber pull out, fiber matrix debonding and loss of fiber to fiber interlock, breaking of no any fiber was observed. This tells that there is still room for the improvement of the tensile strength of SIFCON improvising the matric compressive strength.

As the testing begins, the curve is linear up to a stress equal to 0.9 ksi and then the curve becomes a nonlinear. The non-linearity of the stress-strain curve is due to the fine cracks developed in the specimen. The onset of non-linearity of the curve does not mean onset of cracking in the matrix but only the end of the composite elastic response (Homrich and

Naaman 1987). Before the development of fine cracks, very high modulus of rupture, more than 4500 ksi was recorded.

The maximum tensile stress for UHP-FRC recorded was 1.1 ksi while for SIFCON the value is 2.3 ksi which is more than 2 times higher. The stress for 1% strain was recorded as 0.7 ksi which is less than 3 times than SIFCON, and for 2% strain, UHP-FRC cannot holds around 0.3 ksi stress, which is nearly at failure stage. Figures 3.73-3.74 show the multiple cracks formed during the testing of SIFCON and Figure 3.75 shows the pull-out failure of fibers.

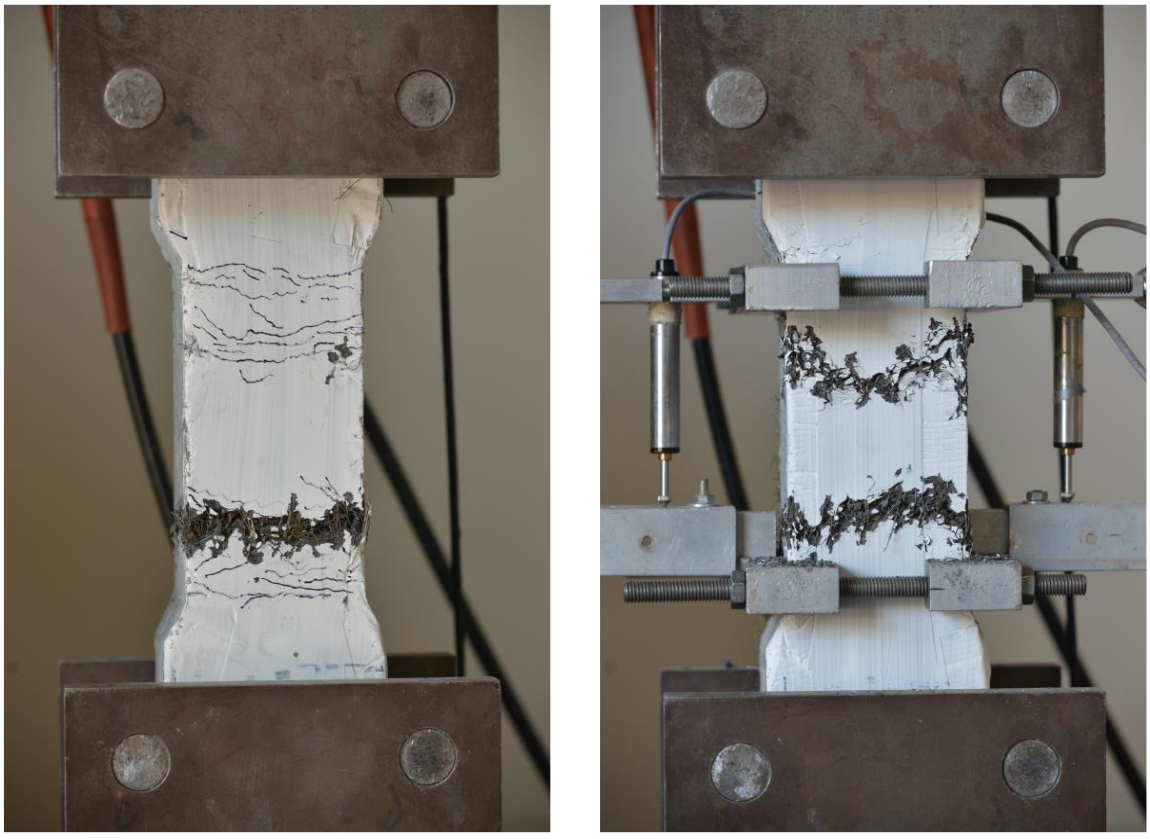

Figure 3.73 Dog Bone Specimens for SIFCON, Fiber type B, Several Micro Cracks (a) Specimen 1 (b) Specimen 2

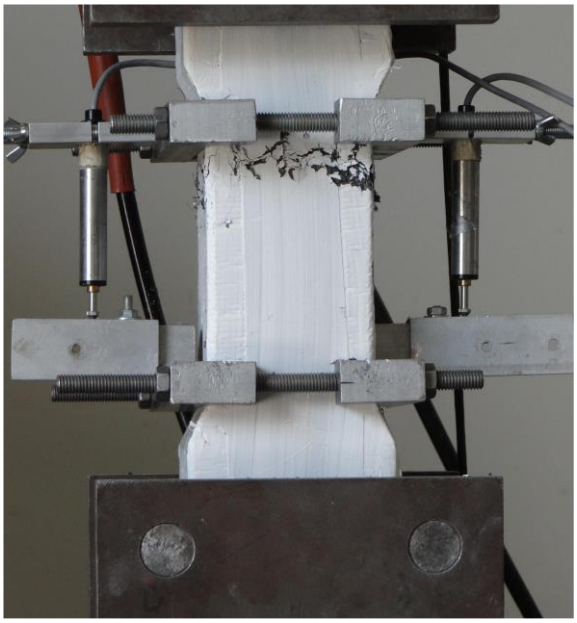

Figure 3.74 Initiation of Cracks (dog bone specimen for SIFCON, fiber type B)

Figure 3.75 Failure due to Pull-out of Fibers, SIFCON, Fiber Type B

3.3 Direct Tensile Testing of UHP-FRC for Large Scale Specimens

Experimental program

In this research large scale dog bone specimens having cross sectional area of 16 in^2 were prepared. For each specimens, the specimens were demolded after 24 hours of casting and kept them inside the curing room for 28 days. The specimens were tested after 28 days following the testing procedure explained in Section 3.2.5.4. The testing set up is shown in the Figure 3.77. The following Figure 3.76 shows flowchart of the specimens tested. All the specimens testing in this research program has shown in Figure 3.78.

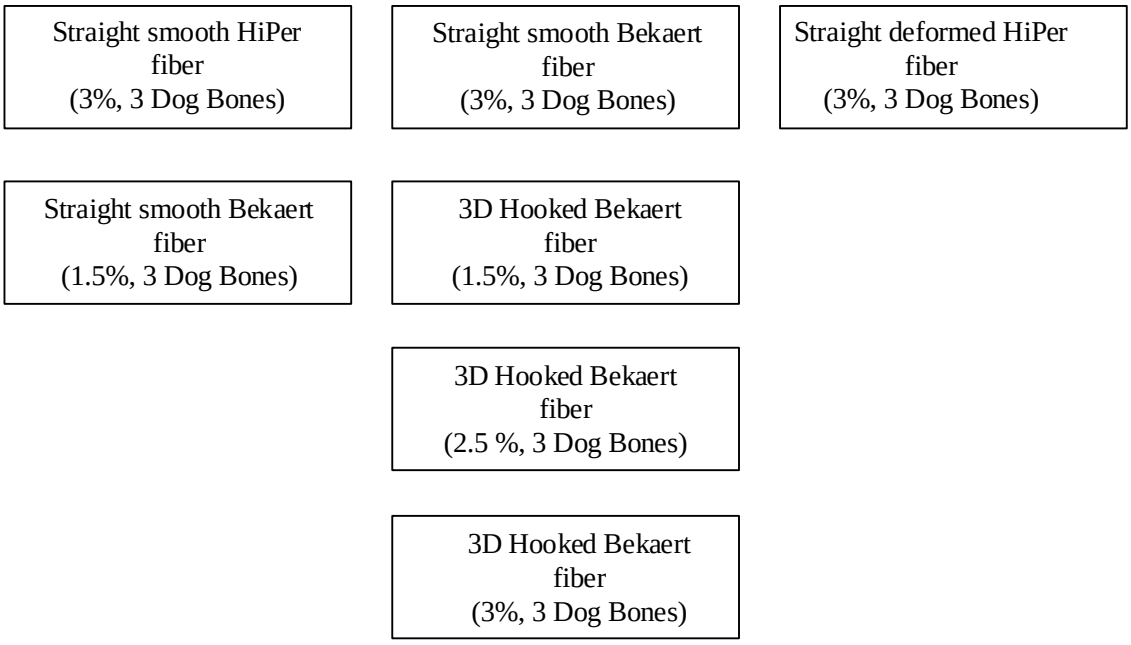

- Total 21 Dog Bone Specimens
- All the specimen have gauge area 16 square inches.

Figure 3.76 Direct Tensile Testing Flowchart

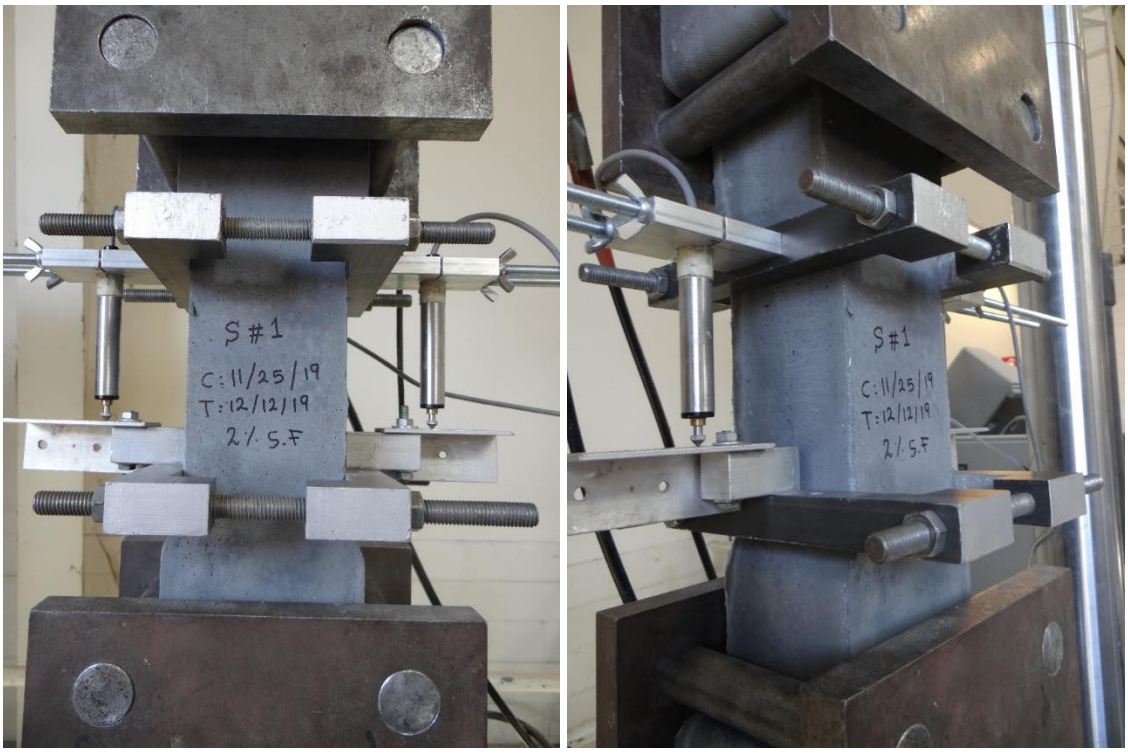

Figure 3.77 Dog Bone Specimens for Straight Fibers

Figure 3.78 Tested Dog Bone Samples

3.3.1 UHP-FRC with Micro Straight Fiber and Hooked End Fiber

Direct tension testing of UHP-FRC with straight microfiber (Bekaert) 3%, straight microfiber 1.5% and 3D Fiber 1.5%. The following Figures 3.79-3.84 shows that 3D fibers shows the similar ductile behavior as straight microfiber. The tensile strength of specimen with 1.5% straight microfiber is slightly less than 3% straight micro fibers. Figure 3.85 shows the specimens for different dosage of steel fiber.

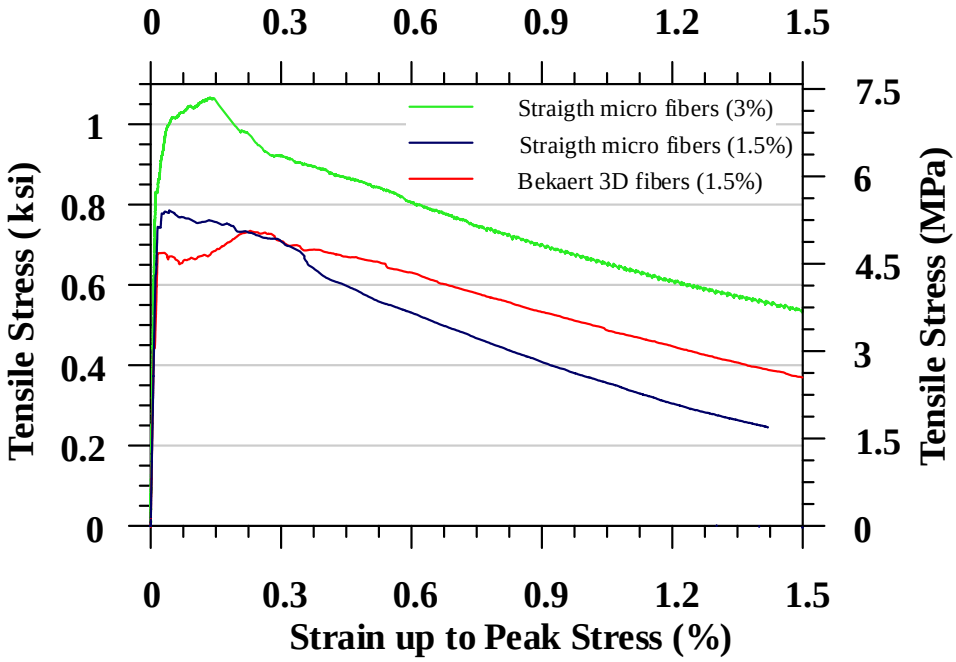

Figure 3.79 DTT of UHP-FRC Strain up to 1.5% (average of 3 specimens)

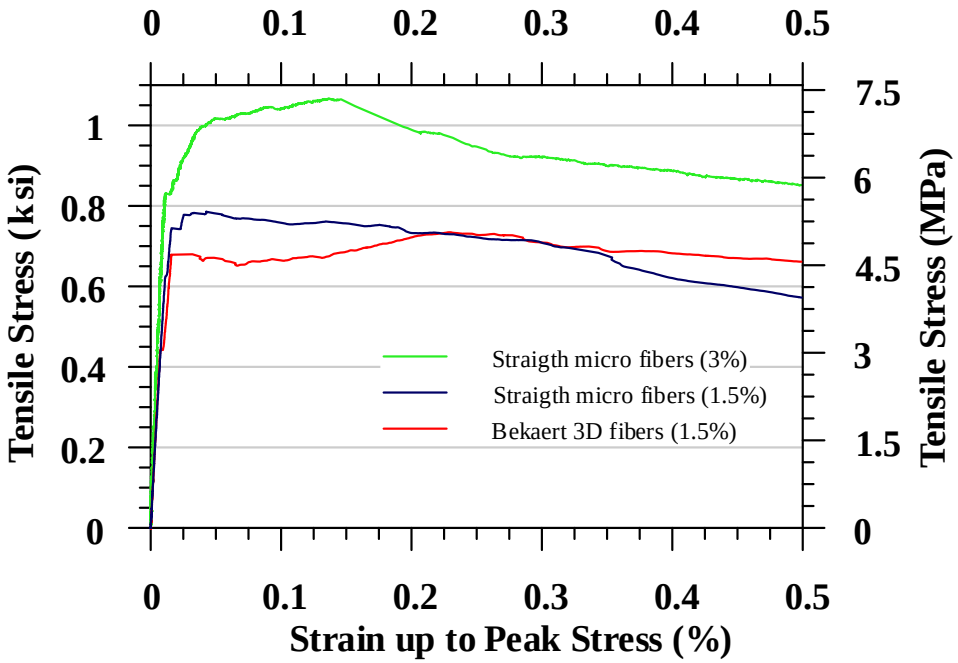

Figure 3.80 DTT of UHP-FRC Strain up to 0.5% (average of 3 specimens)

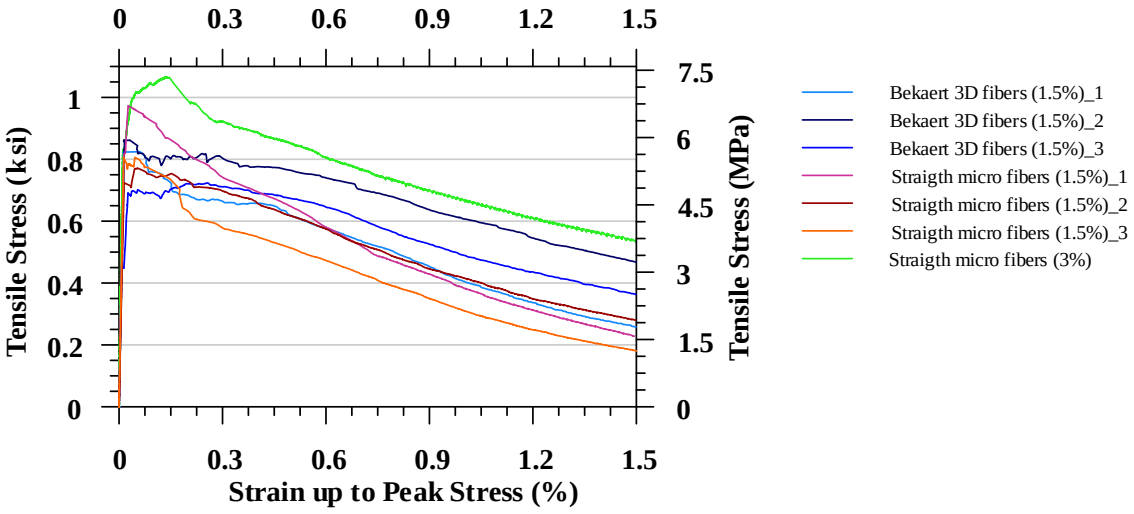

Figure 3.81 DTT of UHP-FRC Strain up to 1.5%

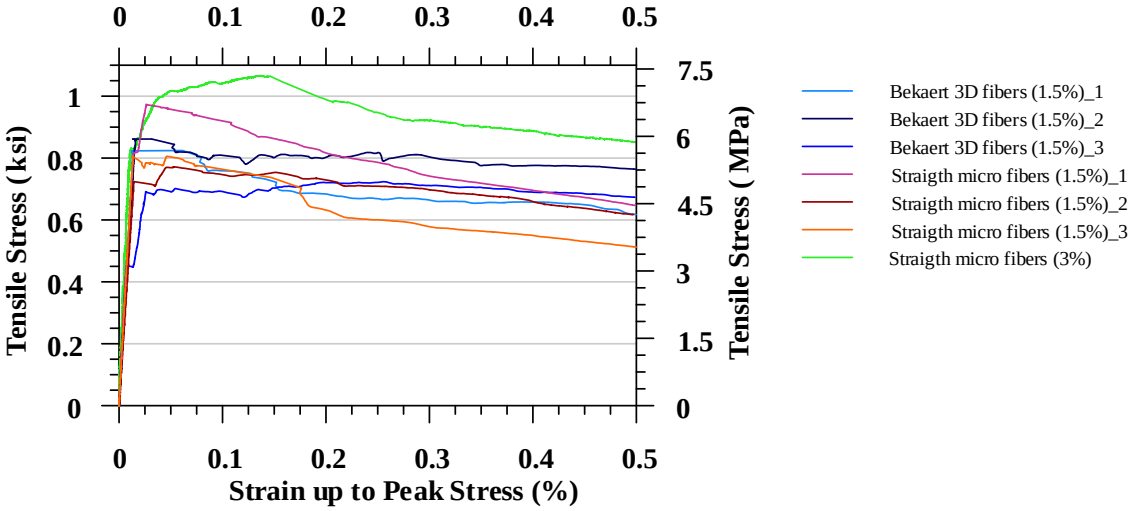

Figure 3.82 DTT of UHP-FRC Strain up to 0.5%

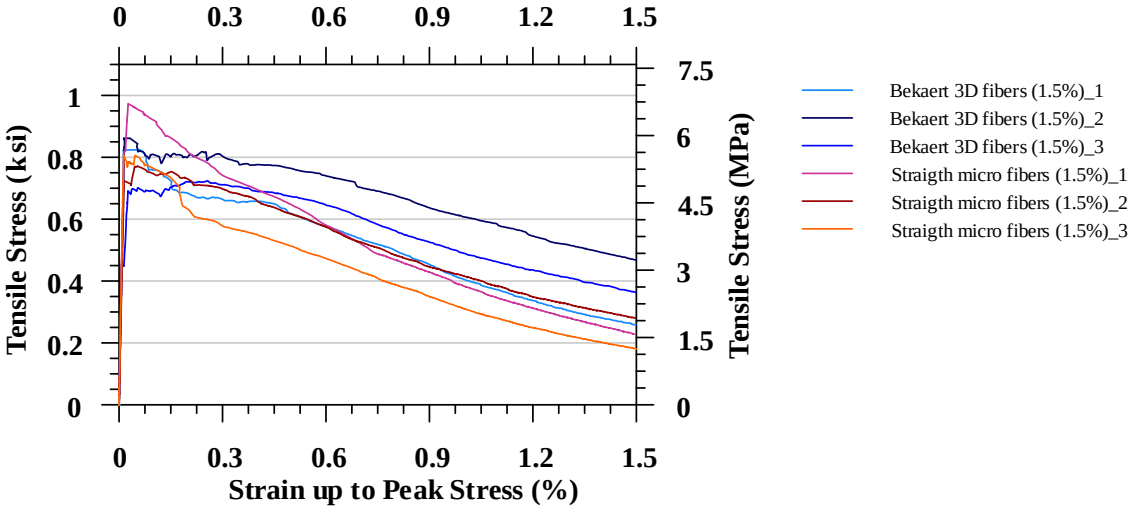

Figure 3.83 DTT of UHP-FRC Strain up to 1.5%

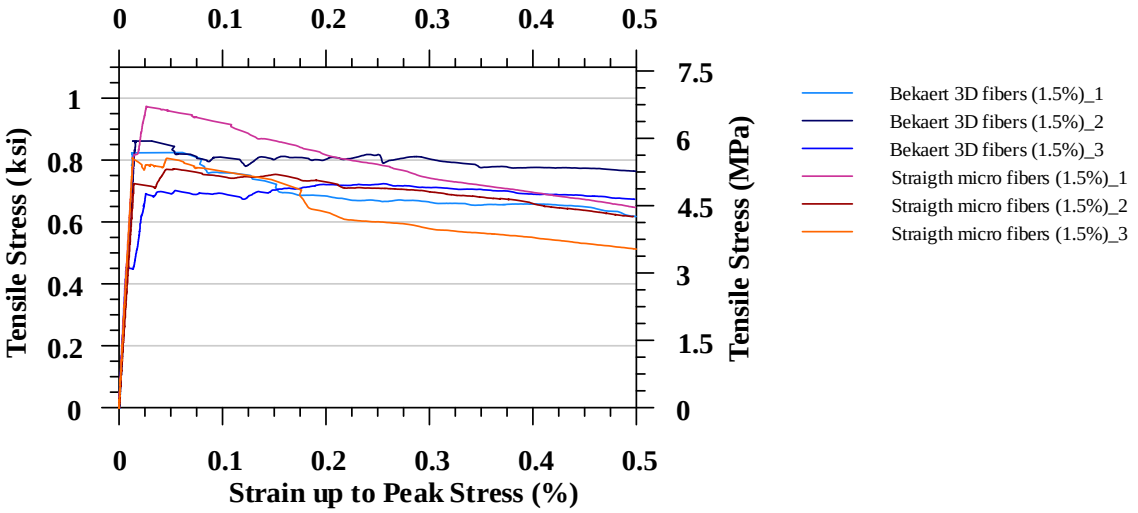

Figure 3.84 DTT of UHP-FRC Strain up to 0.5%

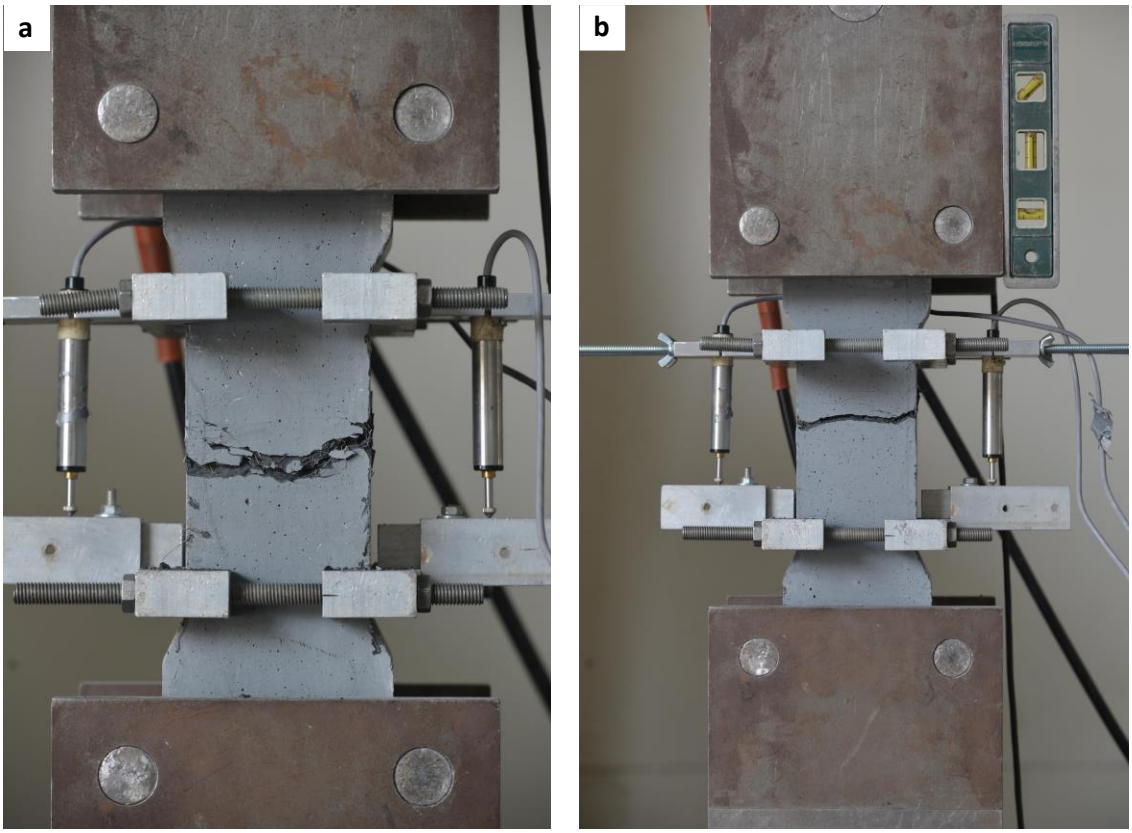

Figure 3.85 Dog Bone Specimens (a) 3D fiber 1.5%, (b) Straight Fiber 1.5%

3.3.2 UHP-FRC with Smooth Straight Fiber and Deformed Straight fiber

Direct tension testing of UHP-FRC with smooth microfiber (HiPer) 3%, smooth microfiber (Bekaert) 3%, and deformed microfiber (HiPer) 3%

Compared with the smooth fibers, the deformed fibers gave a higher composite tensile strength but a lesser ductility and a more drastic degradation beyond peak load as shown in Figures 3.86-3.87. From the observation during the testing, there was a sudden crack open-up along the major crack. This does seem to indicate that the bond between the fiber and the matrix is too strong, which could have damaged the matrix before the inelastic deformation of the fibers could happen.

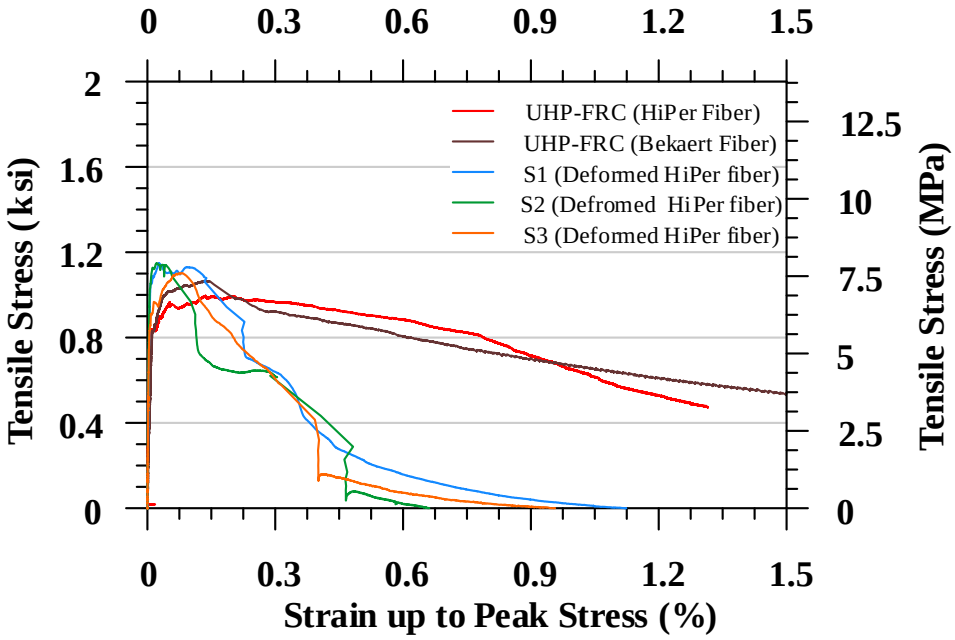

Figure 3.86 DTT of UHP-FRC strain up to 1.5%

The higher composite tensile strength can be attributed to the high bond strength as well. Nonetheless, the results do not necessarily mean the deformed fibers are not suitable for UHPC. Should the compressive be stronger (>25 ksi or so), it could force the fiber's inelastic deformation to occur first hence a slip-hardening behavior and a

more ductile composite behavior. Figures 3.88-3.91 shows the direct tensile specimen and their failure modes.

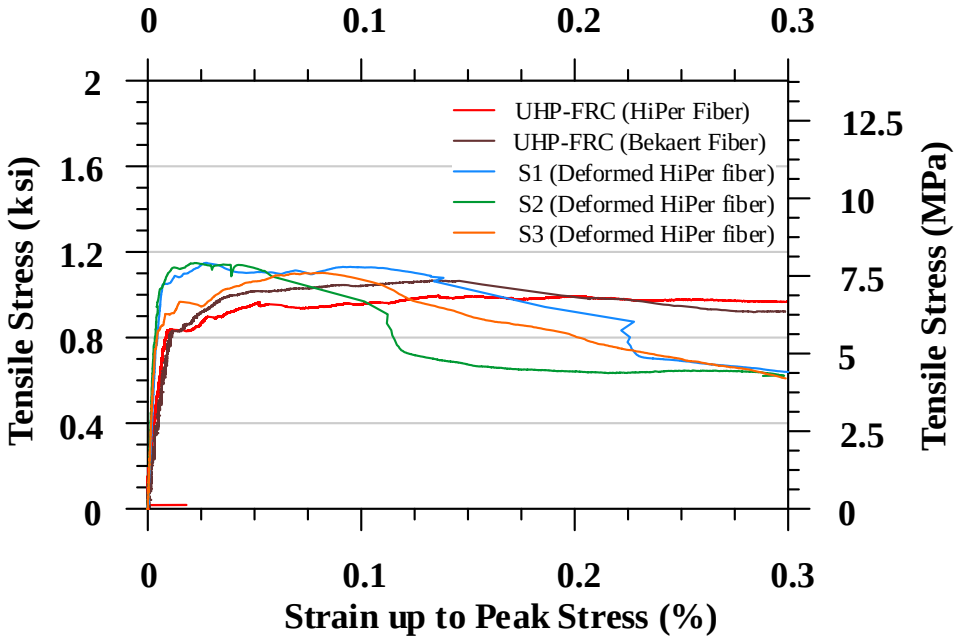

Figure 3.87 DTT of UHP-FRC strain up to 0.3%

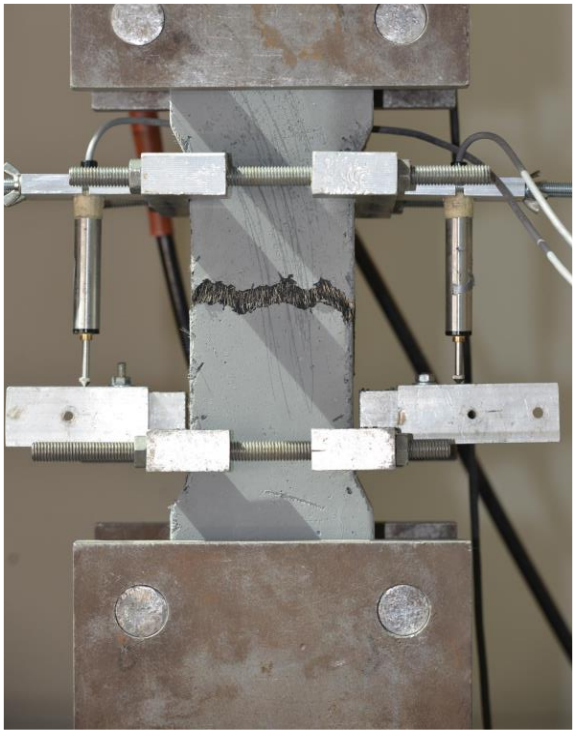

Figure 3.88 Dog Bone Specimens (deformed fiber, 3%)

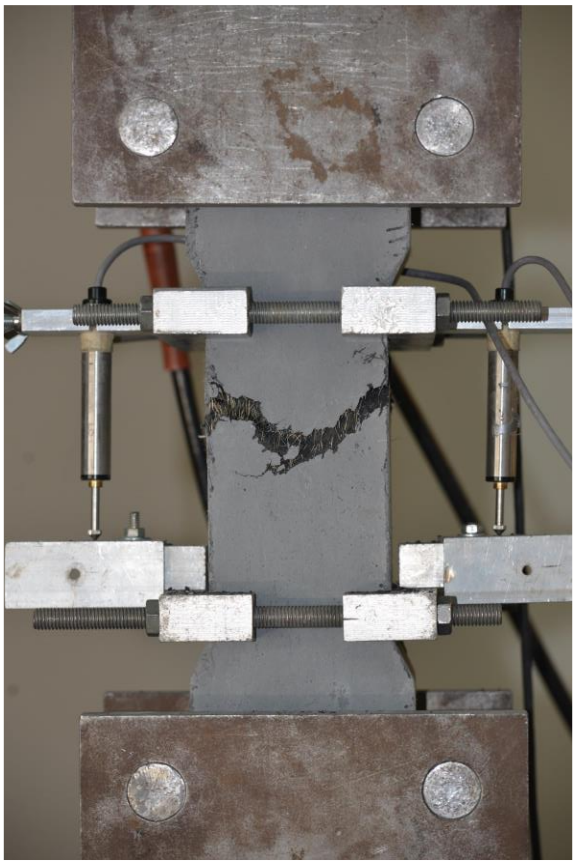

Figure 3.89 Dog Bone Specimens (deformed fiber, 3%)

Figure 3.90 Crack Zone (Dog Bone Specimens (deformed fiber, 3%))

Figure 3.91 Pull-out of Fibers (Dog Bone Specimens (deformed fiber, 3%)

3.3.3 UHP-FRC with Micro Straight Fiber (Bekaert) and Micro Straight Fiber (HiPer)

Direct tension testing of UHP-FRC with straight microfiber (Bekaert) 3%, straight microfiber (HiPer) 3%.

The following Figures 3.92-3.93 shows that both type of fibers (Bekaert and HiPer) show the similar ductile behavior as straight microfiber. The maximum tensile strength obtained was 1.1 ksi.

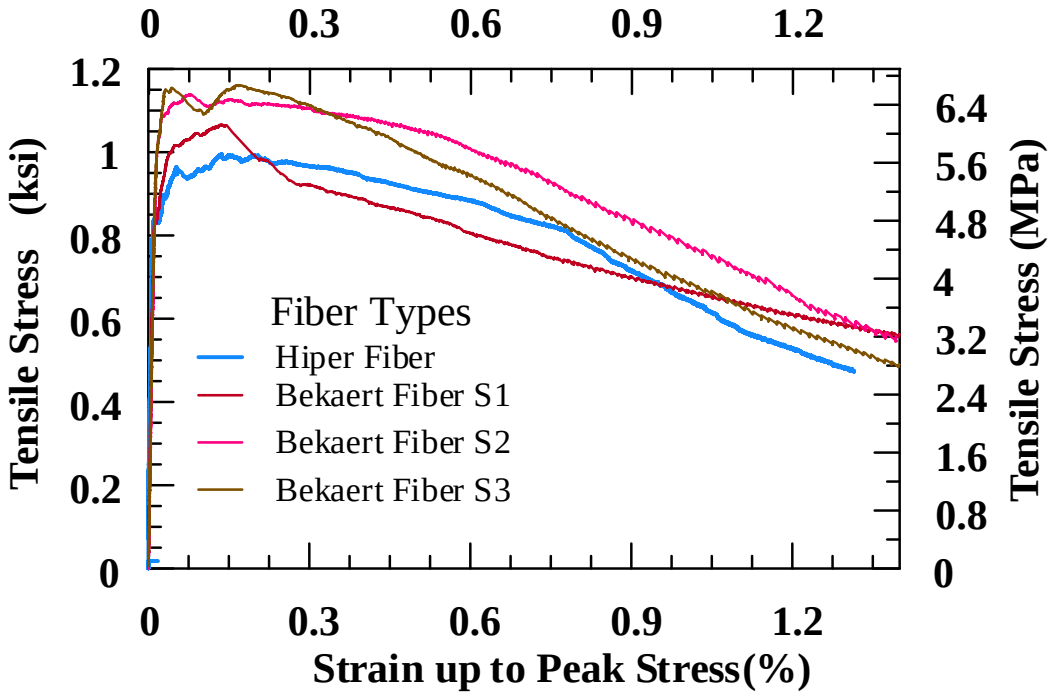

Figure 3.92 DTT of UHP-FRC strain up to 1.4 %

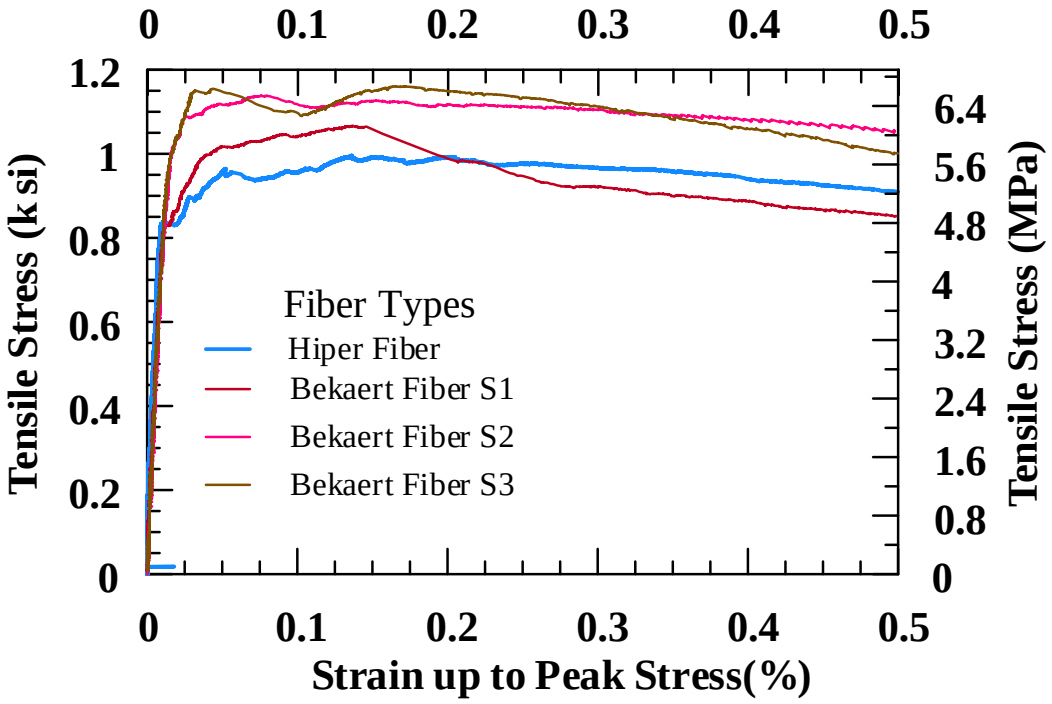

Figure 3.93 DTT of UHP-FRC strain up to 0.5%

Figure 3.94 Dog Bone Specimens (smooth HiPer fiber, 3%)

3.4 Early-Age Shrinkage Control of UHP-FRC

UHP-FRC has superior mechanical properties in the hardened state; however, it is susceptible to early-age shrinkage and cracking potential due to high binder content and low water-to-binder ratio (w/b). The early-age shrinkage can result from both autogenous shrinkage and drying shrinkage. Such shrinkage can increase the risk of cracking at an early age and cause impairment of durability, bond, and structural integrity. The measures investigated in this study were primarily for drying shrinkage however it has been shown by other studies that they could partially reduce the autogenous shrinkage [66].

3.4.1 Measurement of Shrinkage of UHP-FRC

To measure the shrinkage (both autogenous shrinkage and drying shrinkage) of UHP-FRC in one dimension, the following setup was used. It consisted of the measurement of shrinkage of a beam from its two sides. A beam of the size 6×6×21 inches was chosen. After 4 hours of UHP-FRC cast, as soon as the beam became self-standing, the two ends of the mold were removed, and small steel plates were glued onto both sides. Two LVDTs were used to measure the shrinkage of the beam. The two LVDTs used in this study can read a deformation up to 0.0001 mm.

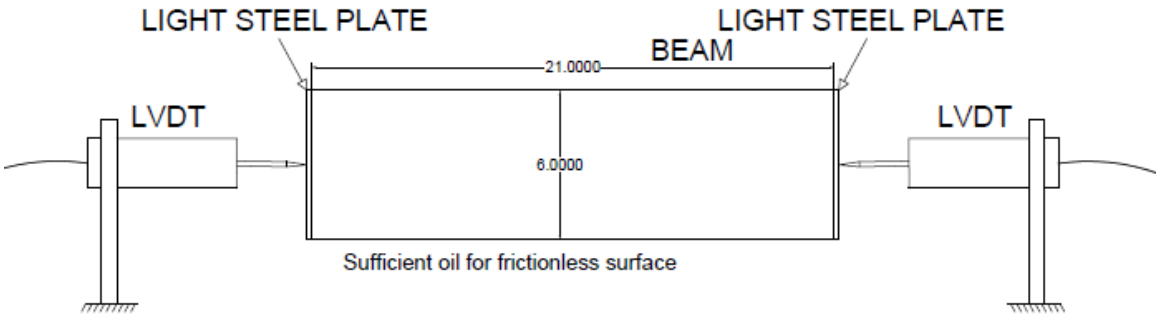

Figure 3.95 Measuring of Linear Shrinkage in this Study

Figure 3.96 Specimens Subjected to Air and Heat (Simulation of external worst environment)

The result of the shrinkage measurement of UHP-FRC is shown in the following curve. The following observations are obtained from the measurement:

a. Shrinkage developed at its fastest rate in the first 24 hours (First day).

b. After 100 hours (4 days), shrinkage in UHP-FRC stabilizes and occurs at an infinitely small rate.

One major drawback of this method of measuring shrinkage is that the early hour shrinkage cannot be measured. Few hours should wait for self-standing of concrete to measure the shrinkage.

The following two shrinkage mitigation measures have been experimented with this research.

1. Use of shrinkage reducing admixture (SRA)

2. Use of concrete curing compound.

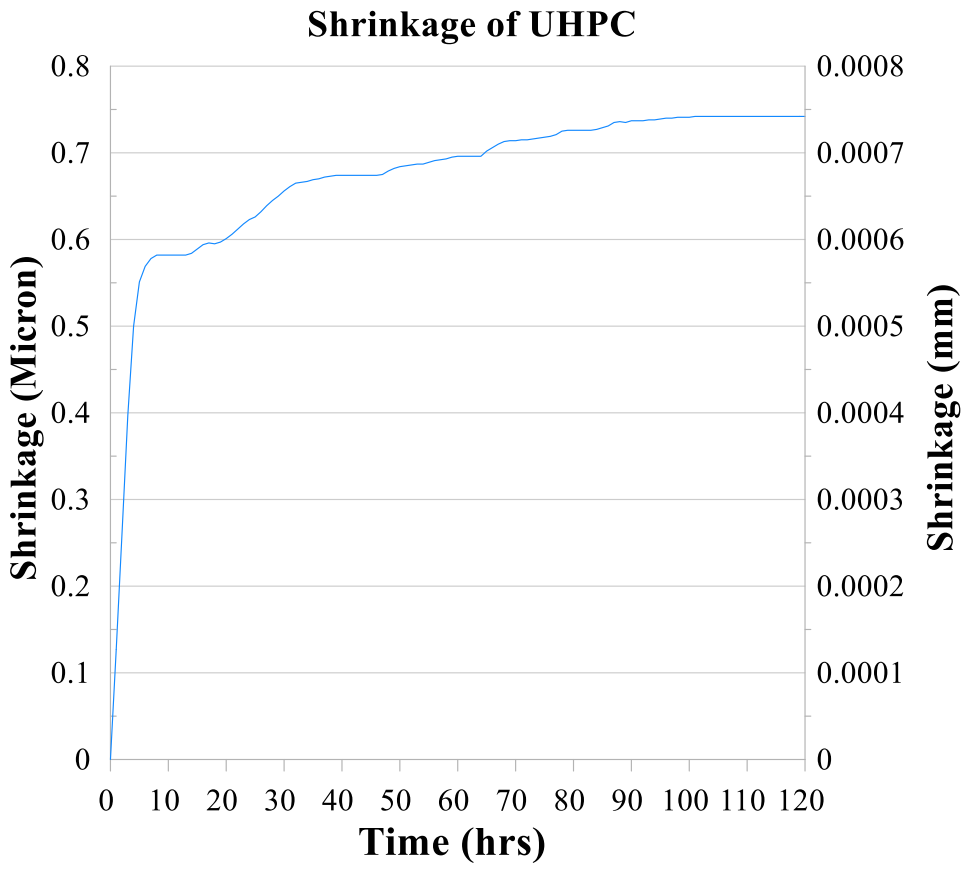

Figure 3.97 Shrinkage vs Time curve of UHP-FRC

3.4.2 Use of Shrinkage Reducing Admixture (SRA)

Shrinkage reducing admixture produced by NYCON was used for this purpose to examine the effect of SRA on UHP-FRC. SRA was used for two different ratios, 0.5% by weight of binder and 1% by weight of the binder.

Six 2×2×2 UHP-FRC cubes with 0.5% SRA and six 2×2×2 UHP-FRC cubes with 1% SRA were prepared. Also, two 6×6×21 beams were prepared with half of the specimen with normal

concrete and half of the specimen with UHP-FRC having 0.5% and 1% SRA content respectively. All the specimens were kept outside of the laboratory to expose them to the harsh environment to simulate the real field situation. From the observation, after casting the specimens, swelling of the UHP-FRC was observed immediately after 30 minutes of casting. The swelling rate was very high at the beginning and the rate of swelling was reduced when time goes on. The swelling action was observed for initial 8 hours. Figure 3.98 shows the swelling of UHP-FRC at 1% SRA dosages.

Figure 3.98 Swelling of UHP-FRC (a) UHP-FRC Cubes

Figure 3.99 UHP-FRC and normal concrete beam

The compressive strength of cubes specimens for UHP-FRC without SRA, UHP-FRC with 0.5% SRA, and UHP-FRC with 1% SRA were tested at 24 hours and 28 days. The compressive strength of the UHP-FRC with SRA was found to be decreased dramatically and the result of each of the specimens have presented in the following tables. Table 1 presents the test results at 24 hours and Table 2 presents the test results after 28 days.

Table 3.5 Compressive Strength of Cube Samples with and without SRA at 24 Hours (exposed to external environment)

Cube Casting date: 04/01/2019

Cube Testing date: 04/02/2019

Sample No	Ultimate Force (lb.)	Compressive Strength (ksi)	Average Compressive Strength (ksi)	Percentage Drop in Strength
Exposed to External Environment				
UHP-FRC_1	11,869	2.97	3.16	
UHP-FRC_2	12,992	3.25		
UHP-FRC_3	13,072	3.27		
UHP-FRC+(0.5% SRA)_1	4,895	1.22	1.51	52.37%
UHP-FRC+(0.5% SRA)_2	6,594	1.65		
UHP-FRC+(0.5% SRA)_3	6,577	1.64		
UHP-FRC+(1% SRA)_1	4,324	1.08	1.12	64.71%
UHP-FRC+(1% SRA)_2	4,972	1.24		
UHP-FRC+(1% SRA)_3	4,092	1.02		

Table 3.6 Compressive Strength of Cube Samples with and without SRA at 28 days

Cube Casting date: 04/01/2019

Cube Testing date: 04/29/2019

Sample Number	Ultimate load (lb.)	Compressive Strength (ksi)	Average Compressive Strength (ksi)	Percentage Drop in Strength
Cured in Curing Room				
UHP-FRC_1	71,800	17.95	16.79	
UHP-FRC_2	62,482	15.62		
Exposed to External Environment				
UHP-FRC_1	42,463	10.62	10.21	
UHP-FRC_2	41,898	10.48		
UHP-FRC_3	38,134	9.53		
UHP-FRC+(0.5% SRA)_1	19,035	4.76	4.78	53.14%
UHP-FRC+(0.5% SRA)_2	19,800	4.95		
UHP-FRC+(0.5% SRA)_3	18,562	4.64		
UHP-FRC+(1% SRA)_1	19,204	4.8	4.48	56.11%
UHP-FRC+(1% SRA)_2	17,253	4.31		
UHP-FRC+(1% SRA)_3	17,300	4.33		

3.4.3 Use of Concrete Curing Compound

The curing compound consists of two constituents, water or solvent, and wax or resin. After the concrete was cast, the curing compound was sprayed onto the surface of the concrete. The water or solvent constituent evaporates leaving the wax or resin to form a membrane over the surface of the concrete. This membrane formed after the evaporation of solvent blocks the evaporation of water from the concrete and helps to retain moisture in the concrete.

Curing compound is commonly used in the precast plant to prevent shrinkage crack of large volume concrete units. The one used in this study is shown below (Figure 3.100).

Figure 3.100 Curing Compound Used in this Study

To study the effect of concrete curing compound, panels with surface area 324 in^2 were used. The panels have a high surface area to volume ratio which facilitates water evaporation and shrinkage.

In the first phase, the panels with dimensions 18×18×0.5 inches were cast and exposed to the external environment and observed for shrinkage cracking (Figure 3.101). Three panels were cast and the first panel was kept without any curing method, the second specimen was

cured with moisture curing (covering the specimen with cotton fabric and spraying the water on time to time basis) and the third panel was cured with concrete curing compound.

Figure 3.101 UHP-FRC Panels After 48 Hours: (a) No Curing, (b) Moisture Curing (c) Spraying with Concrete Curing Compound

After observation of these panels, hairline cracks (visible to human eyes) were observed in the first panel as shown in Figure 3.101 (panel without any curing), but no such cracks were observed on the panels with curing compound and conventional moisture curing.

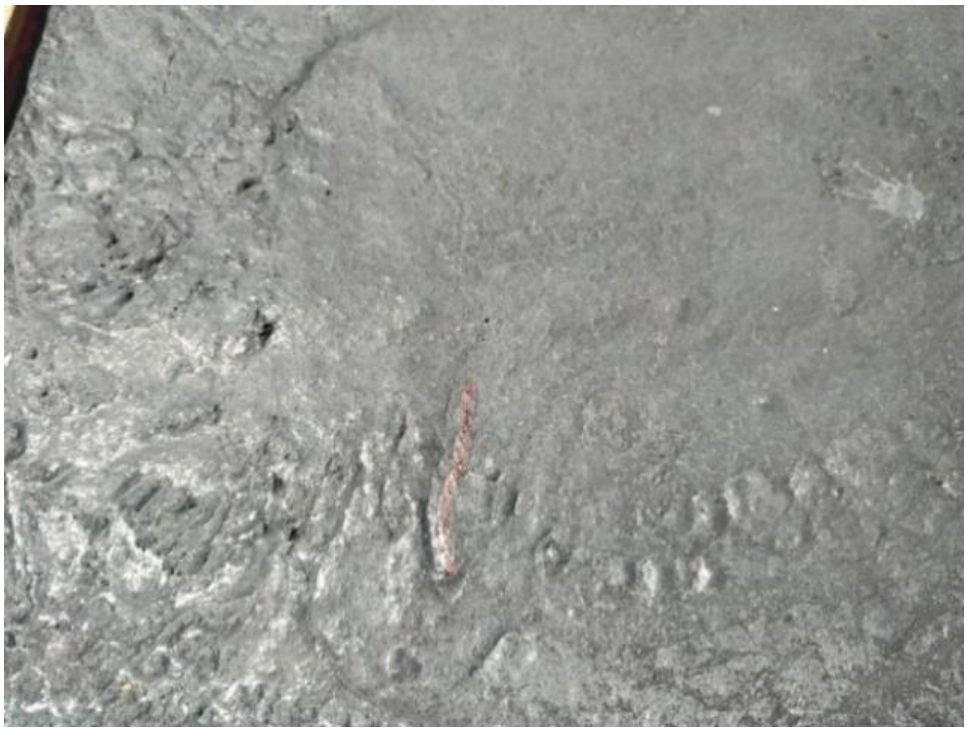

Figure 3.102 Small Cracks at UHP-FRC with No Curing

Figure 3.103 Small Cracks at UHP-FRC with No Curing

Similar to the other cementitious materials, UHP-FRC undergoes volume changes primarily due to shrinkage in unrestrained conditions without introducing significant stress in the materials. However, UHP-FRC materials are commonly reinforced by steel reinforcements that do not experience the same volume change, which limits the volume change and results in the development of tensile stress within the concrete. Whenever the tensile stress becomes greater than the tensile strength capacity of UHP-FRC, shrinkage cracking occurs.

For the better observation of early-age shrinkage, No.4 rebar were used in UHP-FRC panels in the second phase of experiment. In the second phase, panels with a larger dimension (30×30×1 inches) with 5 No.4rebars on both directions and 5 No.4 rebars placed vertically in diagonal direction as shown in Figure 3.104. The purpose of introducing the horizontal and vertical rebar is to introduce the weak point and restraint for shrinkage cracking. Three panels were cast and the first panel was kept without any curing method, the second specimen was cured with conventional moisture curing (covering the specimen with cotton fabric and spraying the water on time to time basis) and the third panel was cured with concrete curing compound.

Figure 3.104 Rebar Cage for the UHP-FRC Panel

The panel was cast during the daytime when the temperature of the surrounding was 90-degree F. Scrutinized after 48 hours, it was seen that there were multiple random cracks on the surface of the panel without curing (Figure 3.102).

The panel in shown Figure 3.106, which was cured with a concrete curing compound. The curing compound was sprayed on the surface of the panel within 30 minutes of the casting of concrete. The panel was cast during the daytime when the temperature of the surrounding was 90-degree.

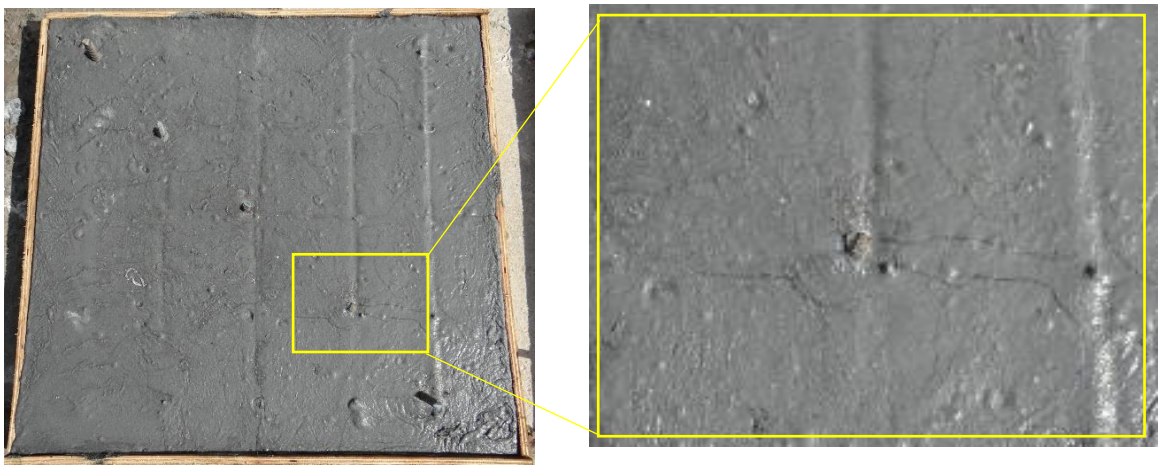

Figure 3.105 Panel with No Curing/ Shows Multiple Hair Cracks in Random Direction

Scrutinized after 48 hours, no visible cracks were observed on the surface of the panel curing with curing compound and panel with moisture curing.

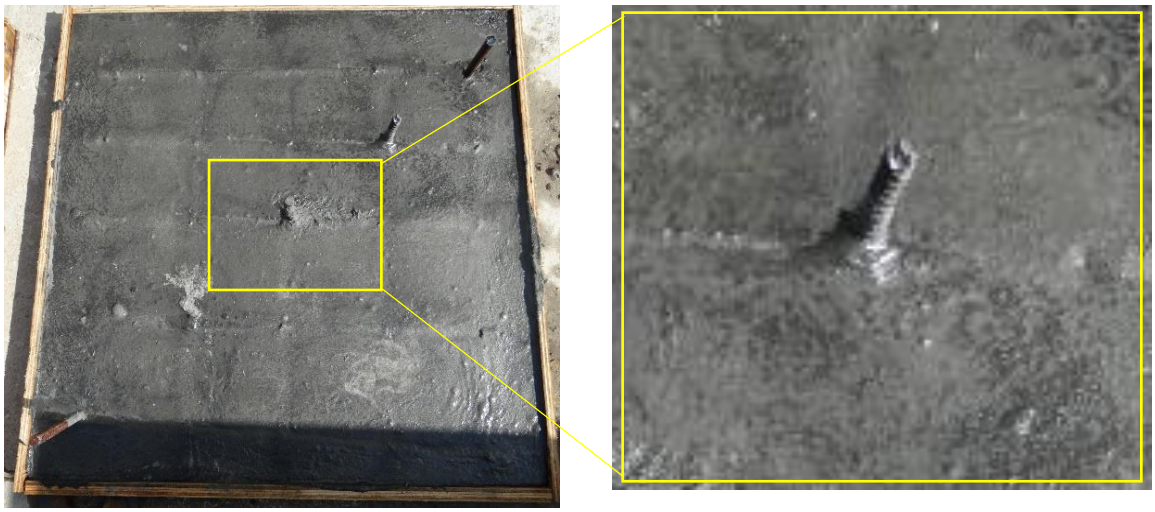

Figure 3.106 UHP-FRC Panel with Curing with Concrete Curing Compound.

3.4.4 Result and Conclusions

The study presented above shows the early-age shrinkage cracking of UHP-FRC and its mitigation measures. Although the use of shrinkage reducing admixture on UHP-FRC has a lesser propensity towards shrinkage cracking, UHP-FRC swells and there is a high chance

of denigrating the mechanical properties of UHP-FRC resulting dramatically drop in compressive strength. This finding has also been reported by a prior study [67]. On the other hand, using concrete curing compound on the surface of UHP-FRC forms a thin layer membrane that acts as a water sealant and ultimately less propensity towards early-age drying shrinkage cracking. Also, the panels with conventional moisture curing (covering the specimen with cotton fabric and spraying the water on a time to time basis) is also efficient to prevent early-age shrinkage cracking but needs to supplying water multiple times which is more time-consuming.

3.5 UHP-FRC at Elevated Temperature

Ultra-High Performance Concrete consists of very fine materials and low water to binder ratio which leads to the high particle packing density and low matrix porosity. Because of its low permeability, UHPC is susceptible to spalling at high temperatures. Spalling of concrete increases the overall damage of the structure exposed to accidental fire and leads to higher costs for repair and restoration. Sometimes it may impose the danger of the overall damage of the whole structure reducing the sectional area of loaded members and loss of protection to the reinforcement due to spalling. So in this research, the UHP-FRC developed by Aghdasi, et al. (2017) [10] has been tested for different temperature up to 435 ºC and some modifications for thermal stress release has been conducted.

3.5.1 Cause of Spalling of Concrete

Fire spalling consists of the sudden separation of concrete chunks from the heated surface of the concrete members because of interaction between cracking and the built-up of pore pressure in the pores [60]. During heating, thermal stress developed because of the steep thermal gradient between the outside hot region and inside the cold-core which leads to the tension between the outside hot region and inside the cold-core. In addition, water vaporization occurs inside the pores and which is constrained and causes the pore water pressure. The developed pore water pressure is responsible for the violent nature of spalling of concrete. Khoury (2000) [61] explains that "the kinetic of moisture migration induced by pressure gradient is very important in spalling development and it is mainly related to concrete permeability. In particular, moisture is pushed toward the cold core, where vapor condensation can occur due to the lower temperature". The condensed vapor may form the moisture clogged because of the low porosity and dense microstructure of UHPC. Moisture

clogged is responsible for the increase in vapor pressure inside it and at the same time there is a thermal expansion of clogged water. Vapor pressure, water dilation pressure, and thermal gradient acts altogether and is responsible for the brittle nature of concrete spalling. In addition to all those forces, the external stress applied also acts in favor of the developed internal force and is responsible for the disastrous nature of the concrete failure.

3.5.2 Previous Studies on Effect of Heat in High Strength Concrete

Lau and Anson (2006) tested six mixtures, included steel fiber reinforced concrete (SFRC), and non-fiber reinforced concrete (NFRC) specimens of both normal concrete (NC), and high-performance concrete (HPC) to investigate the effect of the nine different temperature levels on concrete properties, compressive strength, flexural strength, modulus of elasticity, and moisture content of concrete. It was concluded that compressive strength decreases as temperature increases and the level of severity of reduction depends on the maximum temperature attained in both (NC), and (HPC). (HPC) with 1% steel fiber shows a better response in terms of mechanical properties of concrete than (NC). As the saturation level of concrete increases, the reduction in compressive strength increases as the pore size becomes larger and thus increases the internal pressure in concrete.

Bastami et al. (2011) [62] studied the performance of high strength concretes at elevated temperatures and found that one of the main effects of high temperature on concrete structures is the reduction in compressive strength. They studied the effect of temperature on compressive strength, spalling behavior, and mass loss of high strength concrete (HSC) in terms of four parameters water to cement ratio (w/c), sand ratio, and silica fume ratio and its amount. Sixteen mixtures cast into cylinders, twelve contains silica fume, and four

without silica fume, were cast to be subjected to temperature up to 800^{o} C, with a heating rate of 20^{o} C/min. They concluded that the unheated cylinders with silica fume shows high compressive strength compared with unheated non-silica fume cylinders, whereas after heating the cylinders suffer reduction in compressive strength as well as spalling. They observed that almost 80% loss in compressive strength if the concrete is heated to 800 ºC. The cylinders with 0% silica fume spalled into two or three parts after heating. Increasing sand ratio as fine aggregate, the compressive strength increases, but vice versa in coarse aggregate case, and spalling is slightly decreased. The effect of water to cement ratio on compressive strength is mainly based on temperature exposure. At room temperature, cylinders with high w/c ratio shows reduction in compressive strength, and vice versa occurred for heated cylinder. The w/c ratio significantly reduce the spalling behavior of HSC. They also observed that increasing the water to binder ratio increased the residual compressive strength of the heated specimens. Many researchers have found that the addition of 0.1-0.2% by volume of polypropylene fiber helps to reduce the spalling phenomena and sometimes can be avoided. Polypropylene fiber melts when the temperature reached beyond 160-170 ºC and produces the voids and micro-cracks in the cement paste, which leads to the lower moisture gradient and lower pressure peak inside the concrete is observed and releases the thermal stress developed [63].

Li et al. (2019) [63] studied the effect of incorporating polypropylene (PP) fiber, steel fibers, and aggregate size on spalling behavior, and pore pressure of different concrete specimens of ultra-high-performance concrete (UHPC). They studied the individual and combined effects of these three parameters. The temperature and pore pressure was measured simultaneously at different depth. It is concluded that the addition of

polypropylene fiber increases compressive strength slightly, whereas, in the case of adding larger aggregate, there is a slight reduction due to the defect of UHPC caused by aggregate size. The addition of steel fiber shows the benefit of increasing compressive strength as it prevents the propagation of cracks. The incorporation of only (PP) fiber significantly increases the permeability as compared to large aggregate size, due to the incompatibility of thermal expansion of the (PP) fiber and mixture, as well as melting of (PP) fiber. The inclusion of only large aggregate or steel fiber independently shows severe spalling due to low permeability, compared to an addition of PP fiber which did not observe any spalling. When the pore pressure decreases dramatically (reaches a value of zero), this means that the spalling behavior of UHPC occurred.

3.5.3 Experimental Program Flowchart

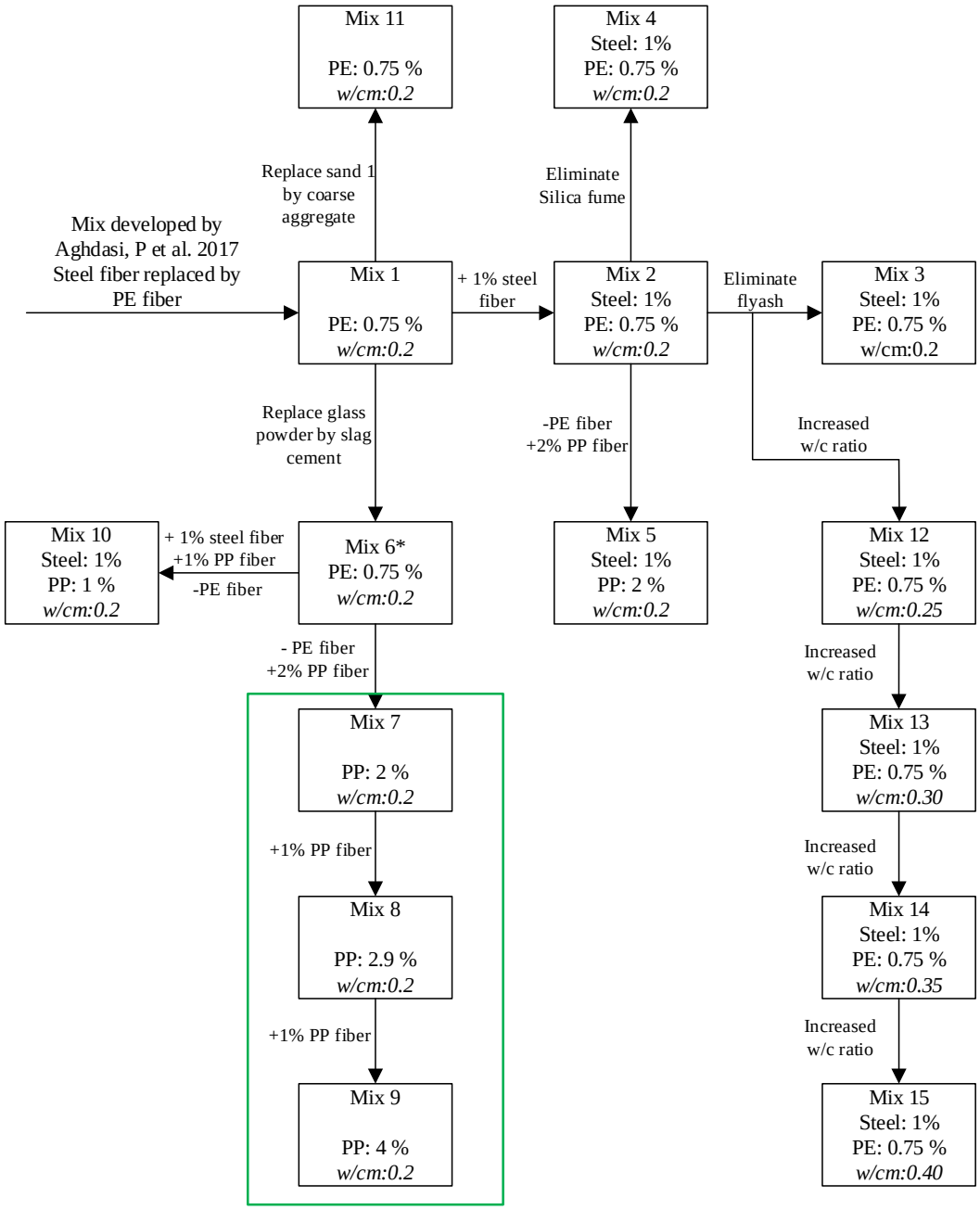

*This mix was used for Precast Pavement Implementation at Dallas/Fort worth International Airport (2019)
PE: Polyethylene fibers
PP: Polypropylene fibers
The green line means that those mixes showed no spalling effect however some surface cracks were present.

Figure 3.107 Flow Chart of Mixes

3.5.4 Sample Preparation and Testing

At least three 2 in. × 2 in. × 2 in. cubes were prepared for each trial. Sample were prepared and kept them for 28 days in the curing room at controlled temperature. After 28 days of age, the cubes were tested in high temperature following ASTM E119, “Standard Test Methods for Fire Tests of Building Construction and Materials”. Thermcraft laboratory furnace (Figures 3.108-3.111) was used for the high temperature application. Two thermocouples were used to measure the temperature, and they were placed underneath the concrete cubes while heating.

Figure 3.108 UHP-FRC cubes inside the furnace, ready for heat application

Figure 3.109 Specimens inside the furnace

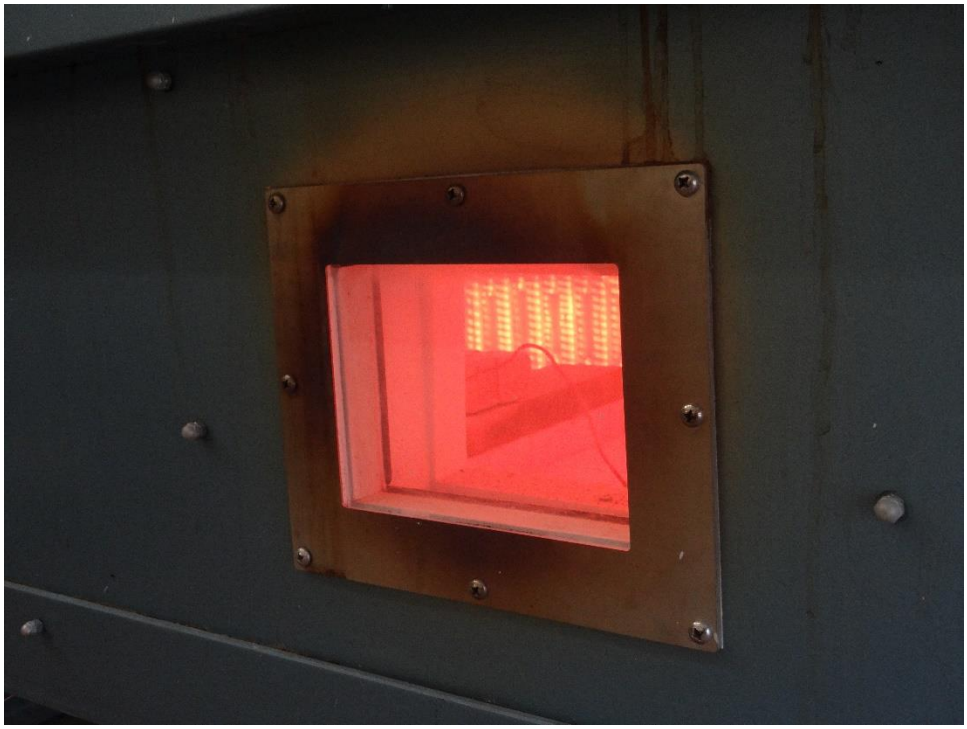

Figure 3.110 Specimens inside the furnace

Figure 3.111 Controller of the furnace

Figure 3.112 Cube samples

The mix developed by Aghdasi, et al., (2017) was taken as a base mix. For trial mix 1, the steel fiber in the base mix was replaced by 0.75% PE fibers (Polyethylene fiber). Samples were prepared and subjected to high temperature after 28 days of curing. The specimens had begun spalling at 300 ºC and nearly a quarter portion of the specimen was spalled-out at 380 ºC. Figure 3.113 (a) shows the specimens after the test. For trial mix 2, 1% of short straight microfiber was added to mix 1. The specimens were begun to spalled-out at the temperature of 150 ºC. The addition of steel fibers had an adverse effect. Although the concrete was spalled-out, the chunks of concrete was held by steel fibers as shown in Figure 3.113 (b). For trial mix 3, the fly ash from mix 2 was removed and tested. Mix 3 also performed the same way as to mix 2 at high temperatures. There was a disastrous spalling as shown in Figure 3.114, on the top of the specimen, which implies that there is no effect of fly ash on the spalling effect. For mix 4, silica fumes was removed from mix 2. The mix 4, specimens had shown the spalling behavior at 435 ºC with the form of big chunks of concrete. The Figure 115 (a) shows the spalling of concrete for mix 4. For mix 5, Polyethylene fibers were replaced by 2% of Polypropylene fibers. The mix 5 was subjected to a temperature up to 435 ºC and observed that there was a reduction in the degree of spalling of concrete as shown in Figure 3.115 (b). However noticeable crack was observed on the surface of the specimen. This indicates that the addition of polypropylene fibers helps to reduce the spalling effect of high-strength concrete. The cracks in the surface of the concrete is assumed to occur due to the melting of the polypropylene fibers at the high temperature.

Figure 3.113 Spalling of UHP-FRC at high temperature (a) mix 1 (b) mix 2

Figure 3.114 Spalling of UHP-FRC without fly ash, mix 3 (a) before heating (b) after heating

Figure 3.115 Spalling of UHP-FRC (a) without silica fume, mix 4 (b) with 2% PP fiber and 1% steel fiber, mix 5

For trial mix 6, the glass powder in mix 1 was replaced by slag cement. The mix 6, as shown in Figure 3.116 (a) specimens began spalling at 150 ºC which implies that the addition of slag cement as replacement of glass powder has no effect regarding on spalling behavior of UHP-FRC at high temperature. For mix 7, the PE fibers from mix 6 was replaced by the 2% of polypropylene fibers. Mix 7 did not show any spalling of concrete but still, there was the development of cracks at the surface of the cube. This shows that the addition of polypropylene fibers helps to reduce the spalling effect but the cause of surface cracks still needs to be investigated. For trial mix 8, the polypropylene fiber content from mix 7 was increased to 2.9% and investigated. For mix 8, as shown in Figure 3.117 (a) no spalling of concrete occurred but the problem of large surface cracks at the specimens was not resolved. For the mix 9, the PE fiber percentage was further increased to 4% from the mix 8, similar to the mix 7 and mix 8, as shown in Figure 3.117 (b) no spalling behavior was observed but the problem of surface cracks was still present. This indicates that increasing PP fibers helps but it is not the only solution and other variables are present and need to be investigated. For the mix 10, the PE fibers from mix 6 was replaced by 1% steel fiber and 1% PP fibers. As shown in Figure 3.118, the spalling behavior was observed at 435 ºC but the concrete chunks was held by steel fibers. For the trial mix 11, the silica sand 1 from the base mix 1 was replaced by coarse aggregates keeping all the other variables were same. The problem of spalling was not resolved anymore at 435 ºC as shown in Figure 113 (b).

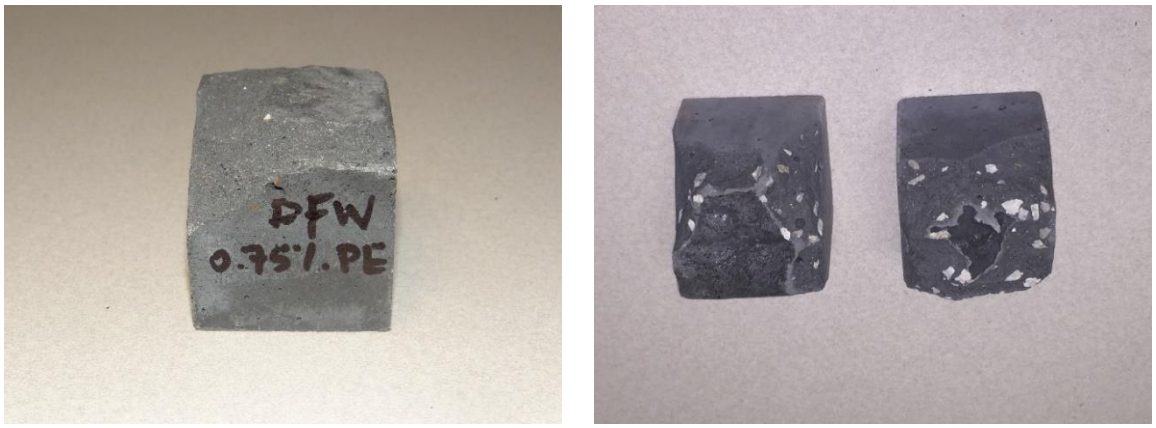

Figure 3.116 (a) Spalling of UHP-FRC Mix 6 (b) Spalling of UHP-FRC with Coarse Aggregates (mix 11)

Figure 3.117 Development of Surface Cracks on UHP-FRC (a) with 2.9% PP fiber, Mix 8 (b) with 4% PP fiber, Mix 9

Figure 3.118 Spalling of UHP-FRC, mix 10

For trial mix 12, the water to binder ratio was increased to 0.25 from mix 2 and the specimens were prepared. For trial mix 13, the water to binder ratio was increased to 0.3 from mix 12 and the specimens were prepared. For trial mix 14, the water to binder ratio was increased to 0.35 from mix 13 and the specimens were prepared. For trial mix 15, the water to binder ratio was increased to 0.4 from mix 14 and the specimens were prepared. For the w/cm 0.25 and w/cm 0.3, as shown in figure 59 (a) the spalling phenomena was present but for the w/cm 0.35 and w/cm 0.4, as shown in figure 59 (b) no spalling of concrete was observed. And the interesting finding is there was no change in compressive strength before and after the specimen subjected to high temperature for mix 14 and mix 15.

Mix 12 to mix 15 were subjected to very high temperature up to 845 ºC and neither any spalling nor any cracks was observed. Although the increase in water to binder ratio helps to control the cracking in the concrete at elevated temperatures this is not a solution since it compromises the compressive strength drastically. The reduction in the spalling of concrete in higher water to binder ratio is assumed to be due to an increase in the porosity of the concrete. No water vapor pressure and no liquid expansion pressure is developed due to the increased porosity.

Figure 3.119 UHP-FRC with High w/cm (a) w/cm 0.25 and w/cm 0.3 After Heating (mix 12 and 13) (b) w/cm 0.35 and w/cm 0.4 After Heating (mix 14 and 15)

Mix 14 and mix 15 did neither show spalling of concrete nor any surface cracks within. So those two mixes were subjected to repetitive temperature change. The specimens were kept inside the furnace, they were heated up to the temperature of 845 ºC and they were allowed to cool down to normal laboratory temperature and heated again. This cycle was run three times. After the repeated application of heat, the specimens did not show any cracks or spalling but the color of the specimens was changed from dark gray to light gray shown in the Figure 3.120.

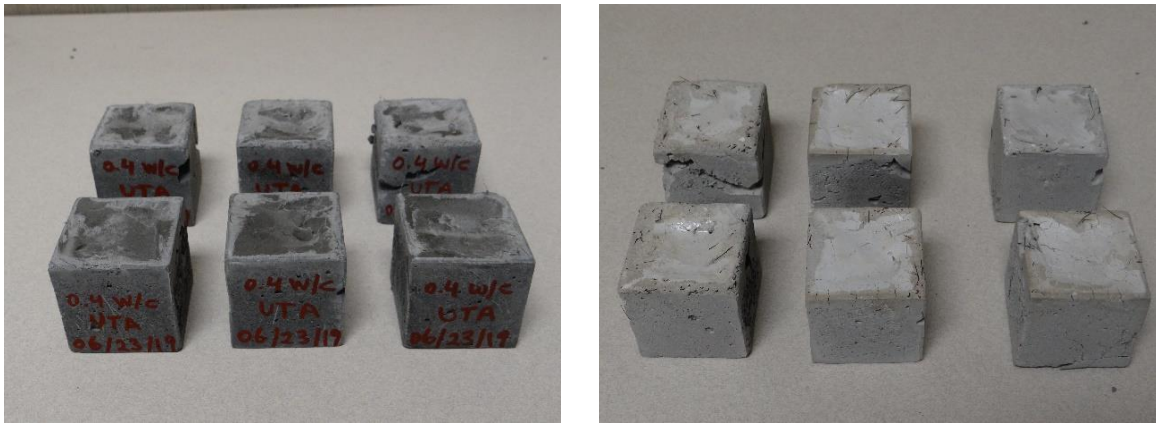

Figure 3.120 UHP-FRC with High w/cm Subjected Repetitive Temperature Change, w/cm 0.4, mix 15, before and after the Repeated Heating

3.5.5 Results and Observation

Based on the observation so far, the following observation can be made.

The inclusion of polypropylene fiber helps reduce the spalling effect of UHP-FRC at elevated temperatures. The increase in w/cm ratio up to 0.35 helps to reduce the spalling effect of high strength concrete but it dramatically reduces the compressive strength. The inclusion of steel fibers holds the concrete while spalling but the effect of steel fiber in the reduction of spalling effect cannot be clearly stated and further research necessary. The effect of fly ash, slag cement, and silica fume in the reduction of spalling was observed as neutral. Replacement of silica sand 1 by coarse aggregates does not have any influence on the spalling effect reduction.

3.6 Lightweight Ultra High Performance Fiber Reinforced Concrete

The normal weight concrete typically has a density of 145 lb./ft^3 to 155 lb./ft^3 while the structural lightweight concrete (SLC) typically has a density of 110 lb./ft^3 to 115 lb./ft^3. ACI 318-19, R19.2.4 defines lightweight concrete as having an equilibrium density from 90 to 135 lb./ft^3. Structural light concrete typically has a similar compressive strength as normal weight concrete at the age of 28 days. Lightweight concrete typically has a smaller elastic modulus which causes smaller tensile stress when concrete shrinks than its normal-weight counterpart (ACI 213, 2014). The science behind lightweight concrete is to replace the heavyweight constituents from normal-weight concrete with something light aggregates or light materials.

Structural lightweight concrete (SLC) has been used in multi-story building frames and floors, curtain walls, shell roofs, folded plates, prestressed or precast elements of all types, and marine structures. The heaviest components of these buildings are slabs. Any reduced weight can significantly reduce the design and construction work in other structural members such as columns, beams, and foundations in addition to the shipping and handling cost, which results in economic benefits. For buildings in high seismic areas, the reduced self-weight can lead to much smaller inertial forces thereby potentially reducing the damage induced by earthquakes. Increased weight of the structure increases the seismic force in the building and requires special designed structural members (Baral & Yajdani (2015).

3.6.1 Development of Ultra-lightweightUHP-FRC

Conventionally, structural lightweight concrete uses lightweight aggregates (LWAs) (expanded shale, slate, and clay) to reduce the weight of concrete. LWAs have a low-particle relative density because of their cellular pore system. The compressive strength of SLC ranges from 3000 to 5000 psi and less frequently up to 7000 psi. In this experiment, instead of using LWAs, high-strength hollow glass microspheres (called 3M Glass Bubbles) made from water-resistant and chemically stable soda-lime borosilicate glass were used to reduce the density of UHP-FRC. Due to the small dimensions of the glass bubbles (16-65 microns), ULW-UHP-FRC was made using the same dense particle packing principle (Aghdasi et al. (2017)) by redesigning and integrating the glass bubbles as one of the fillers. Depending on the compositions, these hollow glass bubbles have a variable crushing strength of 3 to 28 ksi. The glass bubbles have been used in the manufacture of synthetic foam and lightweight concrete as a filler. In the coal-fired power station, glass bubbles are produced as one of the waste products. The spherical shape of 3M glass bubbles offers higher filler loading, lower viscosity/improved flow, and reduced shrinkage and warpage. 3M glass bubbles are available in K series, S series, and iM series. In this research K37, iM16K, and iM30K have been used. The crushing strength of K37, iM16K, and iM30K are 3 ksi, 16 ksi, and 30 ksi, respectively.

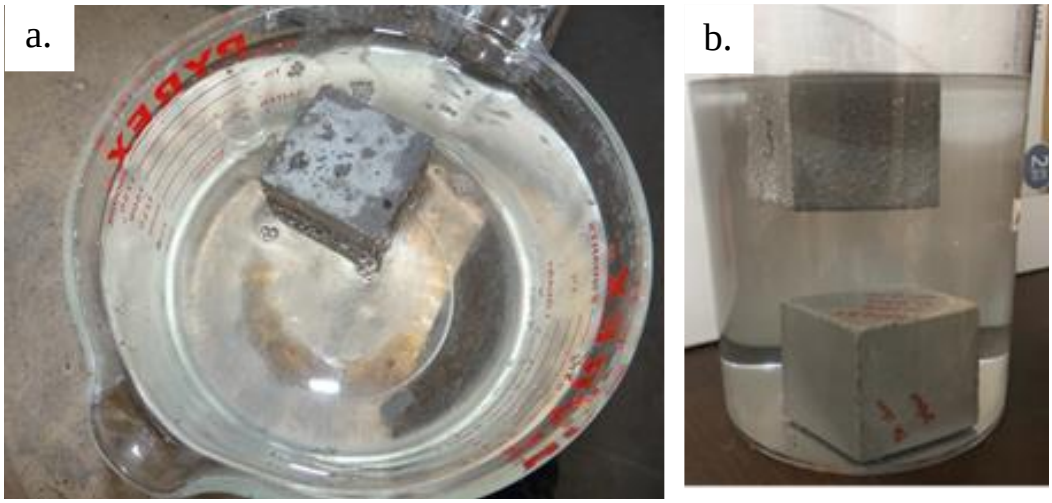

Figure 3.121 Floating of cube in water (a) and (b)

Aghdasi, et al. (2017) [10] developed Ultra-High-Performance Fiber-Reinforced Concrete for Large-Scale Structural Applications by using the dense particle packing concept using normal mixing and curing. This mix uses cement. Fly ash, silica sand 1, silica sand 2, silica fume, high range superplasticizer, glass powder, steel, and water. The mix constituents, median size, and their specific gravity have presented in the following Table 3.7. The median size of the fly ash (20 microns) is comparable to the median size of glass bubbles (16-45 microns). So in the first phase of the experiment, the fly ash from the mix developed by Aghdasi, et al. (2017) [10] was replaced by glass bubbles. Since glass bubbles have a lower density, which leads to higher volume for the same mass. Also, specific surface (surface area per unit weight) increases with reduction in density, which demands more water for lubricating the mix to give the desired workability so the w/cm ratio have also been increased. In the first phase of the experiment, the density of the developed light weight mix is 97 to 117 lb./ft^3. In the second phase of the experiment, further, the glass powder from the resulting mix was replaced by glass bubbles. The glass powder and glass

bubbles both are inert materials and both of them act as fillers in the high-performance concrete. In the second phase of the experiment, the density of the developed lightweight mix is 94 to 111 lb./ft^3.

Table 3.7 Materials used in light Weight UHP-FRC

Materials	**Median size (micron)**	**Specific Gravity**	**Crushing Strength (psi)**
Type I Cement	20	3.15	
Fly Ash	20	1.9-2.8	
Silica Fume	1.2	2.2	
Silica Sand 1	500	2.65-2.67	
Silica Sand 2	120	2.65-2.67	
Glass Powder	1.7	3.01-3.02	
Glass Bubbles (K-37)	45	0.37	3000
Glass Bubbles (iM16K)	20	0.46	16,000
Glass Bubbles (iM30K)	16	0.6	30,000

3.6.2 Replacement of Fly Ash by Glass Bubbles

For mix 1, fly ash was replaced by iM30K glass bubbles with 20% weight of cement and 3% steel fiber was used. The liquefaction time was less than 3 minutes and the flowability of the mix was sufficient. The mix showed the swelling action. The bottom of the cube was not hardened after demolding at 24 hours. The average density after 28 days was found to be 117.4 lb./ft^3 and the average compressive strength of the mix was 7.9 ksi. For mix 2, the

steel fiber from mix 1 was replaced by 0.75% PE fibers. Similar to mix 1, some swelling action was observed. The mix was not hardened until 24 hours of casting. The average density and average compressive strength of the specimen was recorded 109.4 lb./ft^3 and 5.8 ksi. A lower density and lower compressive strength than mix 1 was expected because PE fibers was used instead of steel fiber.

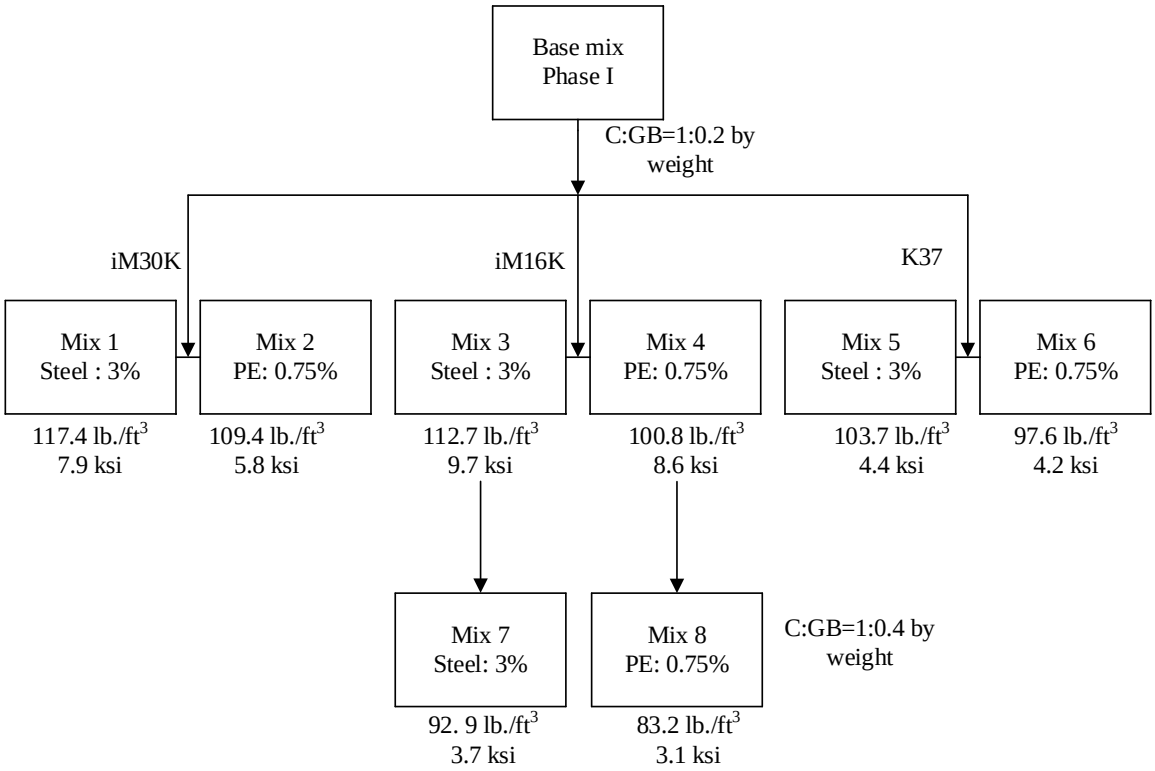

- HRWR % was kept constant 2.1% for all the mixes.
- w/cm ratio was kept constant 0.25 for all the mixes.
- The compressive strength was measured after 28 days.
- C: Cement
- GB: Glass Bubbles
- Density and compressive strength values are average value of 3 specimens each.

Figure 3.122 flowchart of phase I experiment

Figure 3.123 Cube Samples for ULW-UHP-FRC

For mix 3, fly ash was replaced by iM16K glass bubbles with 20% weight of cement and 3% steel fiber was used. The liquefaction time was around 3-4 minutes which is slightly more than mix 1 and mix 2, and the flowability of the mix was sufficient. The mix did not show any swelling actions unlike mix 1 and 2, however, the mix was not hardened after 24 hours of demolding. The average density after 28 days was found to be 112.7 lb./ft3 and the average compressive strength of the mix was 9.7 ksi. For mix 4, the steel fiber from mix 3 was replaced by 0.75% PE fibers. Similar to mix 3, neither any swelling action nor any cracks at the surface were observed. The mix was not hardened until 24 hours of casting. The average density and average compressive strength of the specimen was recorded 100.8 lb./ft3 and 8.6 ksi. A lower density and lower compressive strength than mix 3 was expected because PE fibers was used instead of steel fiber.

For mix 5, fly ash was replaced by K37 glass bubbles with 20% weight of cement and 3% steel fiber was used. The liquefaction time was 5-6 minutes and the flowability of the mix was sufficient. The mix showed the swelling action. The bottom of the cube was not hardened after demolding at 24 hours. The average density after 28 days was found to be

103.7 lb./ft3 and the average compressive strength of the mix was 4.4 ksi. For mix 6, the steel fiber from mix 5 was replaced by 0.75% PE fibers. Similar to mix 5, some swelling action was observed. The mix was not hardened until 24 hours of casting. The average density and average compressive strength of the specimen was recorded 97.6 lb./ft3 and 4.2 ksi. A lower density and lower compressive strength than mix 1 was expected because PE fibers was used instead of steel fiber.

a.

Figure 3.124 (a) Swelling of ULW- UHP-FRC (b) Cracks at the Surface of ULW- UHP-FRC

After observation of mix 1 to mix 6, mix 3 and mix 4 did not show any swelling action, and higher compressive strength was achieved. So the content of glass bubbles in mix 3 and 4 was increased to 40% by the weight of cement. For mix 7, 3% steel fiber was used and for mix 8, 0.75% PE fiber was used instead of steel fiber from mix 7. Because of the high content of glass bubbles, liquefaction time was increased to 7-8 minutes the flowability of the mix was less than 5 inches which led to lower workability in the casting process. Both of the mix, mix 7 and mix 8, were not hardened until 3 days. After demolding at 24 hours, the bottom part of the cube specimen was still in a plastic stage. Because of a high content of glass bubbles, swelling with spongy formation was observed as shown in the Figure 3.126. Formation of the sponge created many voids inside the specimen and led to lower compressive strength. For mix 7, the average density after 28 days was found to be 92.9 lb./ft^3 and the average compressive strength of the mix was 3.7 ksi. And for mix 8, the average density and average compressive strength of the specimen was recorded 83.2

lb./ft^3 and 3.1 ksi. A lower density and lower compressive strength than mix 7 was expected because PE fibers was used instead of steel fiber.

3.6.3 Replacement of Glass Powder by Glass Bubbles

Fly ash was already eliminated in phase I experiment from the mix developed by Aghdasi, et al. (2017) [10]. In the phase II, glass powder was replaced by the glass bubbles and there is no fly ash in the mix. Mix numbers have continued for the previous section to maintain the consistently in the nomenclature. For mix 9, glass powder was replaced with iM30K glass bubbles and 3% steel fiber was used. 25% by weight of glass bubbles was used as glass powder replacement. From the prior preliminary trial, the mix had less workability so the superplasticizer content was increased to 3% by weight of cement and water to cement ratio was maintained to 0.3. The workability was good enough and the flowability was 7 inches in average. No any swelling action was observed. The average density after

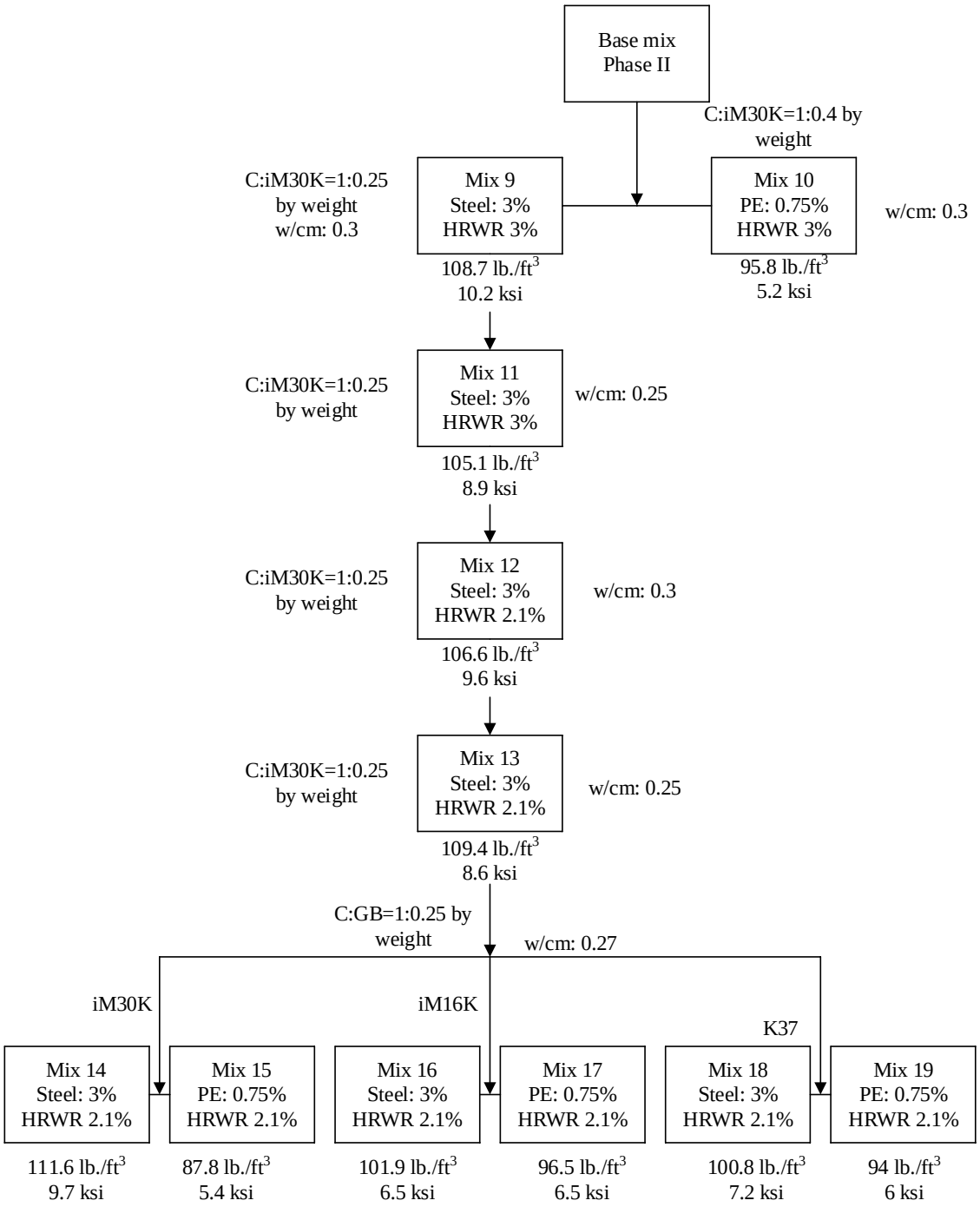

- C: Cement
- GB: Glass Bubbles
- The compressive strength was measured after 28 days.
- Density and compressive strength values are average value of 3 specimens each.

Figure 3.125 Flowchart of phase II experiment

28 days was found to be 108.7 lb./ft^3 and the average compressive strength of the mix was 10.2 ksi.

For mix 10, glass powder was replaced with iM30K glass bubbles and 0.75% PE fiber was used. 40% by weight of glass bubbles was used as glass powder replacement. Similar to the mix 9, superplasticizer content was increased to 3% by weight of cement and water to cement ratio was maintained to 0.3. Because of high volume of glass bubbles, swelling action and sponge formation was observed. Swelling action was responsible to distortion of the shape of the cubical specimens and many voids were observed inside the cube that led to lower compressive strength. As shown in Figure 3.126 a lot of void could be seen in the surface and inside the cube specimens. The cube specimen was still plastic after demolding at 24 hours, and some cracks at the top of the specimens were observed.

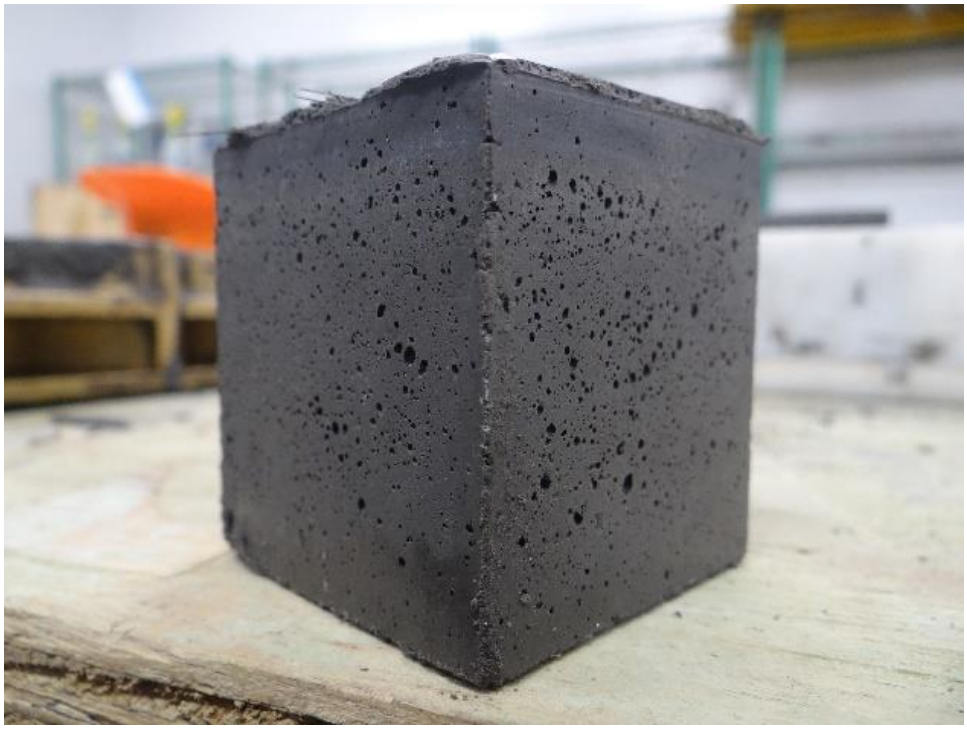

Figure 3.126 Formation of voids in the specimen

Mix 11, mix 12, and mix 13 were used as the preliminary mix to determine the optimum flowability and workability. So for all of those mixes, the material content same as mix 9 has. Mix 11 have 3% superplasticizer and w/cm ratio 0.25. Mix 12 have 2.1% superplasticizer and w/cm ratio 0.3. Mix 13 have 2.1% superplasticizer and w/cm ratio 0.25. For mix 11, the average density after 28 days was found to be 105.1 lb./ft^3 and the average compressive strength of the mix was 8.9 ksi. For mix 12, the average density after 28 days was found to be 106.6 lb./ft^3 and the average compressive strength of the mix was 9.6 ksi. For mix 13, the average density after 28 days was found to be 109.4 lb./ft^3 and the average compressive strength of the mix was 8.6 ksi. Furthermore, the superplasticizer content was kept constant at 2.1% by weight of cement and the w/cm ratio was kept constant at 0.27 for all the mixes.

Figure 3.127 Specimens with (a) Mix 14, (b) Mix 15, (c) Mix 16

For mix 14, glass powder was replaced with iM30K glass bubbles and 3% steel fiber was used. 25% by weight of glass bubbles was used as glass powder replacement. Superplasticizer content was kept 2.1% by weight of cement and the water to cement ratio was maintained at 0.27. The liquefaction time is an average of 5-6 minutes and the flowability of the mix was very high as much as 9 inches. The mix looked cohesive. No swelling and cracks at the surface of the specimens were observed. The problem from phase

I, that is, swelling and formation of some cracks at the surface was resolved. For mix 14, the average density after 28 days was found to be 111.6 lb./ft^3 and the average compressive strength of the mix was 9.7 ksi. For mix 15, steel fibers from mix 14 was replaced with 0.75% PE fibers. The flowability and the liquefaction time was similar to mix 14. For mix 15, the average density after 28 days was found to be 87.5 lb./ft^3 and the average compressive strength of the mix was 5.4 ksi. A lower density and lower compressive strength than mix 14 was expected because PE fiber was used instead of steel fiber. For mix 16, glass powder was replaced with iM16K glass bubbles and 3% steel fiber was used. 25% by weight of glass bubbles was used as glass powder replacement. Superplasticizer content was kept 2.1% by weight of cement and the water to cement ratio was maintained at 0.27. The liquefaction time was increased to more than 10 minutes and the flowability was decreased compared to mix 14 and mix 15. The mix looked cohesive. No swelling and cracks at the surface of the specimens were observed. For mix 16, the average density after 28 days was found to be 101.9 lb./ft^3 and the average compressive strength of the mix was 6.5 ksi. For mix 17, steel fibers from mix 16 was replaced with 0.75% PE fibers. The flowability and the liquefaction time was similar to the mix 16. For mix 17, the average density after 28 days was found to be 96.5 lb./ft^3 and the average compressive strength of the mix was 6.5 ksi. A lower density and lower compressive strength than mix 16 was expected because PE fiber was used instead of steel fiber.

For mix 18, glass powder was replaced with K37 glass bubbles and 3% steel fiber was used. 25% by weight of glass bubbles was used as glass powder replacement. Superplasticizer content was kept 2.1% by weight of cement and the water to cement ratio

was maintained at 0.27. The liquefaction time was increased to more than 10 minutes and the flowability was decreased compared to mix 14 and mix 15. The mix looked cohesive. No swelling and cracks at the surface of the specimens were observed. For mix 18, the average density after 28 days was found to be 100.8 lb./ft^3 and the average compressive strength of the mix was 7.2 ksi. For mix 19, steel fibers from mix 18 was replaced with 0.75% PE fibers. The flowability and the liquefaction time were similar to the mix 18. For mix 19, the average density after 28 days was found to be 94 lb./ft^3 and the average compressive strength of the mix was 6 ksi. A lower density and lower compressive strength than mix 18 was expected because PE fiber was used instead of steel fiber.

Figure 3.128 Specimens with (a) Mix 17, (b) Mix 18, (c) Mix 19

3.6.4 Summary of the Mix Density and Compressive Strength

Table 3.8 Summary of the mix density and compressive strength

Mix	Density (lb./ft^3)	28 days compressive strength (ksi)	Remarks
M1	117.4	7.9	
M2	109.4	5.8	
M3	112.7	9.7	
M4	100.8	8.6	
M5	103.7	4.4	
M6	97.6	4.2	
M7	92.9	3.7	
M8	83.2	3.1	**Minimum density**

M9	108.7	10.2	**Maximum compressive strength**
M10	95.8	5.2	
M11	105.1	5.4	
M12	106.6	9.6	
M13	109.4	8.6	
M14	111.6	9.7	
M15	87.8	8.9	
M16	101.9	6.5	
M17	96.5	6.5	
M18	100.8	7.2	
M19	94	6	

3.6.5 Potential applications of lightweight High performance Concrete

High-performance lightweight concrete may be used as a leveling material in structures where the thickness of concrete required is very small and not much compressive strength of concrete is needed. The current practice of leveling material is the use of concrete with the addition of polystyrene pebbles to reduce the weight of the structure. Ultra-light pebbles make it difficult to handle during the mixing process. In addition, the minimum thickness of the concrete with pebbles is limited however developed high-performance lightweight concrete is easier to handle and may be used for small thickness members as well.

3.6.6 Results and Conclusions

The study above shows the development of ultra-light UHP-FRC. High-strength hollow glass microspheres (called 3M Glass Bubbles) have used as the replacement of the higher weight fly ash and glass powder in the UHP-FRC mix. Light weight UHP-FRC with weight 60-70% of the weight of conventional UHP-FRC having 28 days compressive strength comparable to normal weight concrete has been achieved. To reduce the weight, three

different 3M glass bubbles having crushing strength 3 ksi, 16 ksi and 30 ksi have used. Although the compressive strength of the concrete is generally related to crushing strength of constituents used, no any noticeable correlation between crushing strength of glass bubble and compressive strength of light weight UHP-FRC as observed for 3 three glass bubbles having high gap in their crushing strength. For the future studies, commination of Shale and Glass Bubbles can be used.

4 CONCLUSION AND RECOMMENDATIONS

In this research, several parameters of UHP-FRC and its different applications have been studied. Development of 3D printable UHP-FRC mix, development of ultra-high-performance slurry infiltrated fiber-reinforced concrete (UHP-SIFCON), and examination of UHP-FRC for different fibers fiber types, mitigation measures for early age cracks in UHP-FRC, the performance of UHP-FRC on elevated temperatures and possible methods on reducing the weight of the UHP-FRC have been carried out. Based on the research described herein, the following conclusions can be made.

1. 3D printable UHP-FRC mix has been developed that has excellent buildability and extrude-ability. The developed mix has excellent ductility, sufficient interlayer bonding, and high early age compressive strength of 9.31 ksi for 24 hours.
2. Ultra-high-performance slurry infiltrated fiber-reinforced concrete (UHP-SIFCON) has developed and tested its mechanical properties. The developed UHP-SIFCON can exhibit very high compressive strength more than 33 ksi (165% of UHP-FRC) for an equivalent compressive strain of 8 % (> 5 times of UHP-FRC) and high tensile strength of 2.34 ksi (200% of UHP-FRC, 1.1 ksi) for an equivalent tensile strain of 1.07 % (20 times of UHP-FRC, 0.05%).
3. Two different types of fiber 1D fiber and 3D fiber have been used in the development of SIFCON. The mechanical properties of 3D fiber with lower fiber volume fraction (7.5 %) surpasses the mechanical properties of 1D fiber having higher volume fractions (10 %). The types of hooks and the number of fiber play a

major role in the mechanical properties of SIFCON instead of total volume of fibers.

4. The use of shrinkage reducing admixture (produced by NYCON) on UHP-FRC has a lesser propensity towards shrinkage cracking, but UHP-FRC have a swelling effect and there is a high chance of denigrating the mechanical properties of UHP-FRC resulting dramatically drop in compressive strength. For 0.5% and 1% by weight of cement of SRA dosage, the drop in compressive strength of more than 50% was recorded.

5. The use of concrete curing compound on the surface of UHP-FRC forms a thin layer membrane that acts as a water sealant and ultimately less propensity towards early-age drying shrinkage cracking.

6. The inclusion of polypropylene fiber helps to reduce the spalling effect of UHP-FRC at elevated temperatures. The inclusion of 2%, 3% and 4% of polypropylene fiber have similar effect in the spalling effect , still the surface cracks were present in all the cases. This indicates that only increasing the polypropylene fibers does not necessarily resolve the problem of cracking and spalling of UHP-FRC at high temperature.

7. The increase in w/cm ratio up to 0.35 helps to reduce the spalling effect of high strength concrete but it dramatically reduces the compressive strength. However, interestingly, the compressive strength of samples with 0.35 w/cm does not lose any compressive capacity for 3 cycles of temperature up to neatly 845 ºC (1472 ºF).

8. Fly ash, slag cement, and silica fumes did not show any direct correlation with the spalling effect of UHP-FRC.

9. Lightweight UHP-FRC with weight 60-70% of the weight of conventional UHP-FRC having 28 days compressive strength comparable to normal weight concrete has been achieved. To reduce the weight, three different 3M glass bubbles having crushing strength 3 ksi, 16 ksi and 30 ksi have been used. Although the compressive strength of the concrete is generally related to the crushing strength of constituents used, no noticeable correlation was observed for 3 three glass bubbles having a high gap in their crushing strength.

REFERENCES

[1] J. Pegna, Exploratory investigation of solid freeform construction, Autom. Construct.5 (5) (1997) 427–437.

[2] Bandyopadhyay, Amit. Additive Manufacturing. CRC Press, 2016.

[3] Zhang, Jingchuan & Wang, Jialiang & Dong, Sufen & Yu, Xun & Han, Baoguo. (2019). A review of the current progress and application of 3D printed concrete. Composites Part A: Applied Science and Manufacturing. 125. 105533. 10.1016/j.compositesa.2019.105533.

[4] Perrot A, Rangeard D, Pierre A. Structural built-up of cement-based materials used for 3D-printing extrusion techniques. Mater Struct 2016; 49:1213–20.

[5] Gosselin C, Duballet R, Roux P, et al., Large-scale 3D printing of ultra-high-performance concrete – a new processing route for architects and builders. Mater Des 2016; 100:102–9.

[6] Khoshnevis, Behrokh. (2004). Automated construction by contour crafting - Related robotics and information technologies. Automation in Construction. 13. 5-19. 10.1016/j.autcon.2003.08.012.

[7] Schutter GD, Lesage K, Mechtcherine V, et al., Vision of 3D printing with concrete technical, economic and environmental potentials. Cem Concr Res 2018; 112:25–36.

[8] https://www.3printr.com/3d-concrete-printing-market-reach-56-4-million-2021-1239664/

[9] Aghdasi, P., Heid A. E., and Chao, S.-H. (2016), “Developing Ultra-High Performance Fiber-Reinforced Concrete For Large-Scale Structural Applications,” ACI Materials Journal, V. 113, No. 5, September-October 2016, pp. 559-570

[10] Zhu, Binrong & Pan, Jinlong & Nematollahi, Behzad & Zhou, Zhenxin & Zhang, Yang & Sanjayan, Jay. (2019). Development of 3D printable engineered cementitious composites with ultra-high tensile ductility for digital construction. Materials & design. 108088. 10.1016/j.matdes.2019.108088.

[11] Halit Yazıci, et al., "Mechanical properties of reactive powder concrete containing high volumes of ground granulated blast furnace slag." Cement and Concrete Composites 32.8 (2010): 639-648.

[12] A.M. Neville, Properties of Concrete, vol. 844, Wiley, New York and Longman, London, 1995 Five, and Final Edition.

[13] ASTM C1437-07 Standard Test Method for Flow of Hydraulic Cement Mortar, ASTM International, West Conshohocken, PA, 2015

[14] ASTM C78/C78M – 21 Standard Test Method for Flexural Strength of Concrete (Using Simple Beam with Third-Point Loading)

[15] Hosseini, Ehsan & Zakertabrizi, Mohammad & Habibnejad Korayem, Asghar & Xu, Guanzhong. (2019). A novel method to enhance the interlayer bonding of 3D printing concrete: An experimental and computational investigation. Cement and Concrete Composites. 99. 10.1016/j.cemconcomp.2019.03.008.

[16] A. Standard, ISO/ASTM 52900: 2015 Additive Manufacturing-General Principles-Terminology, ASTM, 2012 F2792-10e1.

[17] A.A. Ramezanianpour, A. Kazemian, M. Nikravan, M.A. Moghadam, Influence of a low-activity slag and silica fume on the fresh properties and durability of high performance self-consolidating concrete, in: International Conference on Sustainable Construction Materials & Technologies (SCMT3), Kyoto, Japan, 2013.

[18] A.A. Ramezanianpour, A. Kazemian, M. Nikravan, M.A. Moghadam, Influence of a low-activity slag and silica fume on the fresh properties and durability of high performance self-consolidating concrete, in: International Conference on Sustainable Construction Materials & Technologies (SCMT3), Kyoto, Japan, 2013.

[19] Sustainable Construction Materials & Technologies (SCMT3), Kyoto, Japan, 2013.

[20] Kazemian, Ali & Yuan, Xiao & Cochran, Evan & Khoshnevis, Behrokh. (2017). cementitious materials for construction-scale 3D printing: Laboratory testing of fresh printing mixture. Construction and Building Materials. 145. 639-647. 10.1016/j.conbuildmat.2017.04.015.

[21] El-Tawil, S.; Tai, Y.-S.; Meng, B.; Hansen, W.; Liu, Z. Commercial Production of Non-Proprietary Ultra High Performance Concrete; Technical Report; The Regents of the University of Michigan: Ann Arbor, MI, USA, 2018.

[22] A. Perrot, D. Rangeard, A. Pierre, Structural built-up of cement-based materials used for 3D-printing extrusion techniques, Mater. Struct. 49 (4) (2016) 1213–1220.

[23] N. Roussel, Understanding the rheology of Concrete, Woodhead Publishing, Cambridge, 2012.

[24] D. Lootens, P. Jousset, L. Martinie, N. Roussel, R.J. Flatt, Yield stress during setting of cement pastes from penetration tests, Cement and Concrete Research, Volume 39, Issue 5, 2009

[25] Xu, W., Gao, Y., Sun, C., Wang, Z.: Fabrication and Application of 3D-Printed Concrete Structural Components in the Baoshan Pedestrian Bridge Project. In: Burry, J., Sabin, J., Sheil, B., and Skavara, M. (eds.) Fabricate 2020. UCL Press (2020).

[26] Theo A. M. Salet, Zeeshan Y. Ahmed, Freek P. Bos & Hans L. M. Laagland (2018): Design of a 3D printed concrete bridge by testing, Virtual and Physical Prototyping, DOI:10.1080/17452759.2018.1476064

[27] Gebhard L. et al., (2020) Aligned Interlayer Fiber Reinforcement and Post-tensioning as a Reinforcement Strategy for Digital Fabrication. In: Bos F., Lucas S., Wolfs R., Salet T. (eds) Second RILEM International Conference on Concrete and Digital Fabrication. DC 2020. RILEM Book series, vol 28. Springer, Cham. https://doi.org/10.1007/978-3-030-49916-7_63

[28] N. Hack, W.V. Lauer, Mesh-Mould: robotically fabricated spatial meshes as reinforced concrete formwork, Archit. Des. 84 (2014) 44–53, http://dx.doi.org/10.1002/ad.1753.

[29] Asprone, Domenico & Menna, Costantino & Bos, Freek & Salet, Theo & Mata-Falcón, Jaime & Kaufmann, Walter. (2018). Rethinking reinforcement for digital fabrication with concrete. Cement and Concrete Research. 112. 10.1016/j.cemconres.2018.05.020.

[30] www.winsun3d.com

[31] Stampler, L. (2015). A Chinese Company 3D-Printed this five-Storey Apartment Building. Time, 20 January 2015. https://time.com/3674557/3d-printed-apartment-building-winsun/

[32] Vantyghem, Gieljan & Corte, Wouter & Shakour, Emad & Amir, Oded. (2020). 3D printing of a post-tensioned concrete girder designed by topology optimization. Automation in Construction. 112. 10.1016/j.autcon.2020.103084.

[33] N. Roussel, Understanding the rheology of Concrete, Woodhead Publishing, Cambridge, 2012.

[34] D. Lootens, P. Jousset, L. Martinie, N. Roussel, R.J. Flatt, Yield stress during setting of cement pastes from penetration tests, Cement and Concrete Research, Volume 39, Issue 5, 2009

[35] Joseph J. Assaad, Jacques Harb, Yara Maalouf, Measurement of yield stress of cement pastes using the direct shear test Journal of Non-Newtonian Fluid Mechanics, Volume 214, 2014, Pages 18-27, ISSN 0377-0257, https://doi.org/10.1016/j.jnnfm.2014.10.009.

[36] Q.D. Nguyen, D.V. Boger, Direct yield stress measurement with the vane method, J. Rheol. 29 (1985) 335–347.

[37] T.T. Le, et al., Mix design and fresh properties for high-performance printing concrete, Mater. Struct. 45 (8) (2012) 1221–1232.

[38] B. Nematollahi, et al.,, Effect of polypropylene fiber addition on properties of geopolymers made by 3D printing for digital construction, Materials 11 (12) (2018) 2352.

[39] Manuel Hambach, Dirk Volkmer, Properties of 3D-printed fiber-reinforced Portland cement paste, Cement and Concrete Composites,Volume 79,2017,Pages 62-70,ISSN 0958-9465, https://doi.org/10.1016/j.cemconcomp.2017.02.001.

[40] D.G. Soltan, V.C. Li, A self-reinforced cementitious composite for building-scale 3D printing, Cement and Concrete Composites (2018), doi: 10.1016/j.cemconcomp.2018.03.017.

[41] Yiwei Weng, Mingyang Li, Zhixin Liu, Wenxin Lao, Bing Lu, Dong Zhang & Ming Jen Tan (2019) Printability and fire performance of a developed 3D printable fibre reinforced cementitious composites under elevated temperatures, Virtual and Physical Prototyping, 14:3, 284-292, DOI: 10.1080/17452759.2018.1555046

[42] Ogura, Hiroki & Nerella, Venkatesh Naidu & Mechtcherine, Viktor. (2018). Developing and Testing of Strain-Hardening Cement-Based Composites (SHCC) in the Context of 3D-Printing. Materials. 11. 1375. 10.3390/ma11081375.

[43] Chaves Figueiredo, S., Romero Rodríguez, C., Ahmed, Z., Bos, D. H., Xu, Y., Salet, T., Çopuroglu, O., Schlangen, E., & Bos, F. (2019). An approach to develop printable strain hardening cementitious composites. Materials & Design, 169, [107651]. https://doi.org/10.1016/j.matdes.2019.107651

[44] Binrong Zhu, Jinlong Pan, Behzad Nematollahi, Zhenxin Zhou, Yang Zhang, Jay Sanjayan, Development of 3D printable engineered cementitious composites with ultra-high tensile ductility for digital construction, Materials & Design, Volume 181, 2019, 108088, ISSN 0264-1275, https://doi.org/10.1016/j.matdes.2019.108088.

[45] T.T. Le, S.A. Austin, S. Lim, R.A. Buswell, R. Law, A.G.F. Gibb, T. Thorpe, Hardened properties of high-performance printing concrete, Cement and Concrete Research, Volume 42, Issue 3, 2012, Pages 558-566, ISSN 0008-8846, https://doi.org/10.1016/j.cemconres.2011.12.003.

[46] Nematollahi, Behzad & Xia, Ming & Sanjayan, Jay & Vijay, Praful. (2018). Effect of Type of Fiber on Inter-Layer Bond and Flexural Strengths of Extrusion-Based 3D Printed Geopolymer. Materials Science Forum. 939. 155-162. 10.4028/www.scientific.net/MSF.939.155.

[47] R.J.M. Wolfs, F.P. Bos, T.A.M. Salet,Early age mechanical behaviour of 3D printed concrete: Numerical modelling and experimental testing, Cement and Concrete Research, Volume 106, 2018, Pages 103-116, ISSN 0008-8846, https://doi.org/10.1016/j.cemconres.2018.02.001.

[48] Lex Reiter, Timothy Wangler, Nicolas Roussel, Robert J. Flatt, The role of early age structural build-up in digital fabrication with concrete, Cement and Concrete Research, Volume 112, 2018, Pages 86-95, ISSN 0008-8846, https://doi.org/10.1016/j.cemconres.2018.05.011.

[49] ASTM C403/C403M − 16, Standard Test Method for Time of Setting of Concrete Mixtures by Penetration Resistance

[50] Eric L. Kreiger, Megan A. Kreiger, Michael P. Case, Development of the construction processes for reinforced additively constructed concrete, Additive Manufacturing, Volume 28, 2019, Pages 39-49, ISSN 2214-8604, https://doi.org/10.1016/j.addma.2019.02.015.

[51] Yi Wei Daniel Tay, Guan Heng Andrew Ting, Ye Qian, Biranchi Panda, Lewei He & Ming Jen Tan (2019) Time gap effect on bond strength of 3D-printed concrete, Virtual and Physical Prototyping, 14:1, 104-113, DOI: 10.1080/17452759.2018.1500420

[52] Al-Qutaifi, Ali Nazari, Ali Bagheri, Mechanical properties of layered geopolymer structures applicable in concrete 3D-printing, Construction and Building Materials, Volume 176, 2018, Pages 690-699, ISSN 0950-0618, https://doi.org/10.1016/j.conbuildmat.2018.04.195.

[53] Luong Pham, Guoxing Lu, and Phuong Tran.3D Printing and Additive Manufacturing. ahead of print http://doi.org/10.1089/3dp.2020.0172

[54] Homrich, Joseph & Naaman, Antoine. (1988). Stress-Strain Properties of SIFCON in Uniaxial Compression and Tension. 147.

[55] Haynes H Investigation of fiber reinforcement methods for thin shell concrete. Naval Civil Engineering Laboratory, Port Hueneme,CA,N-979,1-26(1968)

[56] Ozkan Sengul, Mechanical properties of slurry infiltrated fiber concrete produced with waste steel fibers, Construction and Building Materials, Volume 186, 2018, Pages 1082-1091, ISSN 0950-0618, https://doi.org/10.1016/j.conbuildmat.2018.08.042.

[57] A.E. Naaman, J.R. Homrich, Tensile stress-strain properties of SIFCON, ACI Mater. J. 86 (3) (1989) 244–251.

[58] Lankard, D.R. Slurry Infiltrated Fiber Concrete (SIFCON): Properties and Applications. MRS Online Proceedings Library 42, 277–286 (1984). https://doi.org/10.1557/PROC-42-277

[59] B.T. Wood. Use of slurry infiltrated fiber concrete (SIFCON) in hinge regions for earthquake resistant structures, Ph.D. thesis North Carolina State University, Civil Engineering, Raleigh, 2000.

[60] Halit Yazıcı, Hüseyin Yiğiter, Serdar Aydın, Bülent Baradan, Autoclaved SIFCON with high volume Class C fly ash binder phase, Cement and Concrete Research, Volume 36, Issue 3, 2006, Pages 481-486, ISSN 0008-8846 https://doi.org/10.1016/j.cemconres.2005.10.002.

[61] Khoury, G.A. and Anderberg, Y. ‘‘Concrete spalling review’’, Report Submitted to the Swedish National Road Administration (2000).

[62] Khoury GA (2000) Effect of fire on concrete and concrete structures. Prog Struct Mater Eng 2:429–44

[63] M. Bastami, A. Chaboki-Khiabani, M. Baghbadrani, M. Kordi, Performance of high strength concretes at elevated temperatures, Scientia Iranica, Volume 18, Issue 5, 2011, Pages 1028-1036, ISSN 1026-3098; https://doi.org/10.1016/j.scient.2011.09.001.

[64] Lo Monte, F.; Felicetti, R.; Rossino, C. Fire spalling sensitivity of high-performance concrete in heated slabs under biaxial compressive loading. Mater. Struct. 2019, 52, 14.

[65] Lau, A., and Anson, M. (2006). “Effect of high temperatures on high performance steel fibre reinforced concrete.” Cement and Concrete Research, 36(9), 1698–1707.

[66] Li, Y., Pimienta, P., Pinoteau, N., and Tan, K. H. (2019). “Effect of aggregate size and inclusion of polypropylene and steel fibers on explosive spalling and pore pressure in ultra-high-performance concrete (UHPC) at elevated temperature.” Cement and Concrete Composites, 99(June 2018), 62–71.

[67] D.P. Bentz a, O.M. Jensen, “Mitigation strategies for autogenous shrinkage cracking,” Cement & Concrete Composites 26 (2004) 677–685

[68] A. M. Soliman, M. L. Nehdi, “Effect of drying conditions on autogenous shrinkage in ultra-high performance concrete at early-age,” Materials and Structures (2011) 44:879–899.

[69] Karmacharya, A. and Chao, S.-H. “Precast Ultra-High-Performance Fiber-Reinforced Concrete (UHP-FRC) for Fast and Sustainable Pavement Repair,” Transportation Consortium of South Central States Conference, San Antonio, TX, April 12, 2019.

[70] Tuladhar S. & Chao S., (2019) “A Simple Tensile Testing Method for UHP-FRC Based on Double-Punch Test”, International Interactive Symposium on Ultra-High Performance Concrete 2(1). doi: https://doi.org/10.21838/uhpc.9662

[71] Baral, A., & Yajdani, S. K. (2015). Seismic analysis of RC framed building for different position of shear wall. International Journal of Innovative Research in Science, Engineering and Technology, 4(5), pp. 3346-3353.

[72] Theo A. M. Salet, Zeeshan Y. Ahmed, Freek P. Bos & Hans L. M. Laagland (2018): Design of a 3D printed concrete bridge by testing, Virtual and Physical Prototyping, DOI:10.1080/17452759.2018.1476064

BIOGRAPHICAL INFORMATION

Bhupendra Raj Acharya graduated from Tribhuvan University, Kathmandu, Nepal in 2015 with Bachelor's degree in Civil Engineering. Right from his undergraduate study, he worked as a civil engineer in the National Society for Earthquake Technology – Nepal (NSET) supervised the construction of many RCC buildings. With a year of experience as a Civil Engineer, he joined Build Change as an Assistant Engineer where he was responsible for structural analysis and design of RCC and load bearing masonry buildings as well as the design of retrofitting of load bearing masonry buildings affected by the Nepal earthquake 2015. With a year of experience, he was given the responsibility of training team leader where he was responsible to contact and coordinate with government officials of the Nepal Reconstruction Authority and organize various levels of retrofitting training of load-bearing masonry. With three years of professional experience, he joined The University of Texas at Arlington for Masters of Science in Civil Engineering with a concentration in Structures and Applied Mechanics. During his graduate program, she worked as a Graduate Research Assistant under the supervision of Dr. Shih-Ho Chao. During his MS study, he was awarded the Outstanding Civil Engineering MS Student Award for 2019-2020 and 2020-2021. His research interest includes Ultra-High Performance Fiber Reinforced Concrete (UHP-FRC) and its different application. He enjoys working on the analysis and design of structures over seismic forces.